MATHEMATICAL MODELING OF FIBRIN GELATION DYNAMICS AND STRUCTURE FORMATION UNDER FLOW

by

Cheryl L. Zapata-Allegro

A dissertation submitted to the faculty of
The University of Utah
in partial fulfillment of the requirements for the degree of

Doctor of Philosophy

Department of Mathematics

The University of Utah

May 2018

The University of Utah Graduate School

STATEMENT OF DISSERTATION APPROVAL

The dissertation of **Cheryl L. Zapata-Allegro**
has been approved by the following supervisory committee members:

Aaron L. Fogelson ,	Chair(s)	**March 29, 2016** Date Approved
James P. Keener ,	Member	**March 29, 2016** Date Approved
Christel Hohenegger ,	Member	**March 29, 2016** Date Approved
Yekaterina Epshteyn ,	Member	**March 29, 2016** Date Approved
Keith B. Neeves ,	Member	**March 29, 2016** Date Approved

by **Davar Khoshnevisan** , Chair/Dean of
the Department/College/School of **Mathematics**
and by **David B. Kieda** , Dean of The Graduate School.

ABSTRACT

Fibrin fibers are an essential component of blood clots. They provide structural support and prevent embolism. Formation of fibrin fibers is initiated by the enzyme thrombin, which is a product of the coagulation cascade. It converts fibrinogen into fibrin monomers. Fibrin monomers polymerize to form half-staggered protofibrils that laterally aggregate to form fibrin fibers. Fibrin fibers form a mesh or gel-like structure over an injury zone and in and around platelet aggregates. It is known that the structure of fibers are dependent on the conditions in which they are formed.

We present a two-dimensional mathematical model of fibrin polymerization in flow with feedback on the fluid. We include a spatial-temporal source of fibrin monomers from a simplified coagulation scheme. In the model, fibrin polymerizes by forming linear bonds between any two oligomers and by forming branch points between any three oligomers. Because we want to track oligomer concentrations composed of any number of monomers and branch points, we have a doubly infinite set of PDEs which include diffusion and advection of oligomers. Using a generating function and a change of variable, we find a closed system of equations to study fibrin gelation and postgelation dynamics. The model tracks both branch point and fibrin mass densities of the gel which are used to calculate a distribution of fiber diameters and pore sizes. The permeability of the gel, which is calculated from the volume fraction of fibrin and the fiber diameters, is used to hinder the fluid velocity through a Brinkman term. We vary model parameters, such as the thrombin production rate and the rate of branch point formation, to find what effect this has on clot structure.

We also present two model modifications. We alter the model to include thrombin production on three different distributions of platelet aggregates. We also modify the model to include hindered transport on all proteins. The diffusivity and advection of oligomers and coagulation proteins are dependent on the amount of gel at each spatial locations. An additional velocity term is included that moves proteins from areas of high volume fraction of gel to areas of low gel volume fraction of gel.

CONTENTS

LIST OF FIGURES

LIST OF TABLES

CHAPTER 1

INTRODUCTION

Coagulation is an essential process that allows animals to maintain healthy vasculature. The process is a complicated cascade of proteolytic reactions that results in a blood clot or thrombus. When an injury occurs, the subendothelium exposes tissue factor that initiates the cascade [34]. Platelets and zymogens circulating in the blood become activated. Platelets cover the injury zone and act as a surface for reactions. One essential reaction results in the coagulation enzyme thrombin. Thrombin is responsible for converting the zymogen fibrinogen into the active form, fibrin. Fibrin polymerizes to form fibrin fibers that make a gel-like network over the injury and bound platelets. This composition is defined as a thrombus. Following formation, fibrinolysis breaks down the fibrin fibers and dissolves the clot.

Coagulation requires a balance between inhibition, activation, and fluid dynamics. An excess of fibrin gelation can lead to difficulties in fibrinolysis, while too little fibrin can cause embolism. The properties of a fibrin gel, including fiber diameter and porosity, are determined from the conditions during polymerization.

In this dissertation, we examine the process of fibrin clot formation. In the remainder of this chapter we discuss the biological background and previous fibrin polymerization and gelation models. In Chapter 2, we derive a 2-D mathematical model of fibrin gelation in flow. In Chapter 3, we discuss the results, parameter explorations, and implications of the model. In Chapter 4, we present an expanded model that includes more biologically realistic coagulation dynamics. In Chapter 5, we present a modified model that incorporates the effect that fibrin gel has on transport. Chapter 6 contains a description of the numerical methods used to simulate the models.

1.1 Fibrin Polymerization

Fibrin polymerization is the process in which fibrin monomers become a gel of fibrin fibers. The process begins at the end of the coagulation cascade where the zymogen prothrombin (Factor II) is converted to the enzyme thrombin (Factor IIa) by the prothrom-

binase complex. Prothrombinase is located on the membrane of platelets and is comprised of Factor Xa and the cofactor, Factor Va.

Prothrombin is carried in the blood at a concentration around 1.4 μM [26]. Prothrombin binds to specific sites on activated platelet. Activated platelets have binding sites for many different coagulation proteins. Factor Va and Xa can also bind to specific sites on the membrane of platelets and join together to form a complex called prothrombinase. Platelet-bound prothrombin binds to prothrombinase and prothrombinase prothrombin to thrombin. Prothrombin can be converted to thrombin in the plasma by Xa. However, this reaction is 4-5 orders of magnitude slower than the conversion of platelet bound prothrombin by prothrombinase [27]. Thrombin is inhibited by antithrombin in order to prevent fibrin monomer production away from an injury.

Fibrinogen is a soluble glycoprotein present in human blood plasma at a concentration of 2.5 g/L [35]. Fibrinogen molecules are 45 nm long and symmetrical. Each half is composed of 3 peptide chains (Aα, Bβ, and γ). The 3 peptide chains are coiled around each other. The two halves of fibrinogen are connected at the central nodule. The N-termini of the Aα and Bβ peptide chains (near the central nodule) contain fibrinopeptides A (FpA) and fibrinopeptides B (FpB) [8]. In order for polymerization to begin, thrombin must cleave FpA from fibrinogen. Thrombin also cleaves FpB. The cleavage events expose knob 'A' and knob 'B' on the N-termini of the α and β chains, respectively. These sequences bind to 'a' holes and 'b' holes in the γ chain on the end of a different fibrin(ogen) molecule. While FpA and FpB can be cleaved at different times, in solution FpA is cleaved first. It is sufficient for only FpA to be cleaved in order for fibrin to form protofibrils [36], [39].

Once thrombin has converted fibrinogen into fibrin monomer, fibrin polymerization begins. Monomers bind center to end. Therefore, fibrin polymerization yields half-staggered protofibrils with a repeat unit of 22.5 nm [37]. Fibrin oligomers are defined to be protofibrils when they reach a length of $0.5 - 0.6\mu$m, which corresponds to 20-25 monomers [6]. At this length, protofibrils can laterally aggregate to form fibrin fibers. The exact mechanism for lateral aggregation is still unknown. However it is known that protofibrils will twist around each other during fiber formation. FpB cleavage might play a role in this process [36].

Fibrin fibers contain two types of branches, bilateral junctions and equilateral junction. Bilateral junctions are formed by two protofibrils laterally aggregating and then separating again to form a branch. The second type of branch is called an equilateral junction which is formed when three fibrin monomers bind together to form an equilateral triangle [28].

Experiments in static conditions have studied the effects of thrombin concentration on

fibrin polymerization. These studies showed that higher concentrations of thrombin form thin fibers with more branches (as compared to lower concentrations of thrombin, which form thick fibers with few branches)[38].

Once there is a three-dimensional network of fibers (branched and unbranched) that behaves like a solid, the clot is formed. This is also known as reaching the gel point. Even though the gel has formed, fibers can continue to thicken, grow longitudinally, and add branches [7].

It is important to study fibrin polymerization in blood flow in order to understand how clots are formed physiologically. There are several key differences between forming a clot in flow and forming a clot in static conditions. Because flow is continuously supplying fibrinogen to the injury site, clots formed in flow tend to have thicker fibers [29]. Similarly, fibrin is constantly being carried out by the fluid. Therefore, fibers have to form and adhere to platelets or subendothium before the flow carries them out. In the same way that the fluid can affect the clot formation, the gel structure can affect the fluid motions.

While most experiments on fibrin clot formation have been performed in static conditions, researchers have recently found techniques to study clot formation in flow. One result from the flow experiments by Wolberg and Weisel (independently) showed that fibrin fibers tend to align in the direction of flow [5] [13]. Even at a low shear rate of 5 s^{-1} (venous flow is around 100 s^{-1}), fibers begin to align. At slightly higher (but still considered low) shear rates, thick fibers are almost completely aligned in the direction of flow. Thin fibers that are perpendicular to the flow serve as connectors between the thicker fibers. Blood clots have also been studied *in vivo*. Clots formed in veins are fibrin-rich. In arteries, where high shear rates are experienced, clots tend to be platelet-rich with fibrin-rich areas only on the downstream end of the clot (where lower shear rates are experienced due to platelets hindering the flow) [40].

1.2 Previous Models

One of the first mathematical models used to study fibrin polymerization was by Hantgan and Hermans in 1979 [15]. They were able to show from their model, along with experimental data, that fibrin polymerization does not require nucleation, i.e., there is not a separate slow nucleation process to start a protofibril. In 1992, Weisel and Nagaswami created one of the first computational models of fibrin polymerization [38]. The model consists of a set of ODEs that explicitly models monomers binding to oligomers, oligomers transitioning to protofibrils, and collections of protofibrils becoming fibers. This model is

able to reproduce lag times seen in experiments between initiation and formation of a fibrin network. It also makes predictions about the effect kinetic rate constants have on fiber size and length.

In order to create models that include reactions between any size oligomers, researchers began using the mathematical framework introduced by Ziff and Stell to study the dynamics of condensation reactions and gelation [42]. Published in 1980, the Ziff-Stell model uses an infinite set of Smoluchowski coagulation equations which describe changes in the concentration of any size oligomer due to polymerization. The system of ODEs includes binding of any two size oligomers. Using a generating function to transform the set of ODEs to a single PDEs and single ODE, they were able to identify a mathematical singularity that indicates the transition from oligomers to gel and the time this transition occurs. They also extended their general polymerization model to include postgelation dynamics. In 2007, Guy et al. used the frame work presented in the Ziff-Stell model to study fibrin gelation [14]. They coupled a modification of the condensation reaction to include a sink (advection) and a source of fibrin monomers with a simplified coagulation cascade and a shear flow. The model answers the question, how tall will a fibrin gel grow in flow? While the model itself is actually quite simple, it is able to study key dynamics of fibrin gelation including thrombin inhibition, effects of fluid flow, and gel permeability.

Fogelson and Keener modified the Ziff-Stell model to include two types of reactions, branch point formation and linear reaction [11]. We will refer to this model as the 'Branching Model'. The original model consists of a doubly infinite set of ODEs for the concentration of oligomers with a different number of branch points and monomers units. The model is reduced to a small set of ODEs for physically-interesting quantities such as concentration of branch points by expressing them as moments of the oligomers concentrations. While the Branching Model does not include the formation of bilateral junctions or lateral aggregation of protofibrils, it does include the formation of equilateral junctions. The Branching Model supplies fibrin monomers at a constant rate and tracks the concentration of reactive sites and branch points, as well as fibrin mass until gel time. By tracking the concentration of branch points, the model is able to predict structure of the oligomers. While the Branching Model initially wrote the condensation reactions as ODEs, it is easily extended to a spacial-temporal model that includes advection of oligomers coupled with fluid dynamics. Also, the model only tracks concentration until gel time and therefore does include any gel formation or postgelation dynamics. These limitations led Fogelson and Keener to revisit the Ziff-Stell model and create a systematic way of including and studying postgelation

dynamics [12].

In Fogelson et al. [12], they begin with general condensation equations that include sources, sinks, and diffusion and apply the same generating function as Ziff-Stell [12]. They show that under the correct change of variables, one can find a closed system of equations that model monomers polymerizing into a gel. They also provided an approach that tracks structural properties of the gel and the oligomers in the solvent. We use the approach that was first presented by Ziff-Stell and modified in Guy et al., the Branching Model, and Fogelson et al., 2015 to examine the effects of fluid flow on the structure of fibrin polymerization.

CHAPTER 2

MODEL

We consider a rectangular domain, $\mathbf{x} \in [0, L_{x_1}] \times [0, L_{x_2}]$, that represents a segment of a blood vessel. The top and bottom, $x_2 = 0$ and $x_2 = L_{x_2}$, represent the vessel walls. We assume that blood flows into the vessel at $x_1 = 0$ with a specific profile and leaves the vessel at $x_1 = L_{x_1}$. An injury zone is located at the center of the lower vessel wall at $[L_1, L_2]$, where $0 < L_1 < L_2 < L_{x_1}$. A depiction of the domain is shown in Figure 2.1. We have three types of species, coagulation chemicals, fibrin oligomers, and fibrin gel. Due to the complexity of coagulation, we use a simplified system involving only three coagulation proteins, prothrombin, thrombin, and fibrinogen. We assume that prothrombinase is located along the injury zone and converts prothrombin to thrombin. Fibrin oligomers polymerize through either linear or branching reactions, eventually forming a fibrin gel. Fibrin gel is immobile and remains where it is formed. Due to its structure, the gel can affect blood flow and diffusion of other species.

2.1 Coagulation Proteins

Our simplification of the coagulation cascade involves only three species. Prothrombin, which is present in the blood, is converted to thrombin on the injury zone by prothrombinase. Fibrinogen, which is also present in the blood, is cleaved by thrombin to produce fibrin monomer. There are several different thrombin inhibitors present in the blood and this is represented by a single degradation term. Let Z_2 represent the zymogen prothrombin (because prothrombin is also known as Factor II), E_2 the enzyme thrombin, and F fibrinogen. Let z_2, e_2, and f denote their respective concentrations. We track the concentration of all three species as they diffuse, advect, and react at points $\mathbf{x}$ at time, t, by these equations

$$\frac{\partial z_2}{\partial t} + \nabla \cdot (\mathbf{u} z_2) = \nabla \cdot (D_z \nabla z_2) \tag{2.1}$$

$$\frac{\partial e_2}{\partial t} + \nabla \cdot (\mathbf{u} e_2) = \nabla \cdot (D_z \nabla e_2) - k_{at} e_2 \tag{2.2}$$

$$\frac{\partial f}{\partial t} + \nabla \cdot (\mathbf{u} f) = \nabla \cdot (D_f \nabla f) - \frac{k_f e_2 f}{k_{fs} + f}. \tag{2.3}$$

Here, $\mathbf{u}$ is the fluid velocity, k_{at} is the rate of thrombin inhibition, k_{fs} is the half-

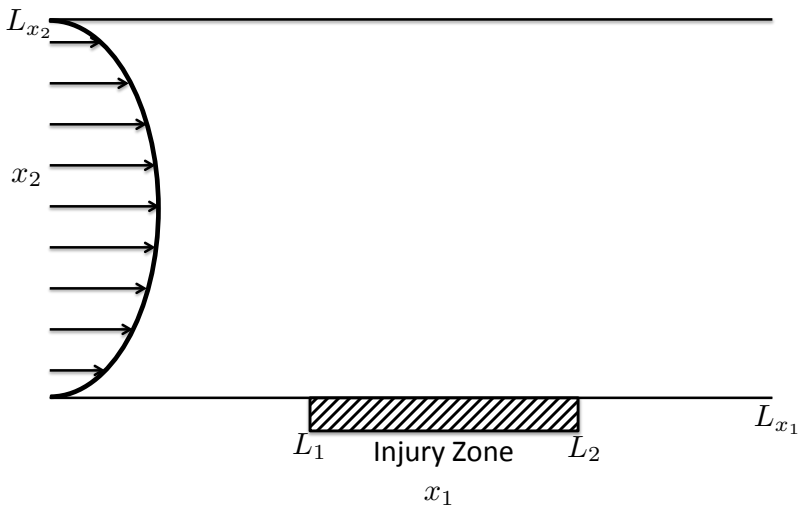

Figure 2.1: Model domain includes an injury zone located in the center along the bottom wall.

saturation concentration, and k_f is the reaction rate for fibrinogen cleavage. Because thrombin is a cleaved form of prothrombin, we assume that they have the same diffusivity, D_z and fibrinogen has diffusivity D_f.

The injury zone contains a density of wall-bound prothrombinase. We assume that prothrombin can diffuse and advect to the wall and bind to and unbind from prothrombinase. While bound, prothrombin can be cleaved to become thrombin. When this happens, thrombin is immediately released into the fluid. We also assume that the prothrombin-prothrombinase system is in quasi-steady state. (A dynamic version of this system will be discussed later.) The quasi-steady state relations lead to the boundary conditions for z_2 and e_2 in the injury zone. The complete set of boundary conditions for z_2, e_2, and f are as follows.

For z_2,

$$z_2(0,x_2,t) = z_2^{up}, \quad \frac{\partial z_2(L_{x_1},x_2,t)}{\partial x_1}=0, \quad \frac{\partial z_2(x_1,L_{x_2},t)}{\partial x_2}=0, \tag{2.4}$$

$$-D_z\frac{\partial z_2(x_1,0,t)}{\partial x_2} = \begin{cases} 0, & \text{for } x_1 < L_1, x_1 > L_2 \\ \frac{-\alpha z_2}{\beta+z_2}, & \text{for } L_1 \le x_1 \le L_2. \end{cases} \tag{2.5}$$

For e_2,

$$e_2(0,x_2,t) = 0, \quad \frac{\partial e_2(L_{x_1},x_2,t)}{\partial x_1}=0, \quad \frac{\partial e_2(x_1,L_{x_2},t)}{\partial x_2}=0, \tag{2.6}$$

$$-D_z\frac{\partial e_2(x_1,0,t)}{\partial x_2} = \begin{cases} 0, & \text{for } x_1 < L_1, x_1 > L_2 \\ \frac{\alpha z_2}{\beta+z_2}, & \text{for } L_1 \le x_1 \le L_2. \end{cases} \tag{2.7}$$

For f,

$$f(0,x_2,t) = f^{up}, \quad \frac{\partial f(L_{x_1},x_2,t)}{\partial x_1}=0, \tag{2.8}$$

$$\frac{\partial f(x_1,L_{x_2},t)}{\partial x_2} = 0, \quad -D_f\frac{\partial f(x_1,0,t)}{\partial x_2}=0.$$

Here, α is a function of the cleavage rate and the concentration of prothrombinase, while β is a function of the binding, unbinding, and cleavage rates. The coagulation proteins yield a source rate of fibrin monomer, $S_{10} = \frac{k_f e_2 f}{k_{fs}+f}$.

2.2 Fibrin Oligomers and Gel

Once fibrin monomers are produced from the coagulation protein, they spontaneously polymerize. The polymerization process yields a fibrin gel. In order to model the formation of a gel, we begin with the condensation reactions of fibrin oligomers. Describing these reactions leads to a doubly infinite set of partial differential equations for concentrations

of oligomers of all sizes and number of branches. Next, we use a generating function to transform the doubly infinite set of PDEs to a system of two PDEs. We next explain how these equations are modified to capture our assumption about reactions involving the gel. Finally, we derive equations that allow us to track structural quantities such as branch point density and mass of fibrin. The boundary conditions for the gelation PDEs are discussed at the end of this section.

2.2.1 Fibrin Condensation Reaction

We assume fibrin polymerizes in two ways, through linear reactions and branching reactions as in [11]. There are two steps to each of these reactions. First, two fibrin monomers bind center to tail; then they can either "zip" together to complete a linear reaction or another monomer can join in a branching reaction. This is depicted in Figure 2.2. We do not explicitly track the two steps, but instead postulate a rate of linear reaction that is a reaction involving two reaction sites on oligomers and a rate of branching that involves three such reactive sites. In general, we want to consider oligomers of any size with any number of branch points. For integers, $m = 1, 2, \ldots$ and $b = 0, 1, \ldots$, let $C_{m,b}$ denote an oligomer with b branch points and $m + 2b$ monomers and let c_{mb} denote the concentration of these oligomers. For example, using this naming convention, monomers are $C_{1,0}$ and oligomers with three branch points and eight monomers are $C_{2,3}$. We track the concentration c_{mb} using the following condensation equation:

$$\begin{aligned}
\frac{\partial c_{mb}(\mathbf{x},t)}{\partial t} = & - \nabla\cdot(\mathbf{u}c_{mb}) + \nabla\cdot(D_{mb}\nabla c_{mb}) \\
& + \frac{k_l}{2}\sum_{\{b_1+b_2=b\}}\ \sum_{\{m_1+m_2=m\}}(b_1+2)(b_2+2)c_{m_1b_1}c_{m_2b_2} \\
& - k_l(b+2)c_{mb}\sum_{b_1}\sum_{m_1}(b_1+2)c_{m_1b_1} \\
& + \frac{k_b}{6}\sum_{\{b_1+b_2+b_3=b-1\}}\ \sum_{\{m_1+m_2+m_3=m+2\}}(b_1+2)(b_2+2)(b_3+2)c_{m_1b_1}c_{m_2b_2}c_{m_3b_3} \\
& - \frac{k_b}{2}(b+2)c_{mb}\sum_{b_1,b_2}\sum_{m_1,m_2}(b_1+2)(b_2+2)c_{m_1b_1}c_{m_2b_2} \\
& + S_{mb}.
\end{aligned} \tag{2.9}$$

Here k_l is the rate of linear binding and k_b is the rate of branch point formation. The first line of 2.9 describes changes due to advection and diffusion. Note that the diffusion coefficient can be different for each oligomer. The second line of 2.9 describes the linear reaction of two appropriate size oligomers that bind to form an oligomer of size c_{mb}. Oligomers c_{mb}

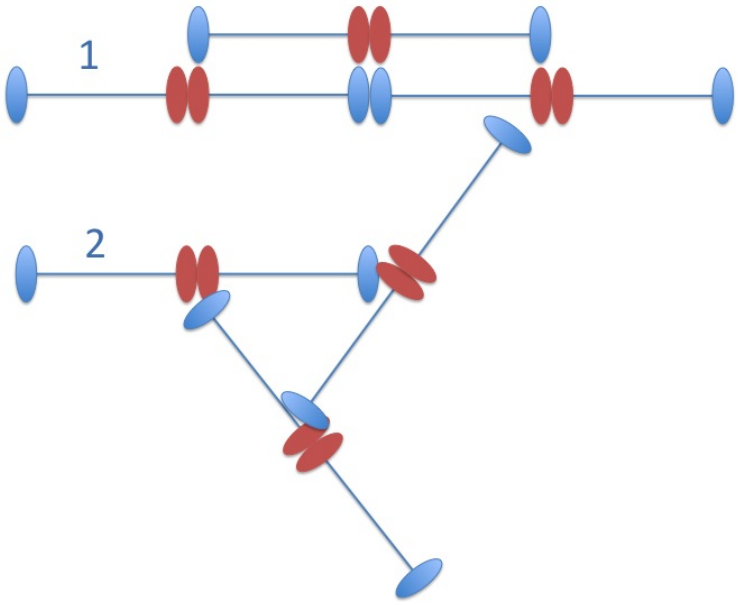

Figure 2.2: Linear and branching binding diagram. Fibrin monomers can polymerize in one of two ways: 1) Linear Binding, where two monomers zip together to form a linear oligomer and 2) Branching Reaction, where three monomers come together to form a branch point.

have $b+2$ end points or reactive sites and we assume that the rate of linear binding of two types of oligomers is proportional to the product of concentrations of reactive sites on each. The third line of 2.9 describes the rate at which three appropriately sized oligomers coming together to form an oligomer of C_{mb}. The fourth line of 2.9 describes C_{mb} oligomers binding with any two oligomers to form a branch point. The final line is the source rate S_{mb}. The only source in the system is for fibrin monomers at a rate S_{10} and describes the thrombin-mediated conversion of fibrinogen to fibrin monomers.
Let R_s be the total number of reactive sites on oligomers. Then

$$R_s = \sum_{m,b}(b+2)c_{mb} \tag{2.10}$$

We can rewrite equations 2.9 as

$$\begin{aligned}
\frac{\partial c_{mb}(\mathbf{x},t)}{\partial t} = & - \nabla\cdot(\mathbf{u}c_{mb}) + \nabla\cdot(D_{mb}\nabla c_{mb}) \\
& + \frac{k_l}{2}\sum_{\{b_1+b_2=b\}}\ \sum_{\{m_1+m_2=m\}}(b_1+2)(b_2+2)c_{m_1b_1}c_{m_2b_2} \\
& - k_l(b+2)\,c_{mb}\,R_s \\
& + \frac{k_b}{6}\sum_{\{b_1+b_2+b_3=b-1\}}\ \sum_{\{m_1+m_2+m_3=m+2\}}(b_1+2)(b_2+2)(b_3+2)c_{m_1b_1}c_{m_2b_2}c_{m_3b_3} \\
& - \frac{k_b}{2}(b+2)\,c_{mb}\,R_s^2 \\
& + S_{mb}.
\end{aligned} \tag{2.11}$$

The boundary conditions for c_{mb} are

$$\begin{aligned}
c_{mb}(0,x_2,t) &= 0, \quad \frac{\partial c_{mb}(L_{x_1},x_2,t)}{\partial x_1} = 0, \\
\frac{\partial c_{mb}(x_1,L_{x_2},t)}{\partial x_2} &= 0, \quad -D_{mb}\frac{\partial c_{mb}(x_1,0,t)}{\partial x_2} = 0.
\end{aligned} \tag{2.12}$$

2.2.2 Gelation

Equations 2.11 and 2.10 describe the process of polymerization but only describe reactions among finite length oligomers. We want to extend the reactions beyond a time when a gel forms (described below). For now suppose there is a gel and that R_g is the concentration of reactive sites in it. Then we modify equation 2.11 to allow for reaction involving reactive sites on finite size oligomers and reactive sites in the gels.

$$\begin{aligned}
\frac{\partial c_{mb}(\mathbf{x},t)}{\partial t} = & - \nabla\cdot(\mathbf{u}c_{mb}) + \nabla\cdot(D_{mb}\nabla c_{mb}) \\
& + \frac{k_l}{2}\sum_{b_1+b_2=b}\sum_{m_1+m_2=m}(b_1+2)(b_2+2)c_{m_1b_1}c_{m_2b_2} \\
& - k_l(b+2)c_{mb}R_s \\
& - k_l(b+2)c_{mb}R_g \\
& + \frac{k_b}{6}\sum_{b_1+b_2+b_3=b-1}\sum_{m_1+m_2+m_3=m+2}(b_1+2)(b_2+2)(b_3+2)c_{m_1b_1}c_{m_2b_2}c_{m_3b_3} \\
& - \frac{k_b}{2}(b+2)c_{mb}R_s^2 \\
& - k_b(b+2)c_{mb}R_g\sum_{m_1}\sum_{b_1}(b_1+2)c_{m_1b_1} \\
& + S_{mb}.
\end{aligned} \tag{2.13}$$

The fourth line of 2.13 describes linear binding of the C_{mb} oligomer with the gel. The seventh line of 2.13 describes C_{mb} oligomer binding with a reactive site in the gel and with another oligomer to form a branch point. Notice that equation 2.13 does not allow for any rings or loops to form (i.e., two reactive sites on the same oligomer cannot bind together and two gel reactive sites cannot bind together).

Equation 2.13 is a doubly infinite system of PDE's. To study it, we follow the approach in [42] and [11] and introduce a generating function which is a power series in two dummy variables y and z with the concentration $c_{mb}(\mathbf{x},t)$ as coefficients.

$$g(\mathbf{x},t,y,z) = \sum_{m,b} y^m z^{b+2} c_{mb}. \tag{2.14}$$

Values of $g(\mathbf{x},t,y,z)$ for z values between 0 and 1 at y values near $y=1$ are all that will be needed below. Under the assumption that all finite-sized oligomers advect and diffuse the same, equation 2.13 can be used to show that the generating function satisfies the PDE

$$\begin{aligned}
\frac{\partial g}{\partial t} = & - \nabla\cdot(\mathbf{u}g) + \nabla\cdot(D_c\nabla g) \\
& + \frac{k_l}{2}\left(\frac{\partial g}{\partial z}\right)^2 - k_l z\frac{\partial g}{\partial z}R + \frac{k_b}{6}y^{-2}\left(\frac{\partial g}{\partial z}\right)^3 \\
& - \frac{k_b}{2}z\frac{\partial g}{\partial z}\left(R^2 - R_g^2\right) + yz^2S_{10},
\end{aligned} \tag{2.15}$$

where $R \equiv R_s + R_g$. We assume that once gel is created it is stationary, it neither advects nor diffuses. Then R evolves because of advection and diffusion of finite sized oligomers and because of reactions among finite sized oligomers and finite sized oligomers and gel.

$$\begin{aligned}\frac{\partial R(\mathbf{x},t)}{\partial t} = &- \nabla\cdot(\mathbf{u}R_s) + \nabla\cdot(D_c\nabla R_s) \\ &- k_l\left(R^2 - R_g^2\right) - \frac{k_b}{2}\left(R^3 - \left(3R_sR_g^2 + R_g^3\right)\right) + 2S_{10}\end{aligned} \tag{2.16}$$

The first term in the second line of 5.19 describes the rate that reactive sites are lost due to linear reactions. Linear reactions cannot occur between two gel reactive sites. Therefore it is subtracted off. The second term describes the rate reactive sites are lost due to branch point formation. Again, reactive sites in the gel cannot react so the terms must be subtracted off.

We perform a change of variables

$$\widetilde{W}(\mathbf{x},t,y,z) = g_z(\mathbf{x},t,y,z) - zR(\mathbf{x},t). \tag{2.17}$$

From equations 2.15 and 5.19,

$$\begin{aligned}\frac{\partial\widetilde{W}}{\partial t} = &- \nabla\cdot\left(\mathbf{u}\left(\widetilde{W} - z\widetilde{W}\big|_{y=z=1}\right)\right) + \nabla\cdot\left(D_c\nabla\left(\widetilde{W} - z\widetilde{W}\big|_{y=z=1}\right)\right) \\ &+ \left\{\frac{k_l}{2}\widetilde{W}^2 + \frac{k_b}{2y^2}\left(\frac{1}{3}\widetilde{W}^3 + z\widetilde{W}^2R + z^2R^2\widetilde{W}\right) - \frac{k_b}{2}z(R^2 - R_g^2)(\widetilde{W} + zR)\right\}_z \\ &- k_lzR_g^2 - \frac{k_b}{2}\left(-zR^3 + 3zR_sR_g^2 + zRg^3\right) + \frac{k_b}{2y^2}z^2R^3.\end{aligned} \tag{2.18}$$

For reasons explained below, define $\widetilde{V}(\mathbf{x},t,y,z) = \widetilde{W}_y(\mathbf{x},t,y,z)$. It turns out that only values of $\widetilde{W}$ and $\widetilde{V}$ for $y = 1$ are needed. So let $W(\mathbf{x},t,z) = \widetilde{W}(\mathbf{x},t,y=1,z)$ and $V(\mathbf{x},t,z) = \widetilde{V}(\mathbf{x},t,y=1,z)$. Then $W(\mathbf{x},t,z) = g_z(\mathbf{x},t,y=1,z) - zR(\mathbf{x},t)$. Computing $g_z\big|_{y=1}$ from the definition of g, we see $g_z\big|_{y=z=1} = R_s$. And implies $W(\mathbf{x},t,1) = R_s - R = R_s - (R_s + R_g) = -R_g$. Hence, we obtain the gel reactive site concentration from $R_g = -W\big|_{z=1}$. From 2.18, we can deduce that

$$\begin{aligned}\frac{\partial W}{\partial t} = &- \nabla\cdot\left(\mathbf{u}\left(W - zW\big|_{z=1}\right)\right) + \nabla\cdot\left(D_c\nabla\left(W - zW\big|_{z=1}\right)\right) \\ &+ \left\{\frac{k_l}{2}W^2 + \frac{k_b}{2}\left(\frac{1}{3}W^3 + zW^2R + z^2R^2W\right) - \frac{k_b}{2}z(R^2 - R_g^2)(W + zR)\right\}_z \\ &- k_lzR_g^2 - \frac{k_b}{2}\left(-zR^3 + 3zR_sR_g^2 + zRg^3\right) + \frac{k_b}{2}z^2R^3.\end{aligned} \tag{2.19}$$

$$\begin{aligned}\frac{\partial V}{\partial t} = & - \nabla\cdot(\mathbf{u}V) + \nabla\cdot(D_c\nabla V) \\ & + \left\{\left(k_l W + \frac{k_b}{2}(W+zR)^2 - \frac{k_b}{2}z(R^2-R_g^2)\right)V\right\}_z \\ & - k_b\left\{(W+zR)^2(W_z+R)\right\} + 2zS_{10}.\end{aligned} \tag{2.20}$$

2.2.3 Structural Quantities

We are interested in tracking the concentration of branch points of finite size oligogmers in the sol and the concentration of branch points in the gel as well as the concentration of fibrin mass in the sol and in the gel. The concentration of branch points in the sol is $B_s = \sum_{mb} bc_{mb}$ which can be rewritten in terms of g and W,

$$\begin{aligned} B_s &= g_z(t,\mathbf{x},1,1) - 2g(t,\mathbf{x},1,1) && (2.21)\\ &= W(t,\mathbf{x},1) - 2\int_0^1 W(t,\mathbf{x},z')dz'. && (2.22)\end{aligned}$$

Let $B = B_s + B_g$, where B_g is the concentration of branch points in the gel. Since gel is fixed, B evolves according to

$$\frac{\partial B}{\partial t} = -\nabla\cdot(\mathbf{u}B_s) + \nabla\cdot(D_c\nabla B_s) + \frac{k_b}{6}\left(R^3 - \left(3R_sR_g^2 + R_g^3\right)\right), \tag{2.23}$$

and we can compute B_g by $B_g = B - B_s$. The reaction term in 2.23 is the rate of branch point formation. One way to explain the coefficient of $1/6$ is using equation 5.19. For every branch point formed, there is a loss of three reactive sites. The rate of branch point formation is a third of rate of reactive site lost due to such reaction.

The mass density of fibrin, θ_s, in the sol is defined as $\theta_s = \sum_{mb}(m+2b)c_{mb}$, i.e., the total number of monomer unites in finite size oligomers. It can be described in terms of g, W, and V,

$$\begin{aligned} \theta_s &= g_y(\mathbf{x},t,1,1) + 2g_z(\mathbf{x},t,1,1) - 4g(\mathbf{x},t,1,1) && (2.24)\\ &= \int_0^1 V(\mathbf{x},t,z')dz' + 2W(\mathbf{x},t,1) - 4\int_0^1 W(\mathbf{x},t,z')dz'. && (2.25)\end{aligned}$$

We let the total mass density of fibrin be defined as $\theta = \theta_s + \theta_g$, where θ_g is the mass density of fibrin in the gel. Since θ_g is stationary, θ evolves according to

$$\frac{\partial\theta}{\partial t} = -\nabla\cdot(\mathbf{u}\theta_s) + \nabla\cdot(D_c\nabla\theta_s) + S_{10}. \tag{2.26}$$

2.2.4 Boundary Conditions for Gelation Equations

The boundary conditions of the gelation the state variables, W, V, R, B, and θ, depend on the boundary conditions of c_{mb}. Since all oligomers are created within the domain, the upstream concentration of the state variables is zero,

$$W(0, x_2, t, z) = V(0, x_2, t, z) = R(0, x_2, t) = B(0, x_2, t) = \theta(0, x_2, t) = 0 \tag{2.27}$$

From the downstream boundary conditions for c_{mb}, we see that homogenous Neumann conditions hold at $x_1 = L_{x_1}$ for all state variables. From the definitions of W and V, $W(\mathbf{x}, t, 0) = V(\mathbf{x}, t, 0) = 0$. No boundary conditions are (or can be) imposed on W and V at $z = 1$ because advection of W and V in z is from left to right.

The derivation of the boundary conditions along the top and bottom walls is more complicated. Recall that we assume that there is no flux of oligomers through the vessel walls. Further, the velocity $\mathbf{u}$ at which oligomers advect vanishes at these walls. Therefore, at $x_2 = 0$ and $x_2 = L_{x_2}$

$$-D_c \frac{\partial c_{mb}}{\partial x_2} = 0. \tag{2.28}$$

The total concentration of reactive sites, R, is the sum of the concentrations of reactive sites in the gel, R_g and reactive sites in the sol, R_s. Because reactive sites in the gel do not advect or diffuse, the total flux of reactive sites must be equal to the flux of reactive sites in the sol. Therefore,

$$R_t = -\nabla \cdot J_R + \text{Reactions} \tag{2.29}$$

$$= -\nabla \cdot J_{R_s} + \text{Reactions} \tag{2.30}$$

This observation was used already in equation 5.19. Because R_s advects and diffuses, J_{R_s} is described by

$$J_{R_s} = \mathbf{u} R_s - D_c \nabla R_s. \tag{2.31}$$

At the wall, $\mathbf{u}$, is zero so the advective flux here vanishes. From the definition, $R_s = \sum_{m,b} c_{mb}$, it follows

$$-D_c \frac{\partial R_s}{\partial x_2} = -D_c \sum_{m,b} (b+2) \frac{\partial c_{mb}}{\partial x_2} \tag{2.32}$$

Therefore, along the top and bottom walls

$$-D_c \frac{\partial R_s}{\partial x_2} = 0. \tag{2.33}$$

This implies $J_{R_s} = 0$ along these walls. However, for equation 5.19, we need a boundary condition on R. Substituting $R_s = R - R_g$ into equation 2.31 , $\mathbf{u} = 0$, and $\frac{\partial R_s}{\partial x_2} = 0$ along the top and bottom walls we find that

$$-D_c\frac{\partial R}{\partial x_2} = -D_c\frac{\partial R_g}{\partial x_2} \tag{2.34}$$

for $(x_1, 0, t)$ and (x_1, L_{x_2}, t).

The boundary conditions for W along the top and bottom wall can be derived similarly. From equation 2.19 for W, we see that the flux of W in the (x_1, x_2) plane is

$$J_w = \left(\mathbf{u}\left(W - zW\big|_{z=1}\right)\right) - \left(D_c\nabla\left(W - zW\big|_{z=1}\right)\right). \tag{2.35}$$

Again, $\mathbf{u} = 0$ along the top and bottom wall so the advection term vanishes. We use the definition of W to find the boundary value of the second flux term. Recall that $W = \widetilde{W}\big|_{y=1}$ where $\widetilde{W} = g_z - zR$. Taking the appropriate derivatives,

$$\frac{\partial\widetilde{W}}{\partial x_2} = \frac{\partial g_z}{\partial x_2} - z\frac{\partial R}{\partial x_2} \tag{2.36}$$

From equation 2.34, $\frac{\partial R}{\partial x_2} = \frac{\partial R_g}{\partial x_2}$. From equation 2.14, we see that $g_z = \sum_{m,b}(b+2)y^m z^{b+1}c_{mb}$. Then,

$$\frac{\partial g_z}{\partial x_2} = \sum_{m,b}(b+2)y^m z^{b+1}\frac{\partial c_{mb}}{\partial x_2} = 0,$$

for $x_2 = 0$ and $x_2 = L_{x_2}$. Therefore along the top and bottom wall,

$$\frac{\partial W}{\partial x_2} = -z\frac{\partial R_g}{\partial x_2} \tag{2.37}$$

$$-D_c\frac{\partial W}{\partial x_2} = D_c z\frac{\partial R_g}{\partial x_2} \tag{2.38}$$

The boundary condition for V along the top and bottom wall can be derived from its definition. Recall that $\widetilde{V} = \widetilde{W}_y$. From equation 2.17,

$$\widetilde{W}_y = g_{zy} \tag{2.39}$$

From equation 2.14, we see that $g_{zy} = \sum_{m,b} m(b+2)y^{m-1}z^{b+1}c_{mb}$. Then,

$$\frac{\partial g_{zy}}{\partial x_2} = \sum_{m,b} m(b+2)y^{m-1}z^{b+1}\frac{\partial c_{mb}}{\partial x_2} = 0,$$

Therefore, for $x_2 = 0$ and $x_2 = L_{x_2}$,

$$-D_c\frac{\partial V}{x_2} = 0. \tag{2.40}$$

The boundary conditions for branch points, B, and total mass, θ, are derived in a similar way as for R. Along the top and bottom wall, the boundary conditions are,

$$-D_c\frac{\partial B}{\partial x_2} = -D_c\frac{\partial B_g}{\partial x_2}, \tag{2.41}$$

$$-D_c\frac{\partial \theta}{\partial x_2} = -D_c\frac{\partial \theta_g}{\partial x_2}. \tag{2.42}$$

2.2.5 Fluid

We model the fluid velocity using modified Navier-Stokes equations for incompressible fluid

$$\rho\left(\mathbf{u}_t + \mathbf{u}\cdot\nabla\mathbf{u}\right) = -\nabla p + \mu\Delta\mathbf{u} - \mu\alpha_1(\phi_g, B_g)\mathbf{u}, \tag{2.43}$$

$$\nabla\cdot\mathbf{u} = 0. \tag{2.44}$$

Here $\mathbf{u}(\mathbf{x},t)$ and $p(\mathbf{x},t)$ are the fluid velocity and pressure at position $\mathbf{x}$, at time t, respectively, and ρ and μ are the fluid mass density and the dynamic viscosity of the fluid, respectively. The term $-\mu\alpha_1\mathbf{u}$ is called a Brinkman term. Along the top and bottom wall, $\mathbf{u}$ is subject to no-slip boundary conditions. Poiseuille flow is prescribed as an inflow condition and a homogenous Neuman condition is prescribed on $\mathbf{u}$ for the outflow condition.

In adding the Brinkman term to the Navier-Stokes equations, we are modeling the gel as a porous medium which imposes a drag force on fluid moving through it. Porous media with high value of α_1, offer more resistance to a given flow and are less permeable. We chose α_1, so that it increases as the local gel volume fraction increases. We assume that the Brinkman term is also a function of branch point concentration and that the permeability decreases with increasing branch point density.

We seek to relate the resistant coefficient α_1 to the state variables θ_g and B_g which describe the local structure of the gel in our model. There is a large literature regarding flow through porous media made up of distributions of fibers. In these works, the permeability K (the reciprocal of the resistance coefficient α_1) is related to the volume fraction ϕ_g of the fibrous material and the typical fiber diameter a. These relationships are obtained by analysis of simplified fiber arrangements and/or empirical measurements in real fibrous media. Jackson and James [18] gave a review of this literature including several relationships between permeability and fiber volume fraction and diameter. While these relationships were obtained from pertubation theory assuming the volume fraction of fiber is small, comparisons with data from porous media shows these relationships hold for volume fraction up to $\phi_g = 0.3$. The different fiber arrangements yield the same relationships to leading order. Therefore, we choose to use the relationships describing permeability of a porous medium formed by circular rods parallel to flow,

$$K = \frac{a^2}{4\phi_g}\left(-\ln\phi_g - \frac{3}{2} + 2\phi_g - \frac{\phi_g^2}{2}\right). \tag{2.45}$$

Here a is the diameter of the fiber. To make use of this formula we define the gel volume fraction to be

$$\phi_g = N_a V_f \theta_g. \tag{2.46}$$

The term N_a is Avogadros number and V_f is the volume of a single fibrin monomer. After making several geometric assumptions, the pore size of the gel P, and the diameter of the fibers, a, can be related to the gel volume fraction and branch point concentration by,

$$P = \frac{F_B(B_g)}{1 + F_\phi(\phi_g)} \tag{2.47}$$

$$a = F_\phi(\phi_g) P \tag{2.48}$$

where $F_B(B_g) = \frac{2}{3^{1/4}(N_a B_g)^{1/3}}$, $F_\phi(\phi_g) = -\frac{3\phi_g + 3^{7/8}\sqrt{\pi\phi_g}}{-3^{3/4}\pi + 3\phi_g}$. The derivation of fiber diameter and pore size can be found in Appendix A.

2.3 Summary

The model consists of three coagulation proteins z_2, e_2, and f that produce a source rate of fibrin monomers, then two gelation variables, W and R, describe monomers polymerizing to form fibrin oligomers then gel, and three structural variables, V, θ, and B, describe how the gel is changing over time. These reactions occur in fluid that is modelled using the modified Navier-Stokes equations that includes feedback from the fluid through a Brinkman term. Next we describe the results of simulating this model.

CHAPTER 3

RESULTS

Using the model described in Chapter 2, we want to examine the process of fibrin clot formation. We look at three model scenarios, no flow, flow, and protected flow. Within the first and third scenarios, we explore the rate of branch formation and the rate of thrombin production, and we vary the upstream fibrinogen concentration.

We look at events in a blood vessel segment of length $400\,\mu m$ and height $100\,\mu m$. The injury zone is located in the center of the lower wall and is $80\,\mu m$ long. The simulations begin with prothrombin and fibrinogen having homogenous concentrations equal to their upstream concentrations. The initial boundary conditions must be consistent with these initial conditions. While this is trivial for most boundary conditions, the nonlinear Robin boundary condition for z_2 requires an initialization period. At $t = 0$, we set $\alpha = 0$. The rate α is then increased for the first $50\,s$ by which time it reaches the desired value.

3.1 No Flow

We begin by looking at fibrin formation when the fluid velocity is identically zero. Prothrombin and fibrinogen are initially uniformly distributed in the domain. Prothrombin is converted to thrombin on the injured wall and then diffuses away from that wall. Fibrin monomer is produced where fibrinogen and thrombin co-exist. Figure 3.1 shows the thrombin and fibrinogen concentrations, and monomer source rate at $t = 100$ s. At this time, thrombin is concentrated near the lower wall and fibrinogen is depleted there. As a result, the largest source rate occurs away from the wall at the left and right edges of the injury zone. In fact this is true for all time. Figure 3.2 shows snapshots in time of the fibrin source rate. To orient the reader, the injury zone is marked in red. Initially there is no source. As thrombin diffuses outward and fibrinogen is depleted from the region near the wall, fibrin monomer is produced further from the injury. This occurs until the fibrinogen above the injury zone is sufficiently depleted, and then substantial fibrin monomer production is limited to the left and right edges of the injury and the source strength decreases with time. As shown below, the source rate of fibrin monomer strongly influences the spatial

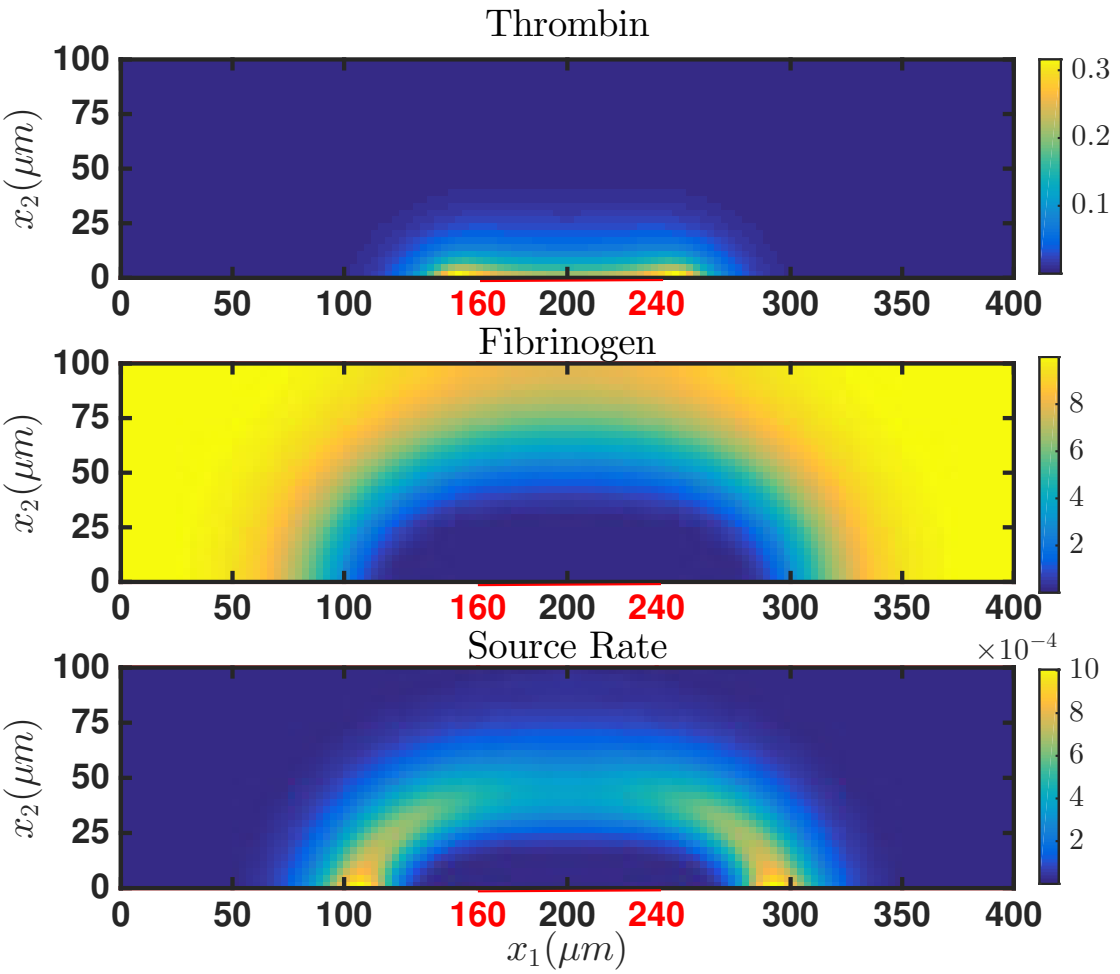

Figure 3.1: Fibrin monomer production without flow. The top plot is the thrombin concentration distribution (e_2) in (μM). The middle plot is the fibrinogen concentration distribution (f) in (μM). The bottom plot is the fibrin monomer production rate, (S_{10}) in ($\mu M/s$). The injury zone is denoted in red. $\alpha = 10^{-5}$ cm $\mu M/s$, $k_b = 10\mu M^{-2}s^{-1}$, $f^{up} = 10\mu M$

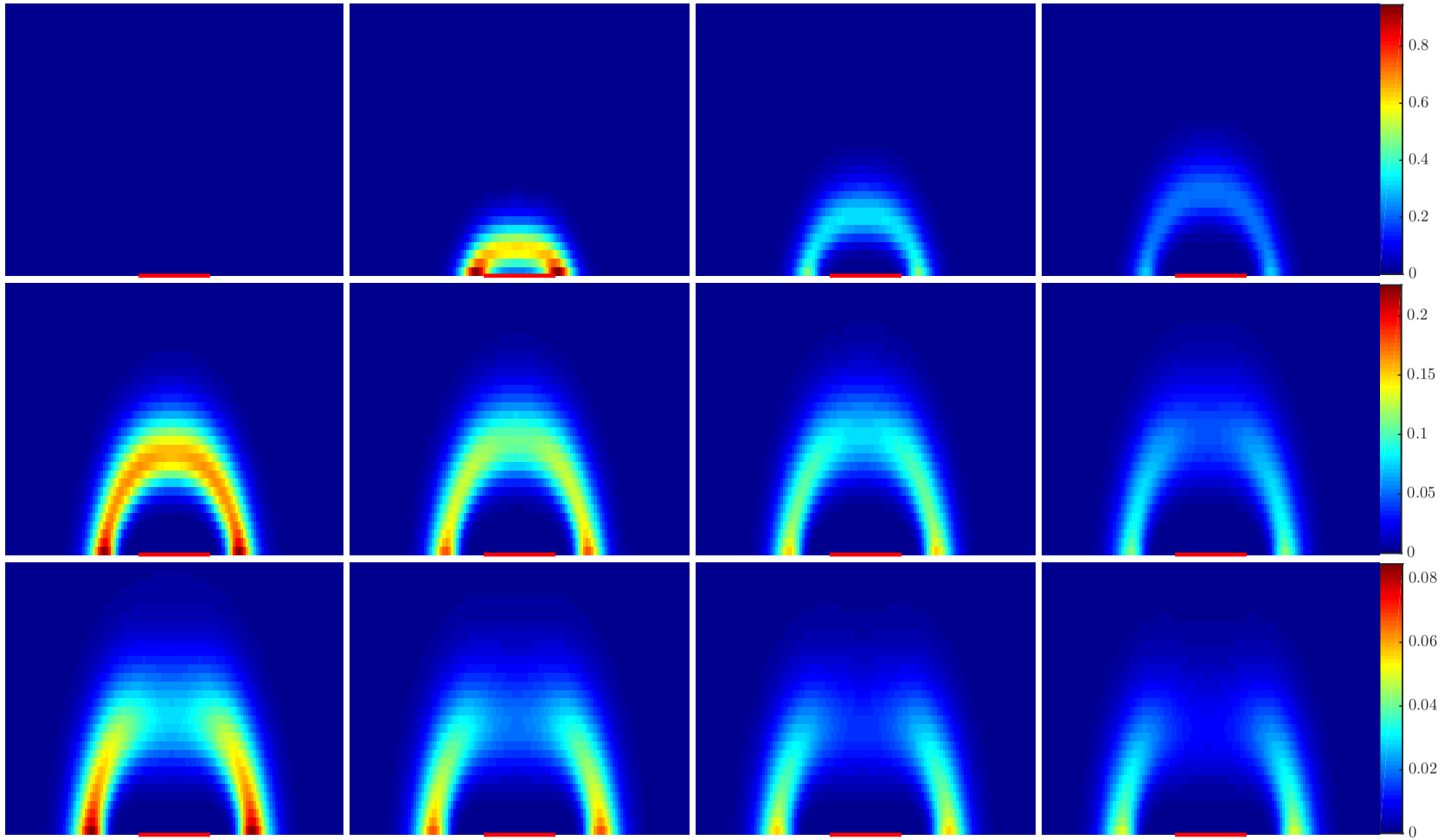

Figure 3.2: Fibrin source rate snapshot without flow. Sequence of snapshots of the fibrin source rate ($\mu M s^{-1}$). From left to right, $t = 0$, 10, 20, 30, 40, 50, 60, 80, 110, 150, 200, and 250 s. Notice the scale is different for each row.$\alpha = 10^{-5}$ cm $\mu M/s$, $k_b = 10\mu M^{-2}s^{-1}$, $f^{up} = 10\mu M$

distribution of the branch point and fibrin mass density and, in turn, they affect the pore size and fiber diameter.

The gel first forms above the injury zone and then grows radially. The gel or clotting time at each spatial location is shown in Figure 3.3.

The high initial fibrin source above the injury site causes a high concentration of sol branch points to form there that eventually become incorporated in the gel. Figure 3.4 shows that at $t = 500\,s$, most of the branch points are contained in the gel. The fibrin mass density however has a very different distribution profile. Because fibrin is supplied to the outer edges of the injury zone at a high rate, fibrin continues to bind even after a gel has formed. This leads to a higher density of fibrin in the lower left and right edges of the gel, as shown in Figure 3.4. Eventually, the fibrinogen is depleted from the right side of the domain but because the boundary condition on f at $x_1 = 0$ is $f = f^{up}$, fibrinogen diffuses from that boundary leading to an asymmetrical gel.

The variability in the distributions of fibrin mass and branch points in the gel leads to a wide range of pore sizes and fiber diameters. Figure 3.5 shows that the highly branched portion of the gel that is located near the wall has smaller fiber diameters than elsewhere. This is consistent with experiments [32] in which region of high branch point density coincided with regions of smaller fiber diameters. The areas with high fiber mass are formed from fibrin production rates were low and have thick fibers and small pores. For some parameters, including the branch point formation rate k_b, we do not have estimates from the literature. Other parameters, e.g., the rate of thrombin production α or the plasma concentration of fibrinogen f^{up}, will naturally vary. We next look at how variation in k_b, α and f^{up} affects fibrin gel formation.

3.1.1 Thrombin Production Rate

The thrombin production rate α is an element in the Michaelis-Menten rate that mediates thrombin flux at the injury zone. When the prothrombin concentration is high (i.e., close to z^{up}), the flux of thrombin is approximately α. This is the scenario at the beginning of a simulation. As prothrombin becomes depleted, the flux of thrombin asymptotes to $\frac{\alpha}{\beta} z_2$. With larger values of α, prothrombin near the wall is depleted faster. The balance between depletion and diffusion is the essential concern.

We look at varying α over two orders of magnitude. A reasonable hypothesis is that a larger α would yield a faster growing clot and higher thrombin concentration. Also, from biological experiments it is reasonable to expect that the higher thrombin concentrations

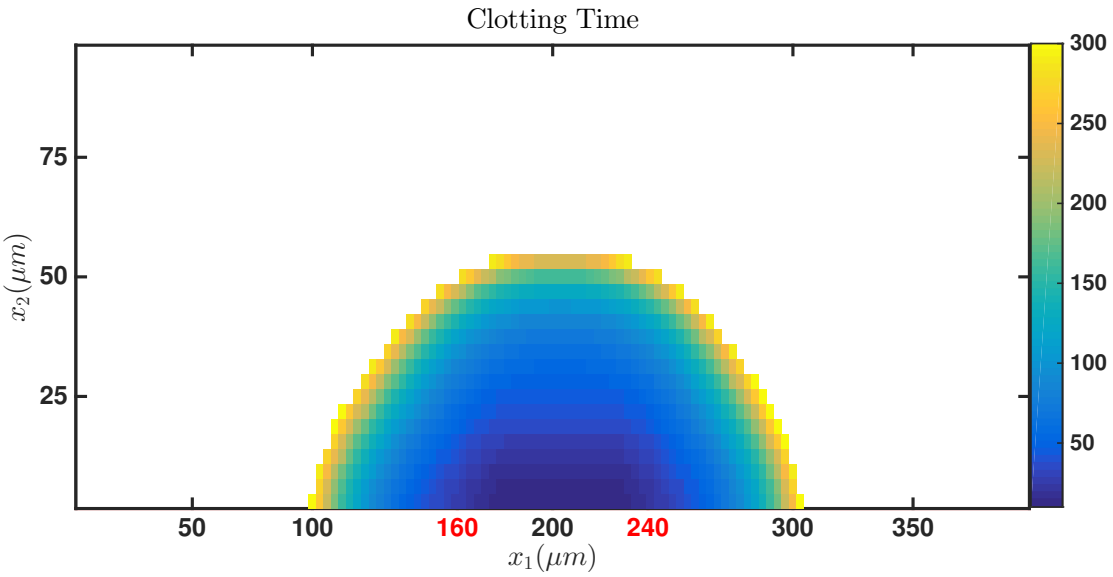

Figure 3.3: Clotting time distribution without flow. It is shown in seconds. The injury zone is marked in red. $\alpha = 10^{-5}$ cm $\mu M/s$, $k_b = 10\mu M^{-2}s^{-1}$, $f^{up} = 10\mu M$

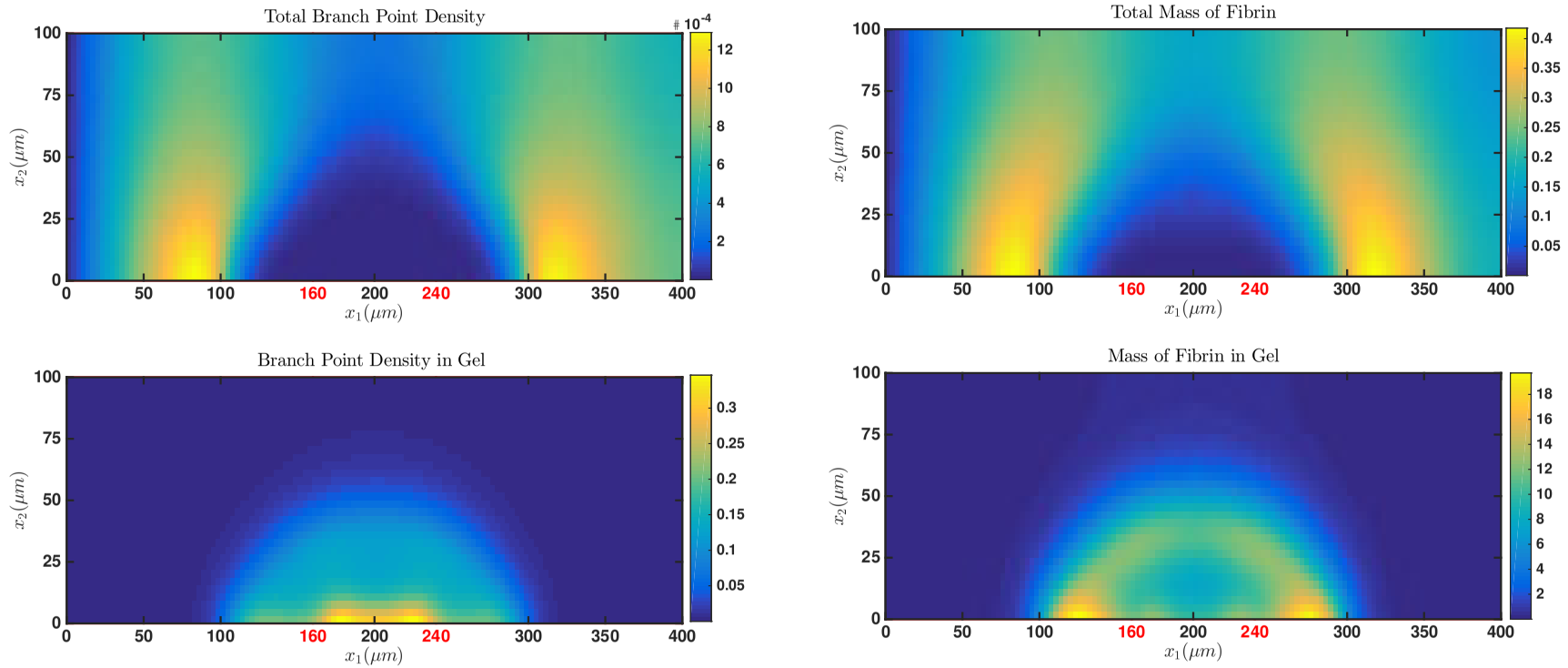

Figure 3.4: Branch point and fibrin mass density distributions without flow. Top left: Branch point density in the sol, B_s. Bottom Left: Branch point density in the gel, B_g. Top right: Fibrin mass density in the sol θ_s. Bottom right: Fibrin mass density in the gel. The concentrations are in (μM) and ploted at $t = 500s$. $\alpha = 10^{-5}$ cm $\mu M/s$, $k_b = 10\mu M^{-2}s^{-1}$, $f^{up} = 10\mu M$

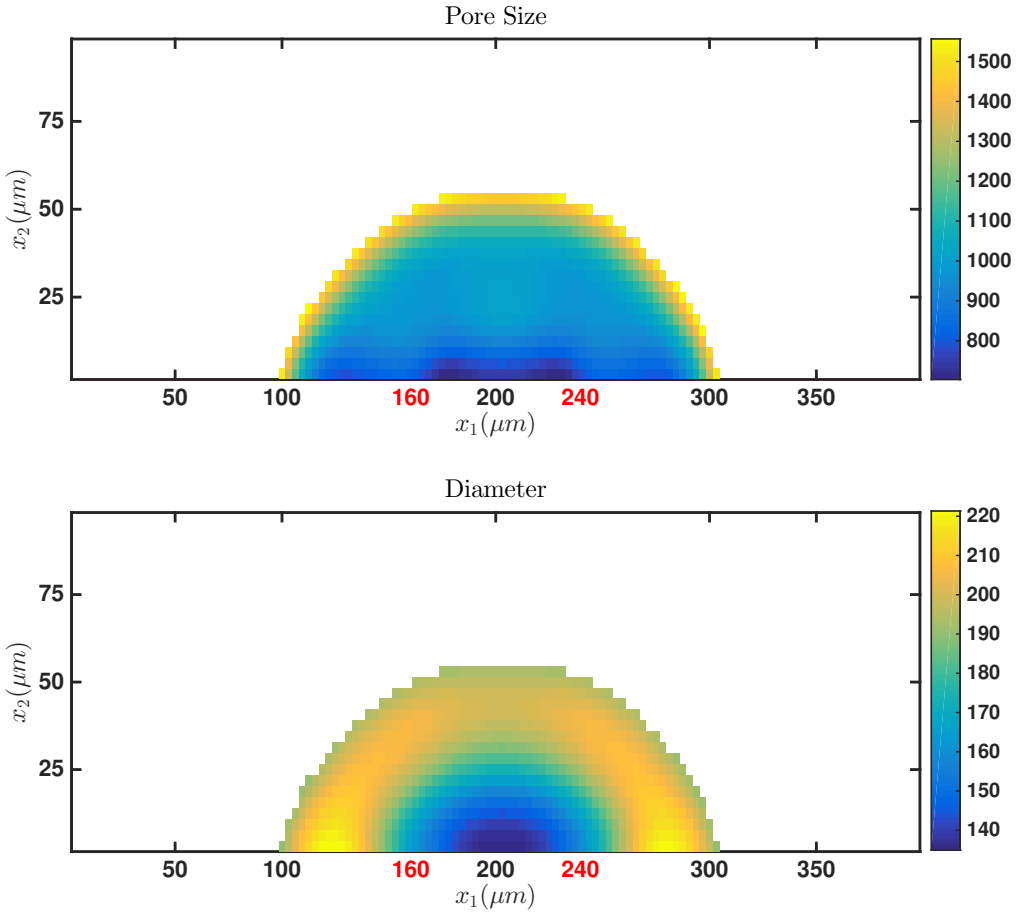

Figure 3.5: Pore size and fiber diameter without flow in (nm).$\alpha = 10^{-5}$ cm $\mu M/s$, $k_b = 10\mu M^{-2}s^{-1}$, $f^{up} = 10\mu M$

will result in higher branch point density and thinner fibers in clots as compared to a lower thrombin concentration.

Initially, larger α does produce more thrombin. However, once the prothrombin near the wall is depleted, the conversion of prothrombin to thrombin becomes limited by the rate that prothrombin diffuses to the wall. Figure 3.6 shows the maximum and average thrombin concentration over the entire domain verses time.

All of the maximum concentrations occur at the wall. The sharp peak occurs when prothrombin that started near the wall is depleted. For later times, there is a higher maximum and average concentration of thrombin for smaller α. The maximum of the thrombin concentration over time and x_1 increases with α but decreases as one moves away from the wall.

Higher thrombin concentration does result in a higher branch point density. As shown in Figure 3.7, near the wall, there is a high branch point density for all values of α, and this near wall density also increases with α. Away from the wall the branch point density is similar for the various α's. Clotting also occurs sooner near the wall for larger values of α due to the high thrombin concentration that results. However, away from the wall clotting occurs at about the same time for different values of α (Figure 3.8). This is explained by the limited variations in thrombin concentration across α's away from the wall. Overall, the fibrin mass density distributions shown in Figure 3.9 vary little or the different α's, with the greatest difference being a somewhat larger area of maximal fiber density above the injury site.

Interestingly, the fibrin mass density is approximately uniform while the branch point density varies for different values of α. Fibrinogen is depleted near the injury zone and is only supplied through diffusion. The Damköhler number is greater than one for all values of α investigated, implying that the rate of depletion is faster than the rate of transport. In fact, the Damköhler number is greater than one for all reaction-diffusion processes in this system. Because the rate of diffusive transport is slow, the same amount of fibrinogen becomes fibrin and becomes incorporated in the gel.

Because the rate of thrombin production (and consequently fibrin monomer production) yields different branch point densities for different values of α but similar fibrin mass densities, the pore size and the fiber diameter vary with α. The central core of the clot is more significantly affected than other regions. As shown in Figure 3.10, for large α, the clot is composed of a core of thin, tightly packed fibers, an inner shell of thick fibers, and an outer shell of medium diameter, loosely packed fibers. For small α, the clot has a larger

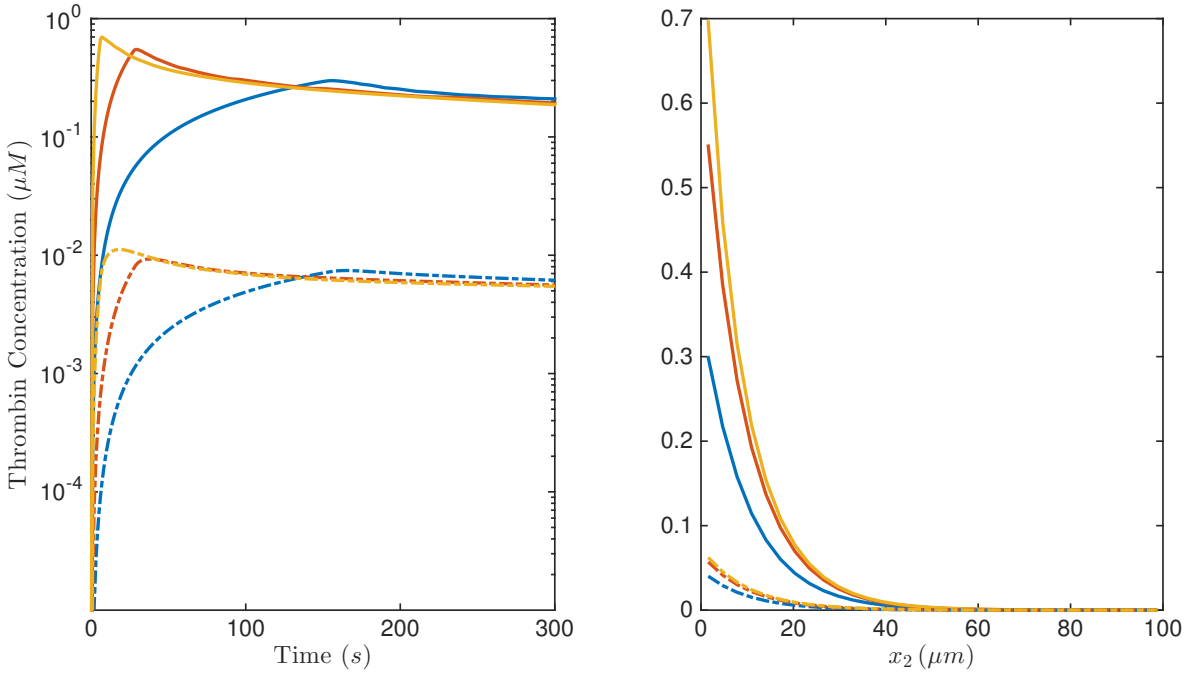

Figure 3.6: Thrombin concentration over time without flow. Left: Maximum and average thrombin concentration over the entire domain as a function of time. Right: Maximum and average thrombin concentration over x_1 and t as a function of x_2. The dashed curves represent average concentrations, the solid curves represent maximum concentrations. The blue, red, and yellow lines represent $\alpha = 10^{-6}$, 10^{-5}, $10^{-4}\,\mu M s^{-1}$ respectively. $k_b = 1\mu M^{-2}s^{-1}$, $f^{up} = 10\mu M$

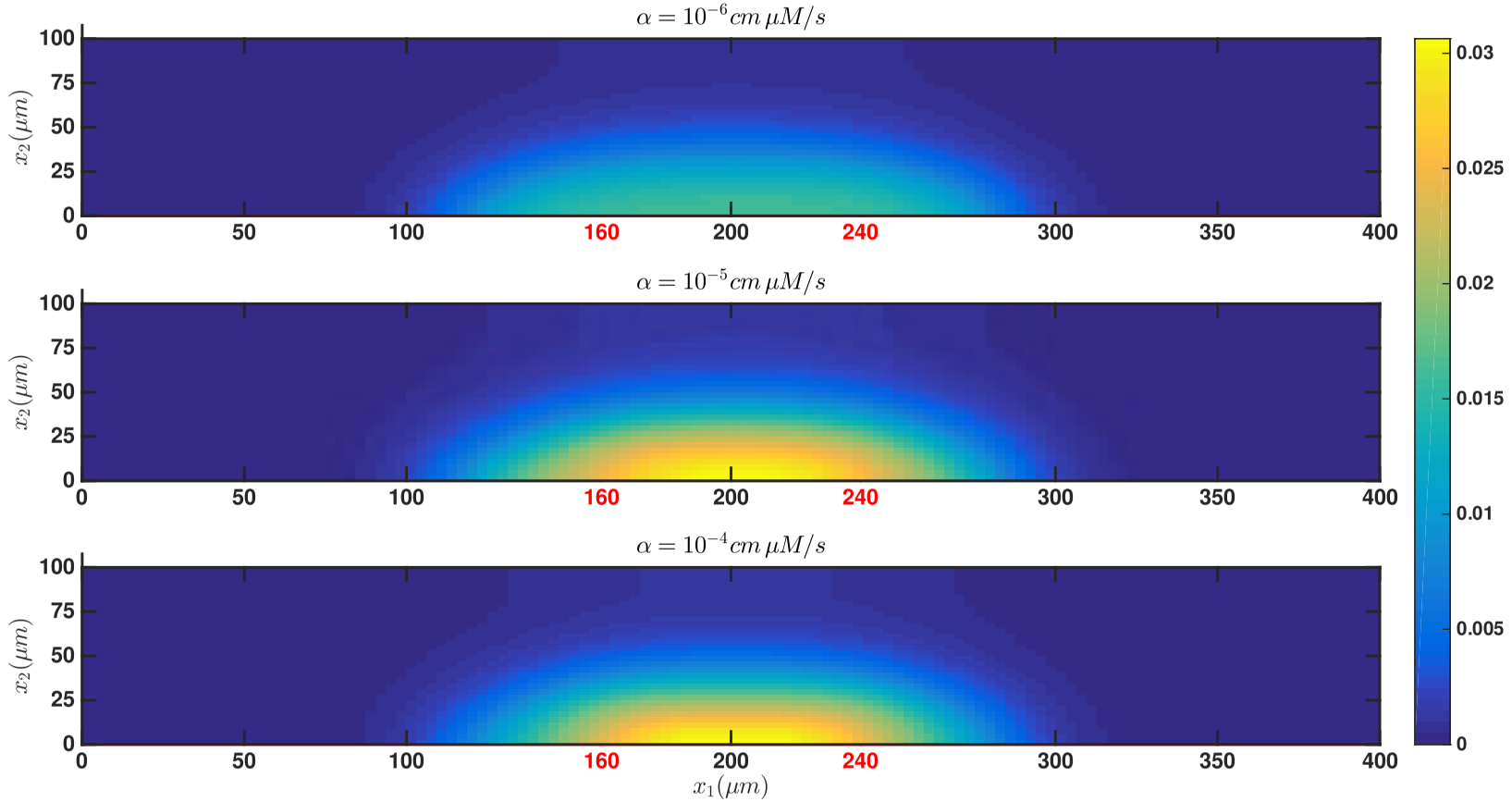

Figure 3.7: Branch point density plotted for different α without flow. This is shown for each spatial location in μM at $t = 300s$. Top: $\alpha = 10^{-6} cm\mu M s^{-1}$. Middle: $\alpha = 10^{-5} cm\mu M s^{-1}$. Bottom: $\alpha = 10^{-4} cm\mu M s^{-1}$. $k_b = 1\mu M^{-2} s^{-1}$, $f^{up} = 10\mu M$.

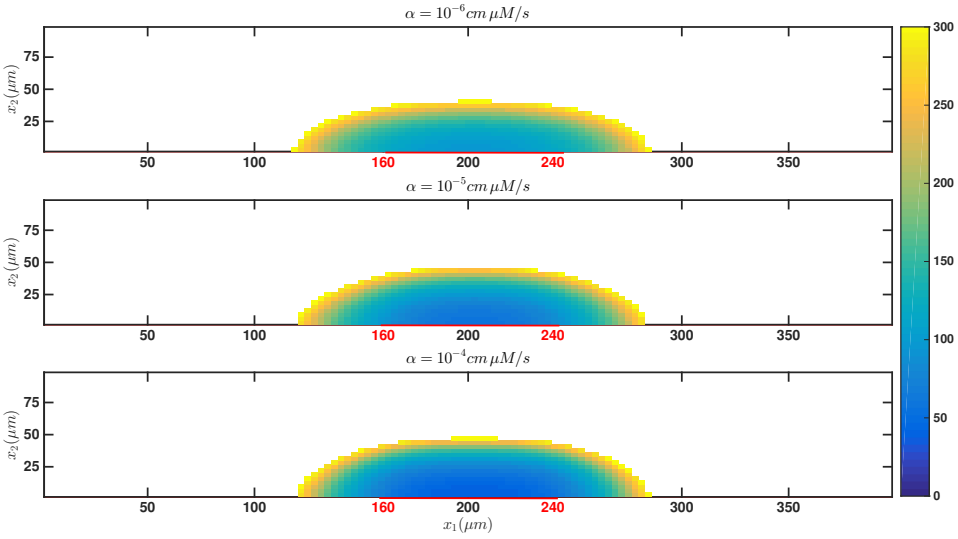

Figure 3.8: Cotting time for different α without flow. This is shown for each spatial location in seconds. Top: $\alpha = 10^{-6} cm\,\mu M s^{-1}$. Middle: $\alpha = 10^{-5} cm\,\mu M s^{-1}$. Bottom: $\alpha = 10^{-4} cm\,\mu M s^{-1}$. $k_b = 1 \mu M^{-2} s^{-1}$, $f^{up} = 10 \mu M$.

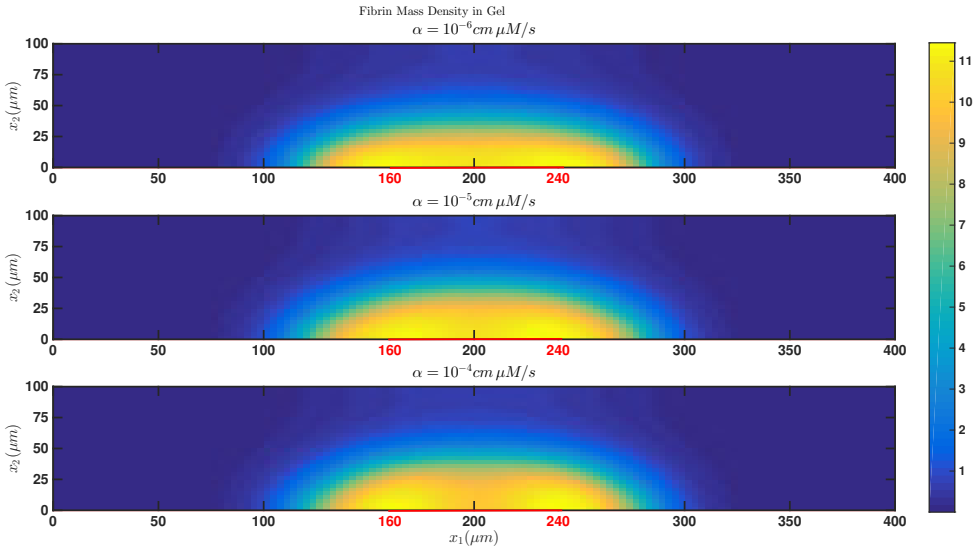

Figure 3.9: Fibrin mass density plotted for different α without flow. This is shown for each spatial location in μM at $t = 300s$. Top: $\alpha = 10^{-6} cm\,\mu M s^{-1}$. Middle $\alpha = 10^{-5} cm\,\mu M s^{-1}$. Bottom: $\alpha = 10^{-4} cm\,\mu M s^{-1}$. $k_b = 1 \mu M^{-2} s^{-1}$. $f_{up} = 10 \mu M$

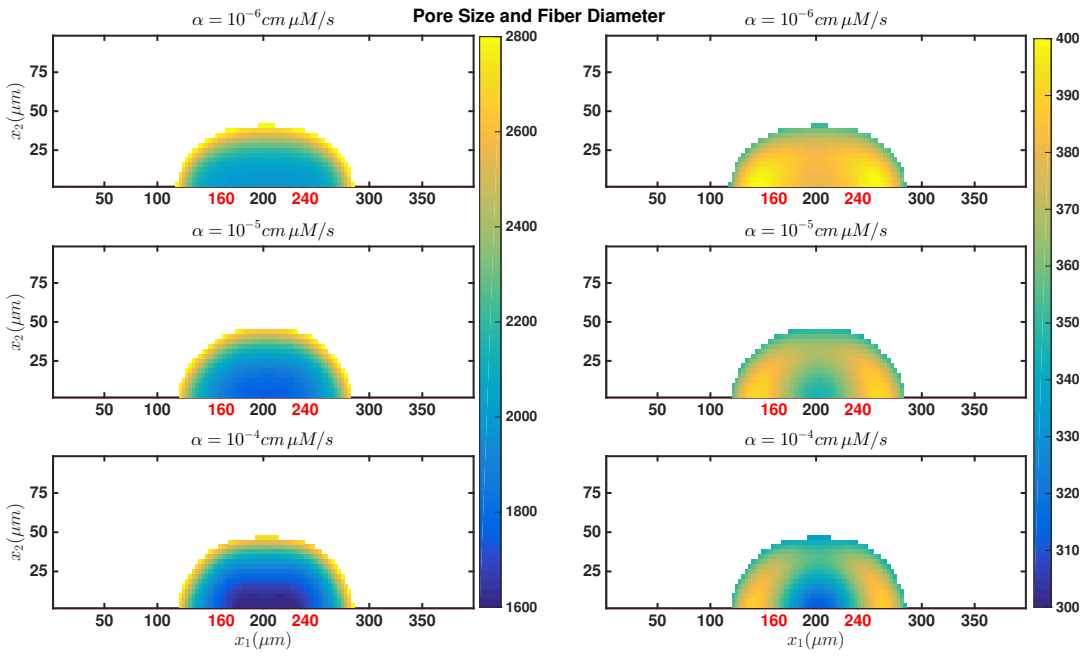

Figure 3.10: Clot structural properties plotted for different α without flow. The pore size (left) and fiber diameter (right) for in nm at $t = 300s$. Top: $\alpha = 10^{-6} cm \mu M s^{-1}$. Middle: $\alpha = 10^{-5} cm\,\mu M s^{-1}$. Bottom: $\alpha = 10^{-4} cm\,\mu M s^{-1}$. $k_b = 1 \mu M^{-2} s^{-1}$. $f_{up} = 10 \mu M$

core of thicker fibers with medium pore sizes and an outer shell that consists of medium diameter fibers and has large pores.

The parameter α affects the rate of thrombin production, but the conversion of prothrombin to thrombin is limited by the rates of diffusion of prothrombin and thrombin. As a result, varying α over several orders of magnitude does not change the spatial extent of the resultant gel. The branch point density and fiber diameter near the wall do change because changes in α affect the rate of fibrin monomer production.

3.1.2 Rate of Branch Point Formation

In the model, there are two rate constants that control fibrin polymerization, k_l and k_b. While there are several estimates for k_l ([15], [39], [24]), there is very little known about the rate, k_b. We explore the effect that varying k_b has on the clot structure.

We find that the value of k_b significantly affects clotting time. This is consistent with results from Ziff's gelation model [42]. The Ziff model consists of a condensation system that occurs between monomers. Each monomer contains f number of binding sites or functional sites for other monomers to bind. As Ziff shows, in order for gelation to occur in a condensation system, there must be more than two functional sites on each monomer. Furthermore, the gel time decreases as the number of functional sites increases. For the model described in Chapter 2, there are two types of reactions, linear extension and branch point formation. The effective number of functional sites for linear extensions is two and for branch point formation is three. This means that it is essential to have branch point formation for gelation to occur. The value of k_b (relative to that of k_l) influences the effective number of functional sites in the fibrin oligomers. For all of the simulations described below, k_l is kept constant. The rate constant, k_b is described in terms of the baseline value k_o, where $k_o = 10\,\mu M^{-2}s^{-2}$.

Table 3.1 shows the time for the first appearance of a gel, as well as the maximum gel width and the maximum gel height at $t = 300\,s$. The first appearance of a gel occurs sooner with increasing k_b. The parameter k_b also has some effect on how clot size changes with t. Smaller k_b values produce more slowly growing clots than higher ones do. It is unclear what the size of the clot will be at steady state. Due to computational limitations, this is not explored.

It is important to note that branch point formation and linear reactions are in competition with each other for monomers. The last column in Table 3.1 shows the mean number of monomers per branch point in the gel at $t = 300\,s$. This ratio shows that linear

Table 3.1: Gel time and clot size for various branching rates. Here $t = 300\,s$. $k_o = 10\,\mu M^{-2}s^{-1}$, $\alpha = 10^{-4}cm\,\mu M s^{-1}$, $f_{up} = 10\mu M$

k_b	First Gel Time	Max Gel Width	Max Gel Height	Monomer/Branch Point
$k_o/10$	$58\,s$	$190\,\mu m$	$42\,\mu m$	674.4
$k_o/5$	$30\,s$	$212\,\mu m$	$45\,\mu m$	421.9
$k_o/2$	$15\,s$	$221\,\mu m$	$48\,\mu m$	210.7
k_o	$10\,s$	$228\,\mu m$	$52\,\mu m$	128.1
$2k_o$	$8\,s$	$228\,\mu m$	$52\,\mu m$	79.3

reactions are favored over branch reactions in the gel but that increasing k_b decreases the number of monomers per branch point.

To better quantify the competition, we look at the rate of branch point formation and linear extension. The overall branch point formation rate is $\frac{k_b}{6}\left(R^3 - (3R_sR_g^2 + R_g^3)\right)$ and the overall extension reaction rate is $\frac{k_l}{2}\left(R^2 - R_g^2\right)$. Figure 3.11 shows that the competition between extension reactions and branch point formation is not significantly affected by k_b over the range of values considered. There is at most a 10% difference between the maximum and average rate of extension reaction for $k_b = k_o/10$ and $k_b = 2k_o$. Of course, the average and maximum overall rates of branch point formation are more significantly affected by k_b. The peak in the overall branching reaction rate corresponds to the higher fibrin source rate near the wall. The subsequent decrease is due to a decrease in the rate of production of monomer from the reaction between fibrinogen and thrombin becoming diffusion limited. Figure 3.12 shows the branch point concentration at $t = 300\,s$. As k_b is increased, the branch point densities increase and also show greater variation across the clot. The mass of fibrin in the gel also changes when the rate of branch point formation changes. However, these changes are limited due to the similarities in the overall rate of linear extension reactions for the different k_b values and the dominance of the linear extension reactions over the branching ones. Figure 3.13 shows the distribution of fibrin mass density in the gel. They are similar and show similar amounts of spatial variably, except for the smallest value, $k_b = k_o/10$. At this rate constant, the fibrin mass in the gel is more uniform.

The combination of branch point and fibrin mass density leads to different pore size and fiber diameter, as shown in Figure 3.14. For the rate constant, $k_b = k_o/2$, the fiber diameter is large and has low variability across the clot. As k_b increases, the clot becomes more uniform and denser with smaller fiber diameters and pores. As k_b decreases, for $k_o/2$

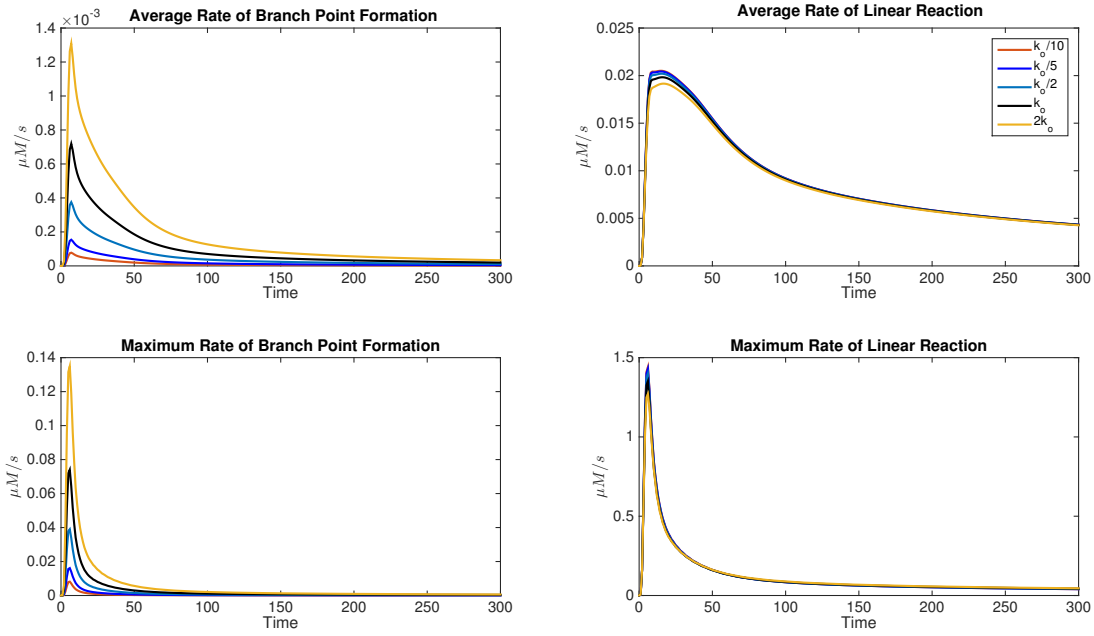

Figure 3.11: Branch and linear reaction rates plot for different k_b without flow. This is shown for $k_b = k_o/10,\ k_o/5,\ k_o/2,\ k_o,\ 2k_o$ with $k_o = 10\,\mu M^{-2}s^{-1}$. $\alpha = 10^{-4}cm\,\mu M s^{-1}$, $f_{up} = 10\mu M$

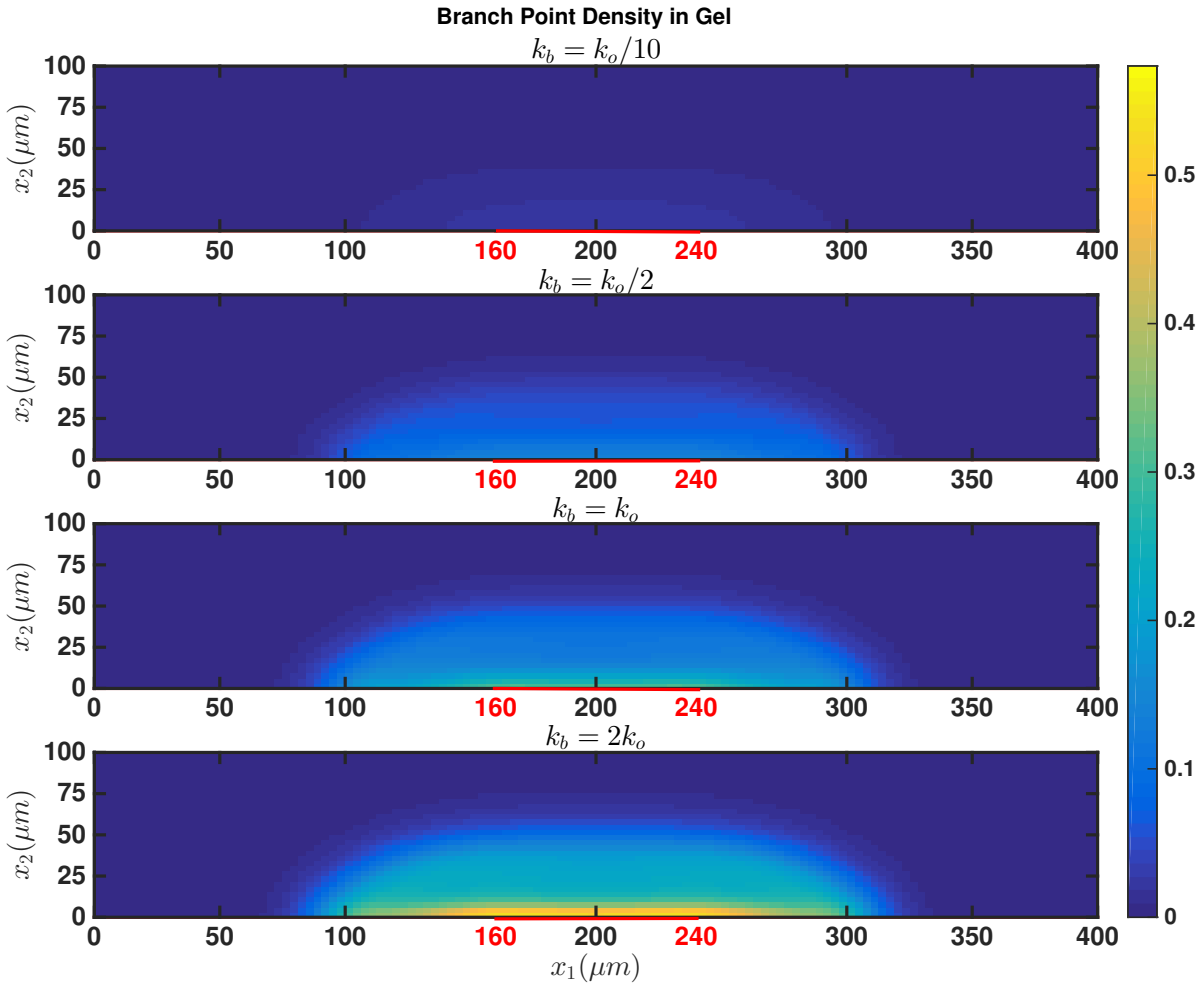

Figure 3.12: Branch point density distribution plotted for different k_b without flow. This is shown for branch point density in gel for four rates of k_b. $k_o = 10\,\mu M^{-2}s^{-1}$, $\alpha = 10^{-4}cm\,\mu M s^{-1}$, $f_{up} = 10\mu M$

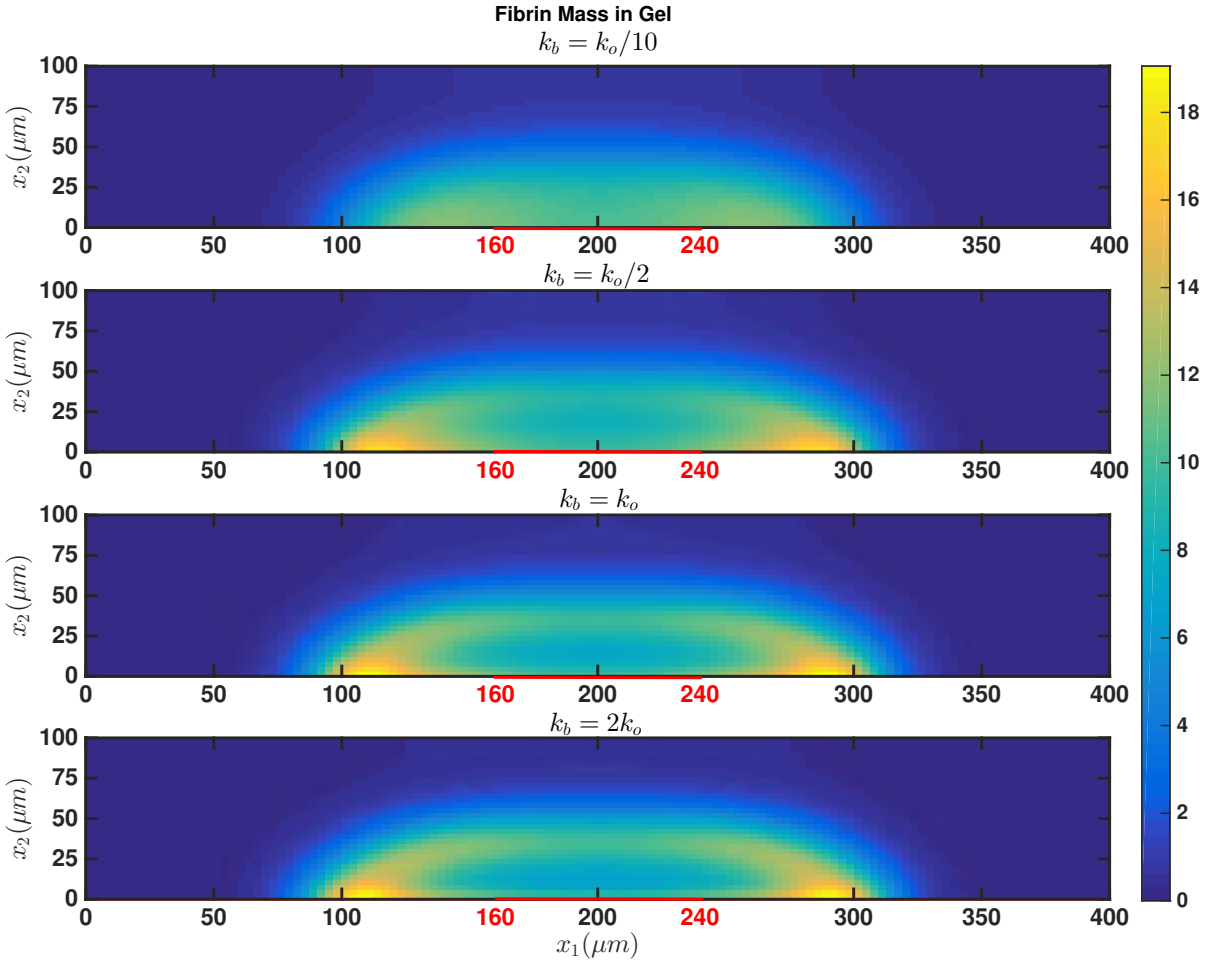

Figure 3.13: Fibrin mass density plotted for different k_b without flow. This is shown for fibrin mass density in gel for four values of k_b. $k_o = 10\,\mu M^{-2}s^{-1}$, $\alpha = 10^{-4}cm\,\mu Ms^{-1}$. $f_{up} = 10\mu M$

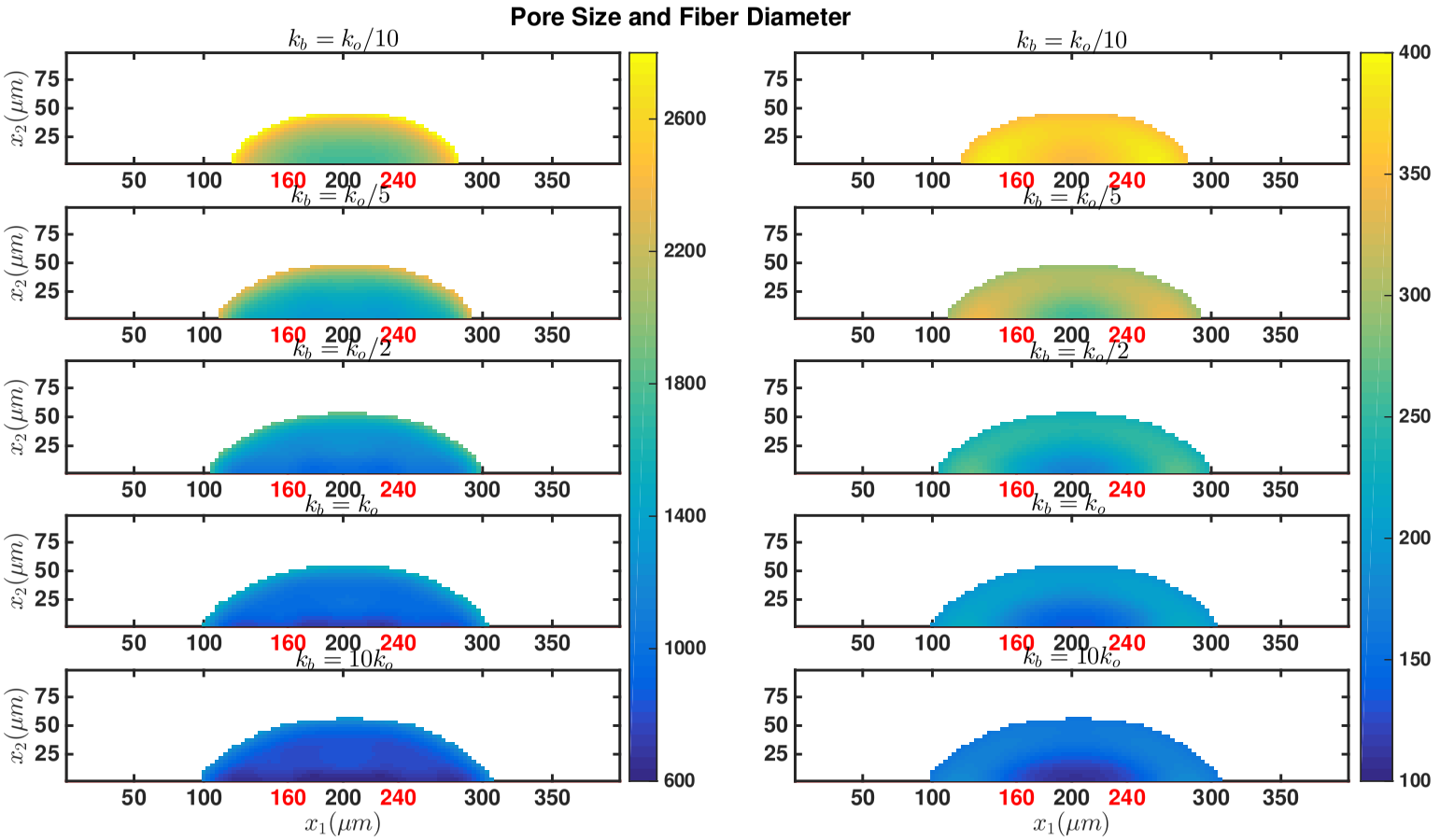

Figure 3.14: Clot structure properties plotted for different k_b without flow. Pore size (left) and fiber diameter (right) in nm for values of k_b. Note that the scales are in (nm). $k_o = 10\,\mu M^{-2}s^{-1}$, $\alpha = 10^{-4}cm\,\mu M s^{-1}$, $f_{up} = 10\mu M$

there is more spatial variation in the pore sizes as well as larger values of the maximum pore size and maximum fiber diameter.

3.1.3 Upstream Fibrinogen Concentration

There are three types of fibrinogen disorders: afibrinogenemia, hypofibrinogenemia, and dysfibrinogenemia. People with dysfibrinogenemia have normal concentrations of fibrinogen but their fibrinogen contains structural abnormalities. People with afibrinogenemia and hypofibrinogenemia have lower than normal fibrinogen concentrations. According to Acharya and Dimichele (2008), afibrinogenemia patients have $< 0.59\,\mu mol/L$ of fibrinogen circulating in the blood. Hypofibrinogenemia patients typically have between $0.59 - 2.4\,\mu mol/L$. Normal fibrinogen concentrations in human blood fall in the range $5.9 - 11.8\,\mu mol/L$. All of these disorders cause clotting issues. Hypofibrinogenemia and dysfibrinogenemia cause prolonged clotting times. Patients with afibrinogenemia are said to not clot. [1]

The model from Chapter 2 can be modified to study afibrinogenemia and hypofibrinogenemia by altering the upstream fibrinogen concentration. We look at fibrinogen concentrations of 0.5, 1, 5, 10, and $50\,\mu mol/L$. Table 3.2 shows the time a gel first appears for each of these cases. For low upstream fibrinogen concentration ($f^{up} = 0.5 - 1 \mu mol/L$), no clot appears by $2000\,s$. It takes more than eight times as long for a fibrin gel to appear for $f^{up} = 5 \mu mol/L$ than for $f^{up} = 10 \mu mol/L$. Increasing the upstream fibrinogen concentration by another factor of five ($f^{up} = 10 \mu mol/L$ to $f^{up} = 50 \mu mol/L$), it is six times faster. Figure 3.15 shows the growth rate of the gel is affected by the fibrinogen concentration. Figure 3.16 shows the branch point density of fibrin gels for various upstream fibrinogen concentrations. With low fibrinogen concentration no gel is able to form. With high upstream fibrinogen concentration, there is a larger branch point density along the lower vessel wall. While the branch point density is higher in larger upstream fibrinogen concentration, the profile shape is consistent with normal upstream fibrinogen concentration. The fibrin mass density shows a similar effect and is shown in Figure 3.17.

Table 3.2: Gel time and clot size various f^{up}. $k_b = 1\,\mu M^{-2} s^{-1}$, $\alpha = 10^{-4} cm\,\mu M s^{-1}$

$f^{up}(\mu mol/L)$	First Gel Time
0.5	–
1	–
5	$480\,s$
10	$58\,s$
50	$10\,s$

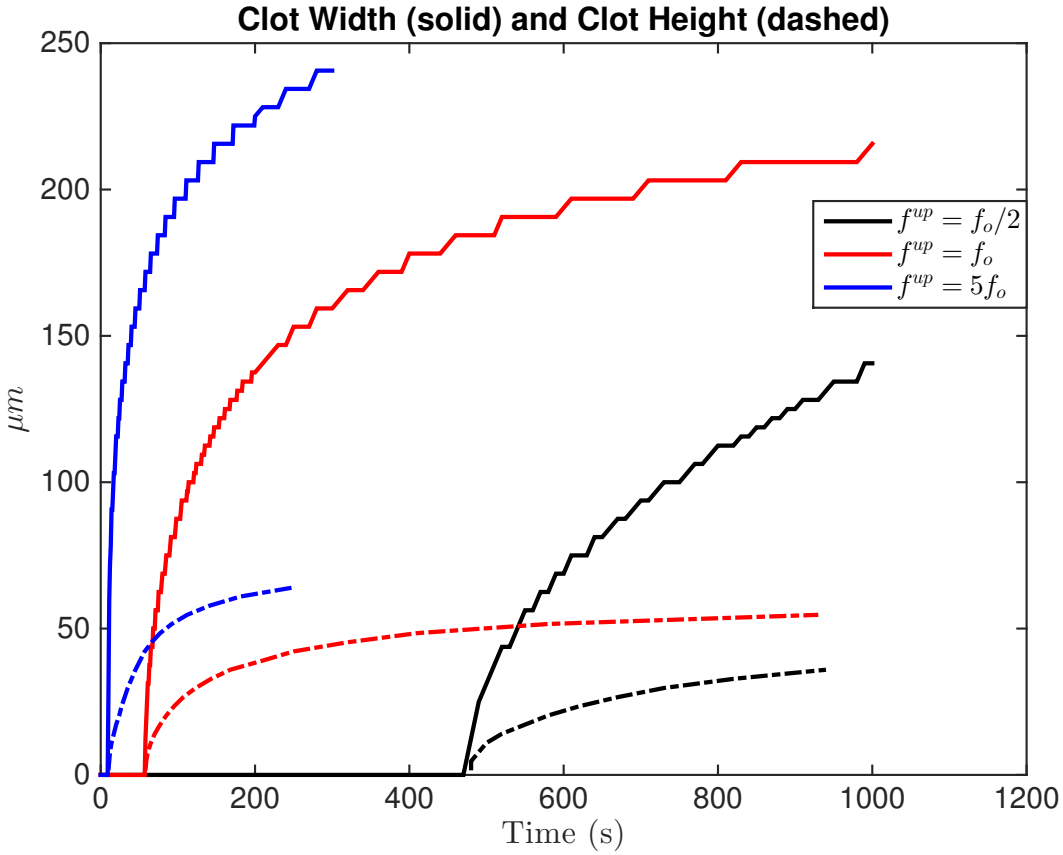

Figure 3.15: The height and width of gels formed with different fibrinogen concentrations: $f^{up} = .5f_o = 5\mu mol/L$ (black), $f^{up} = f_o = 10\mu mol/L$, (red) and for $f^{up} = 5f_o = 50\mu mol/L$, (blue). $k_b = 1\,\mu M^{-2}s^{-1}$, $\alpha = 10^{-4} cm\,\mu M s^{-1}$

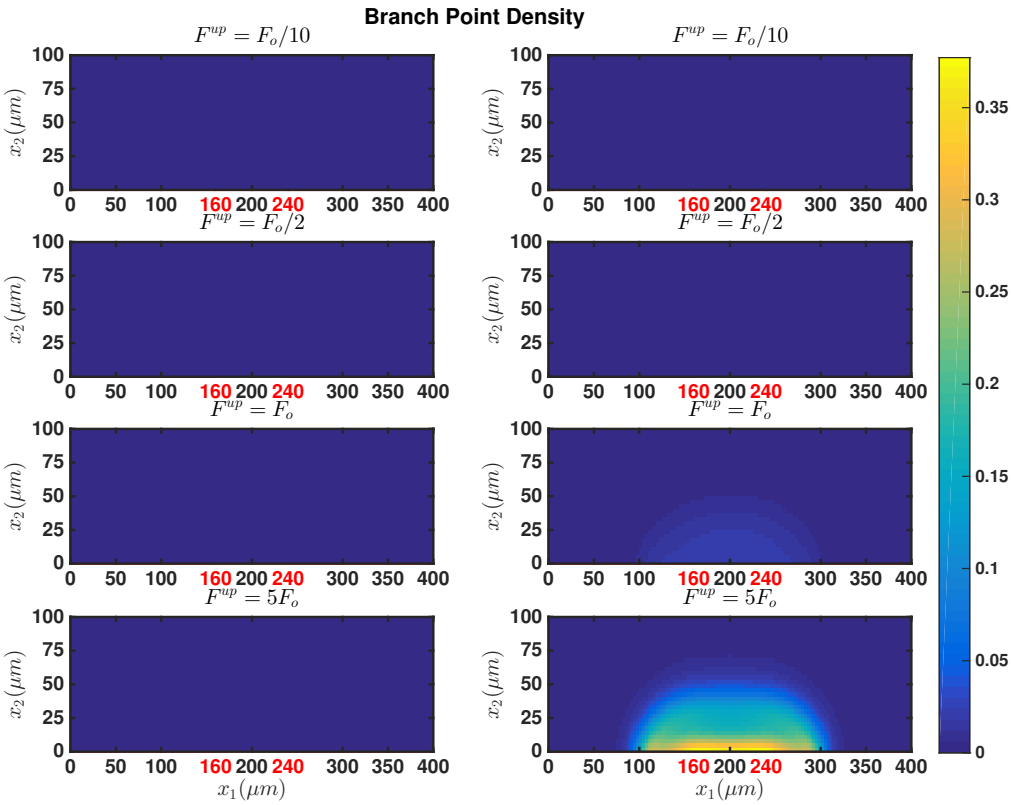

Figure 3.16: Branch point density for various upstream fibrinogen concentrations $f^{up} = f_o/10 = 1\mu mol/L$, $f^{up} = f_o/2 = 5\mu mol/L$, $f^{up} = f_o = 10\mu mol/L$,and for $f^{up} = 5f_o = 50\mu mol/L$. The left side of the graph shows the density for branch point densities in the sol and the right side shows the branch point density in the gel at t = 150 s $k_b = 1\,\mu M^{-2}s^{-1}$, $\alpha = 10^{-4}cm\,\mu M s^{-1}$.

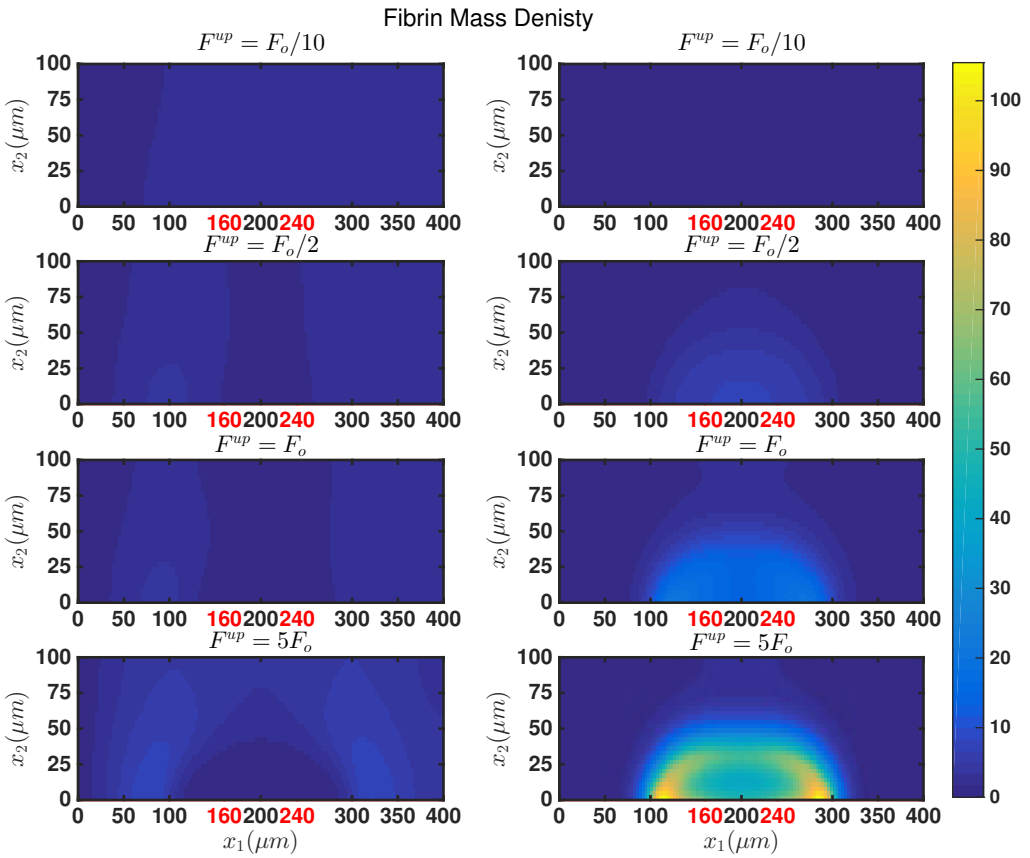

Figure 3.17: Fibrin mass density for various upstream fibrinogen concentrations $f^{up} = f_o/10 = 1\mu mol/L$, $f^{up} = f_o/2 = 5\mu mol/L$, $f^{up} = f_o = 10\mu mol/L$,and for $f^{up} = 5f_o = 50\mu mol/L$. The left side of the graph shows the density for fibrin mass densities in the sol and the right side shows the fibrin mass density in the gel at t = 150 s $k_b = 1\,\mu M^{-2}s^{-1}$, $\alpha = 10^{-4}cm\,\mu M s^{-1}$.

As expected, the larger branch point density and fibrin mass density seen in high upstream fibrinogen concentrations results in fibrin fibers having a smaller diameter (Figure 3.18) and a smaller pore size (Figure 3.19).

3.2 Flow

Next, we explore the model in flow. Fluid flow moves coagulation proteins and oligomers away from the injury site, while suppling fibrinogen and prothrombin. The obvious question is what is the overall effect of the fluid flow on fibrin clot formation?

We begin by prescribing a parabolic flow at the left boundary with a wall shear rate of $10\,s^{-1}$. A low shear rate is representative of shear rates in veins or other smaller blood vessels. We use a domain twice the size as before ($L_{x_1} = 800\,\mu m$ and $L_{x_2} = 200\,\mu m$). Fibrin takes time to form gel from a collection of oligomers. Without flow and for $\alpha = 10^{-6}\mu M\,s^{-1}$ and $k_b = 10\,\mu M^{-2}\,cm\,s^{-1}$, it takes 58 seconds for fibrinogen to become a fibrin gel. At a wall shear rate of $10\,s^{-1}$, an oligomer $1.5\,\mu m$ from the wall would travel 900 μm in $58\,s$ (assuming a shear flow near the wall). This suggests gelation cannot be initiated over an injury zone by the action of thrombin produced there.

The model also produces this result. Fibrin monomer is produced only in a thin strip. One part of the strip is over the injury zone near where thrombin is produced. Thrombin and fibrinogen advect downstream with the fluid and interact to produce fibrin monomer away from the injury zone. The fibrin continues to polymerize while moving downstream and a small amount of gel is produced along the bottom wall first at a location around $x_1 = 725\,\mu m$. The gel then slows the fluid velocity around it which allows additional gel to form on the upstream side of the clot. Figure 3.20 shows the branch point density in the gel and the fibrin source rate at $t = 150s$. Note in these simulations we set $k_b = k_l = 0$ near the right wall to prevent nonphysical accumulations along the bottom corner. The bottom plot shows the shear rate. As the gel forms, the fluid slows in the presence of the gel (due to the Brinkman term in the Navier Stokes equations).

While it is possible for the clot to grow upstream, it is not physiological for a fibrin clot to be initiated downstream from an injury. This is consistent with experimental data from the Neeves Lab [30] where they find fibrin clots do not form on a flat surface. We look at physiological conditions to see what is different between our model and the situation in the body. One difference is, in physiological conditions, platelets bind prior to fibrin clot formation. A collection of platelets could hinder the flow over the injury zone and initiate the conversion of prothrombin to thrombin on platelet surfaces away from the wall.

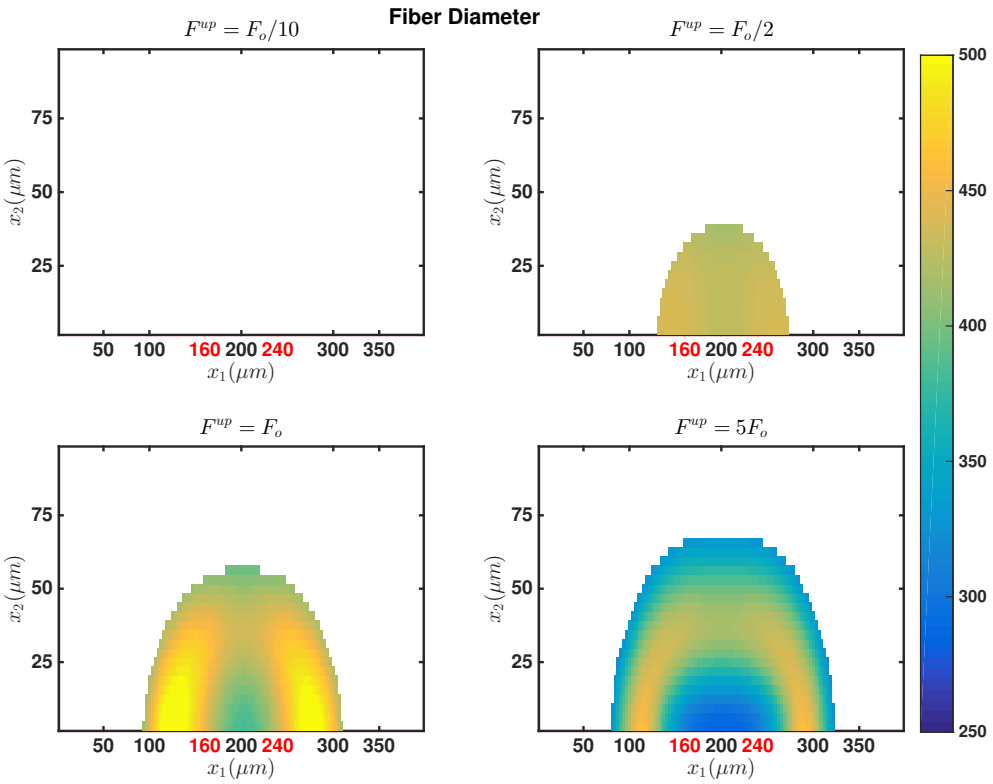

Figure 3.18: Fiber diameter for various upstream fibrinogen concentrations. Here $f^{up} = f_o/10 = 1\mu mol/L$, $f^{up} = f_o/2 = 5\mu mol/L$, $f^{up} = f_o = 10\mu mol/L$,and for $f^{up} = 5f_o = 50\mu mol/L$ at t =150 s $k_b = 1\,\mu M^{-2}s^{-1}$, $\alpha = 10^{-4} cm\,\mu M s^{-1}$.

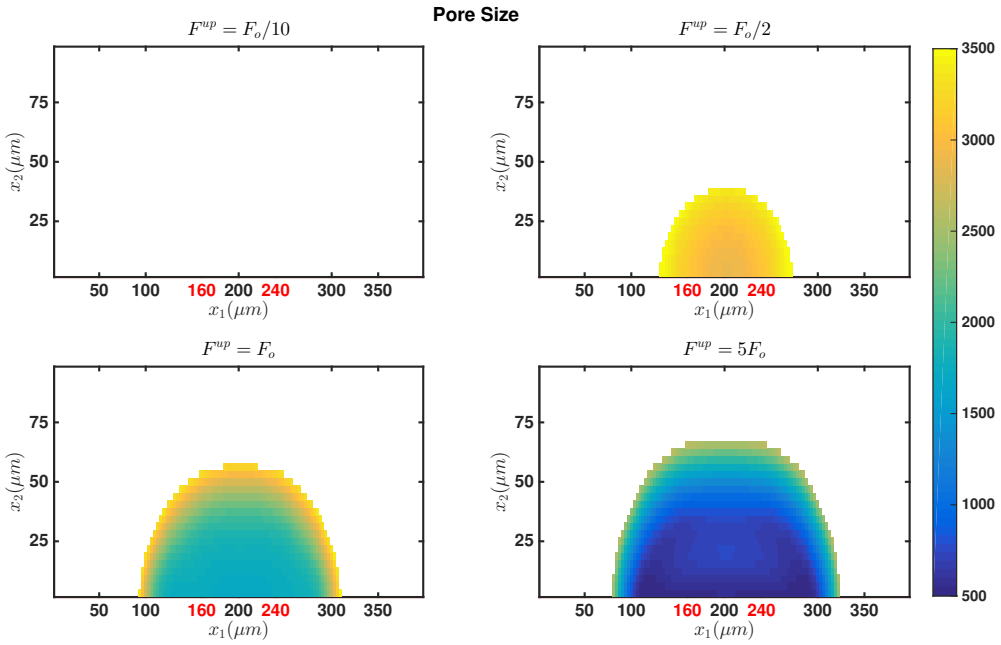

Figure 3.19: Pore size for various upstream fibrinogen concentrations. Here $f^{up} = f_o/10 = 1\mu mol/L$, $f^{up} = f_o/2 = 5\mu mol/L$, $f^{up} = f_o = 10\mu mol/L$,and for $f^{up} = 5f_o = 50\mu mol/L$ at t =150 s $k_b = 1\,\mu M^{-2}s^{-1}$, $\alpha = 10^{-4} cm\,\mu M s^{-1}$.

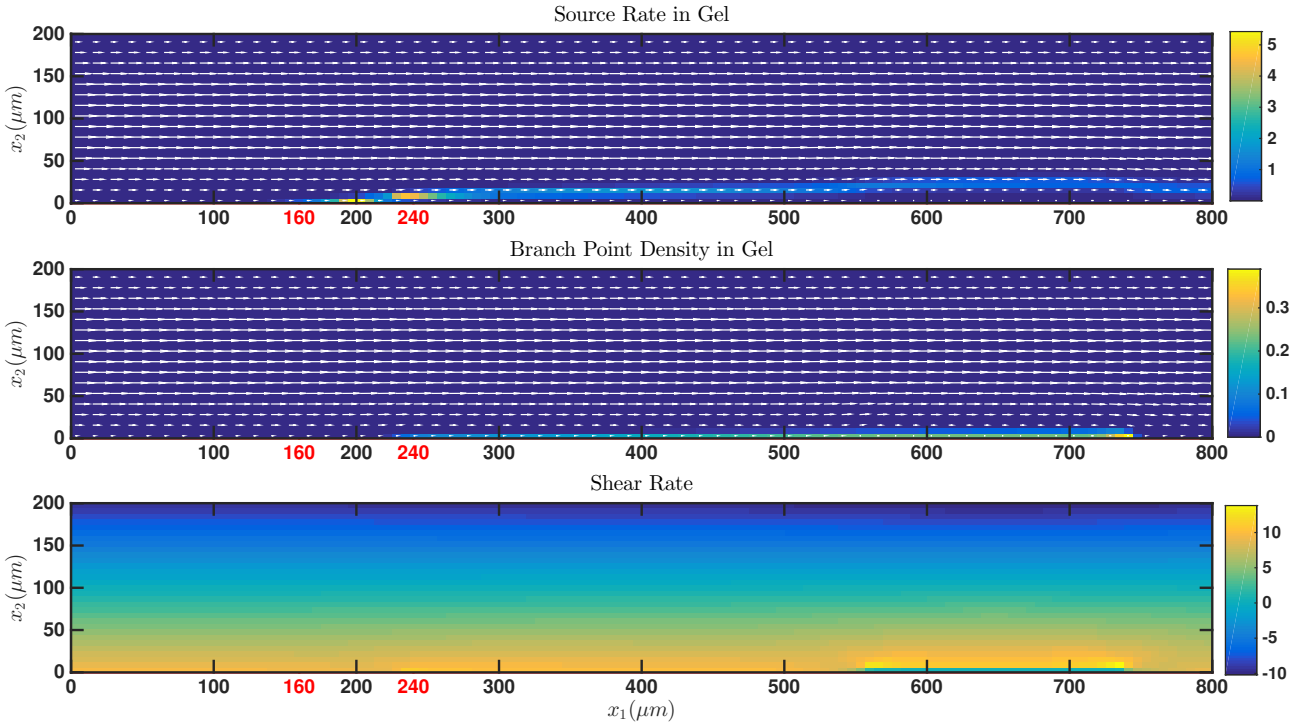

Figure 3.20: Source rate, branch point density, and shear rate for unhindered flow. Top: Source rate distribution $\mu M s^{-1}$. Middle: Distribution of branch point density in the gel in μM. Bottom: Shear rate of the fluid in s^{-1} at $t = 150\,s$, given $\alpha = 10^{-6}\mu M\,s^{-1}$, $k_b = 10\,\mu M^{-2}\,cm\,s^{-1}$, and $f_{up} = 10\mu M$.

First, we explore fibrin formation in hindered flow. In Chapter 4, we look at prothrombin conversion away from the wall.

3.3 Hindered Flow

In order to simulate a group of platelets or any other cells bound upstream from the injury zone, we include a "bump" or an area with a large Brinkman coefficient (α_1) in the domain. We do this for an area about $9\,\mu m$ tall and $20\,\mu m$ wide near the upstream end of the injury site. This addition, shown in Figure 3.21, diverts fluid around the bump and slows fluid flow in and downstream of it. As we show, this allows fibrin gelation to occur over the injury site.

For the following simulation, we use the original domain ($L_{x_1} = 400\,\mu m$ and $L_{x_2} = 100\,\mu m$) and a shear rate of $100\,s^{-1}$. As in the previous simulation, we set $k_b = k_l = 0$ near the right boundary. Figure 3.22 shows thrombin concentration, fibrinogen concentration, and fibrin source rate. The yellow curve on each plot shows the 25% maximum contour for the Brinkman coefficient and the red numbers still delimit the injury zone. The bump allows thrombin and fibrinogen to diffuse upstream and stay around the injury site for a longer period of time. There is depletion of fibrinogen in the areas with small velocities but overall the constant supplying of fibrinogen and prothrombin around the injury zone leads to an increase in fibrin monomer production compared to the no flow cases. Figure 3.23 shows the branch point density and fibrin mass in the gel. Notice that the highest concentration for both occurs on the downstream side of the gel where the source is highest. Also, notice the concentration of fibrin mass and the branch point density in the gel are significantly higher than in the no flow case (shown in Figure 3.12 and 3.13). When the simulation runs longer, a gel grows along the bottom wall but does not grow much taller than the bump. Figure 3.24 shows that the gel has a small variation in fiber diameter with a wide range of pore sizes. The upstream edge of the gel has large pores while the downstream side of the clot has small pores. Notice, that gels formed in flow do not have the same core, inner shell, outer shell structure that was seen in the no flow case. Fiber diameters are much more uniform. There is a small outer region where the fiber diameters are small and the pores are very large. As in the no flow case, the gel begins at the wall and grows outward into the lumen and along the walls.

For the remainder of this chapter, we use the following parameter values unless otherwise noted: $\gamma = 10\,s^{-1}$, $\alpha = 10^{-5}\,cm\,\mu M/s$, $k_b = 1\,\mu M^{-2}s^{-1}$, and $f^{up} = 10\,\mu M$.

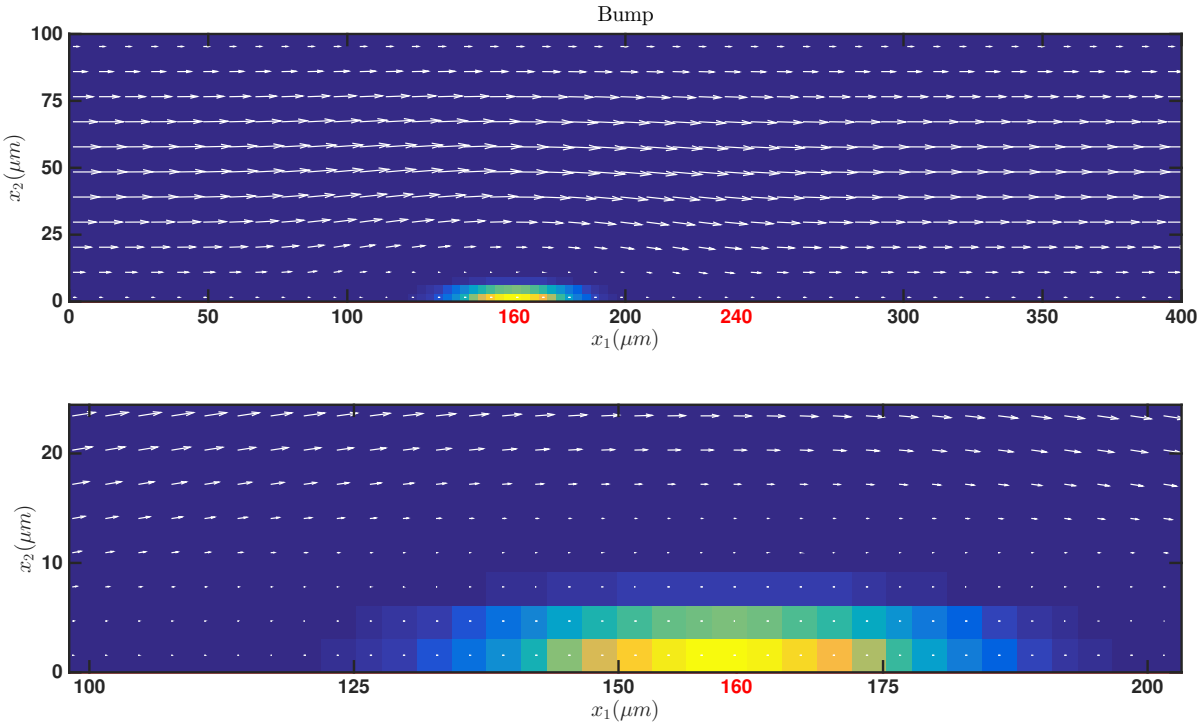

Figure 3.21: Brinkman coefficient distribution for hindered flow. The top plot shows the value of α_1, the Brinkman coefficient. The value α_1 is large in the area upstream from the injury zone to slow down the flow. The fluid velocity vectors are also shown on the plot. The bottom plot is zoomed in on the bump.

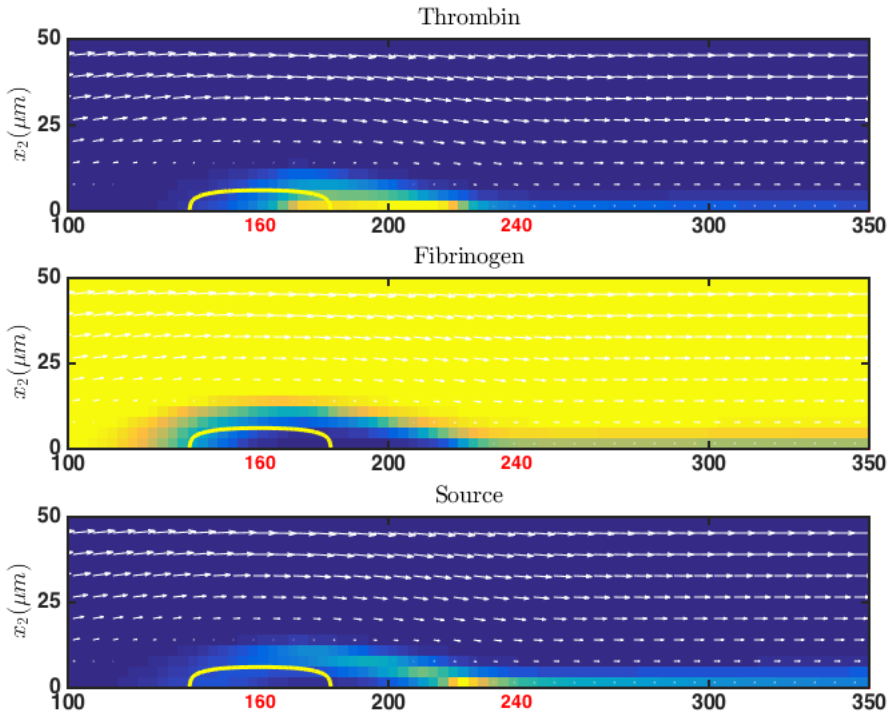

Figure 3.22: Coagulation proteins and source rate distributions in flow. Top: Thrombin concentration in μM,. Middle: Fibrinogen concentration in μM. Bottom: Fibrin source rate for a gel made at $\alpha = 10^{-5}\, cm\, \mu M/s$, $k_b = 1\, \mu M^{-2} s^{-1}$,$f^{up} = 10\, \mu M$, and $\gamma = 100$ at $t = 130\, s$

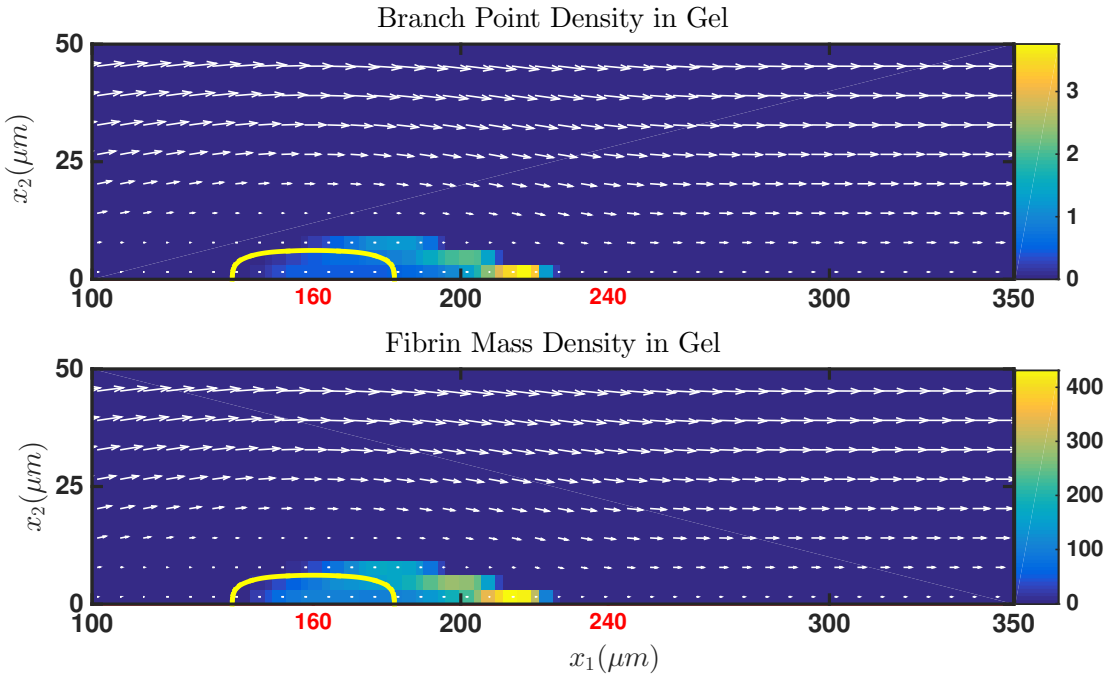

Figure 3.23: Branch point and fibrin mass density distributions in flow. Top: Branch point density in gel μM. Bottom: Fibrin mass density in gel in μM for a gel made at $\alpha = 10^{-5}\, cm\, \mu M/s$, $k_b = 1\, \mu M^{-2} s^{-1}$,$f^{up} = 10\, \mu M$, and $\gamma = 100$ at $t = 130\, s$

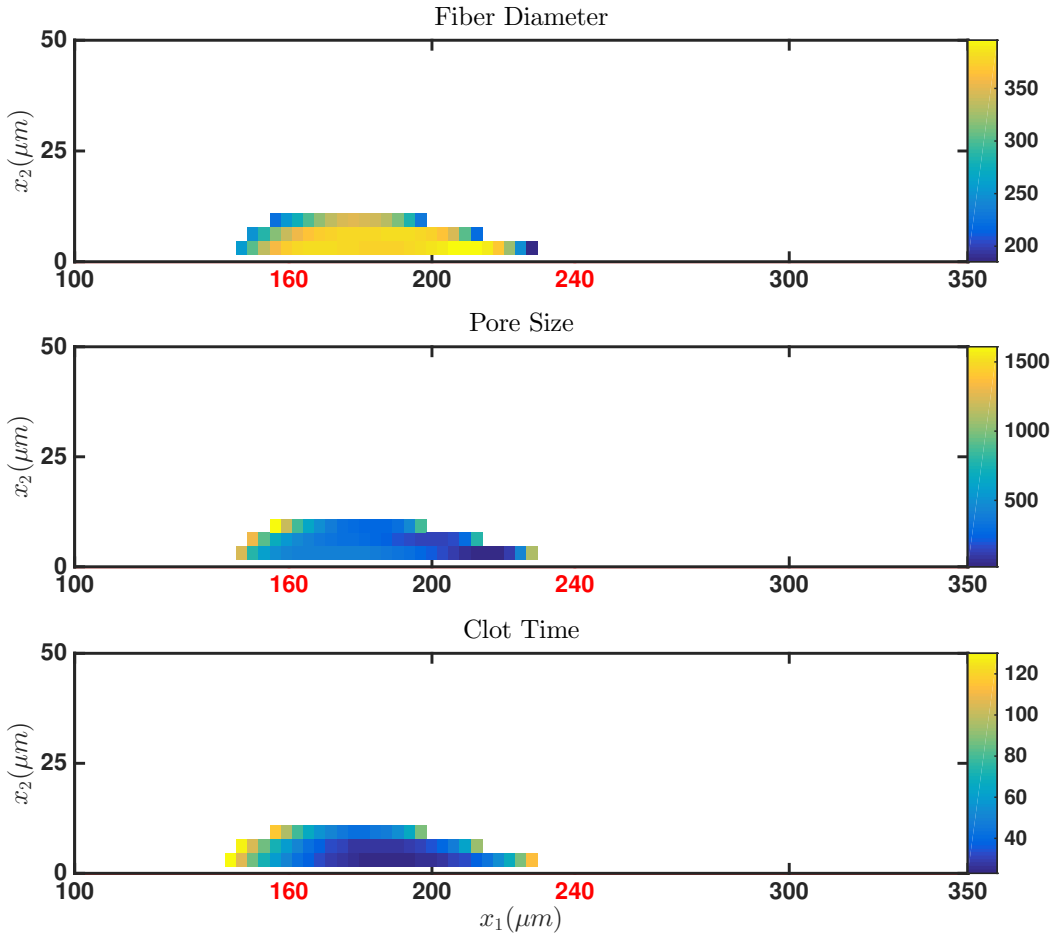

Figure 3.24: Clot structural properties in flow. Top: Fiber diameter (nm). Middle: Pore size (nm). Bottom: Clot time(s) for a gel made at $\alpha = 10^{-5}\, cm\, \mu M/s$, $k_b = 1\, \mu M^{-2} s^{-1}$,$f^{up} = 10\, \mu M$, and $\gamma = 100$ at $t = 130\, s$.

3.3.1 Shear Rate

Next, we explore how the wall shear rate affects fibrin gelation. To begin with, the shear rate affects the profile of the fibrin monomer source. Figure 3.25 shows the source rate for four different shear rates at $t = 115s$. For small shear rates ($1\,s^{-1}$ and $10\,s^{-1}$), the highest source rate occurs away from the wall while for high shear rates, the highest source rates occur at the wall and the source rates are generally higher for larger sheer rates for the range considered. The bump upstream from the injury zone slows the flow and lowers the Péclet number, creating a region in which transport is diffusion domination even for the highest shear rate considered. For low shear rates, this region extends to the end of the injury zone and allows proteins to diffuse effectively over a larger area. For high shear rates, this region ends around 200 μm (where the highest source rate occurs). Inside of these regions, fibrinogen is converted to fibrin faster than diffusion can replenish it and so fibrinogen becomes depleted. Figure 3.25 also shows the fibrin mass density in the gel. The low, diffused source rate created in the low shear environment leads to gels that spread downstream and have low branch point and fibrin mass densities.

For high shear rates, the fibrin is dense and is contained mostly within the region where the Péclet number is low. After an initial transient, the source rate distribution remains qualitatively the same as time advances and fibrin continues to accumulate on the downstream edge of the clot. The continued growth of the fibrin density at this location brings up issues for the fibrin volume fraction. As described so far, the model does not limit accumulation of fibrin mass. Here, the high shear rates case exhibits volume fraction near 20%. In Chapter 5, we present a model with more realistic dynamics that can restrict the gel volume fraction due to hindered transport in the presence of the gel.

Figure 3.26 shows the pore size and fiber diameter of gels that result for the different shear rates. Clots formed at low shear rates have larger pores than those formed at higher shear rates. The fiber diameters vary, with the thickest fibers occurring just inside the upstream edge of the clots. The high shear environment creates dense gels that are located in the diffusion dominated regions. These gels have a core with small pores and nearly uniform fiber diameters. Notice that with high shear, the fibrin clots do not completely cover the injury zone. To do so, a larger region of reduced flow is needed. This is not a surprising result. Physiologically, clots formed at higher shear rates have less fibrin than clots formed at lower shear rates.

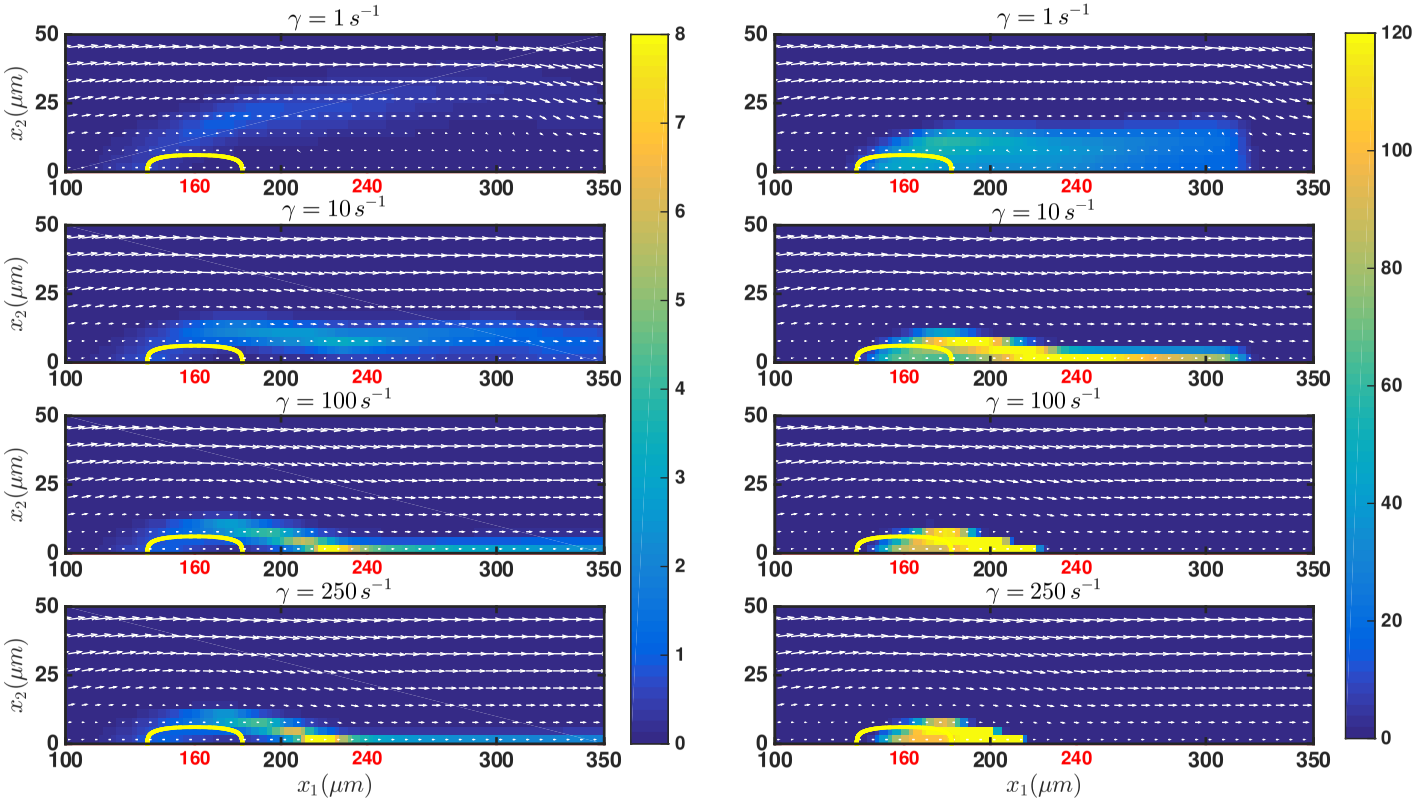

Figure 3.25: Source rate and fibrin mass density distributions plotted for different γ in flow. Left: Fibrin source rates. Right: Fibrin mass density in the gel. Top to Bottom: $\gamma = 1\,s^{-1}$, $\gamma = 10\,s^{-1}$, $\gamma = 100\,s^{-1}$, $\gamma = 250\,s^{-1}$. The yellow curve represents the contour of the Brinkman coefficient. t=115 s for various wall shear rates. $\alpha = 10^{-5}\,cm\,\mu M/s$, $k_b = 1\,\mu M^{-2}s^{-1}$, and $f^{up} = 10\,\mu M$.

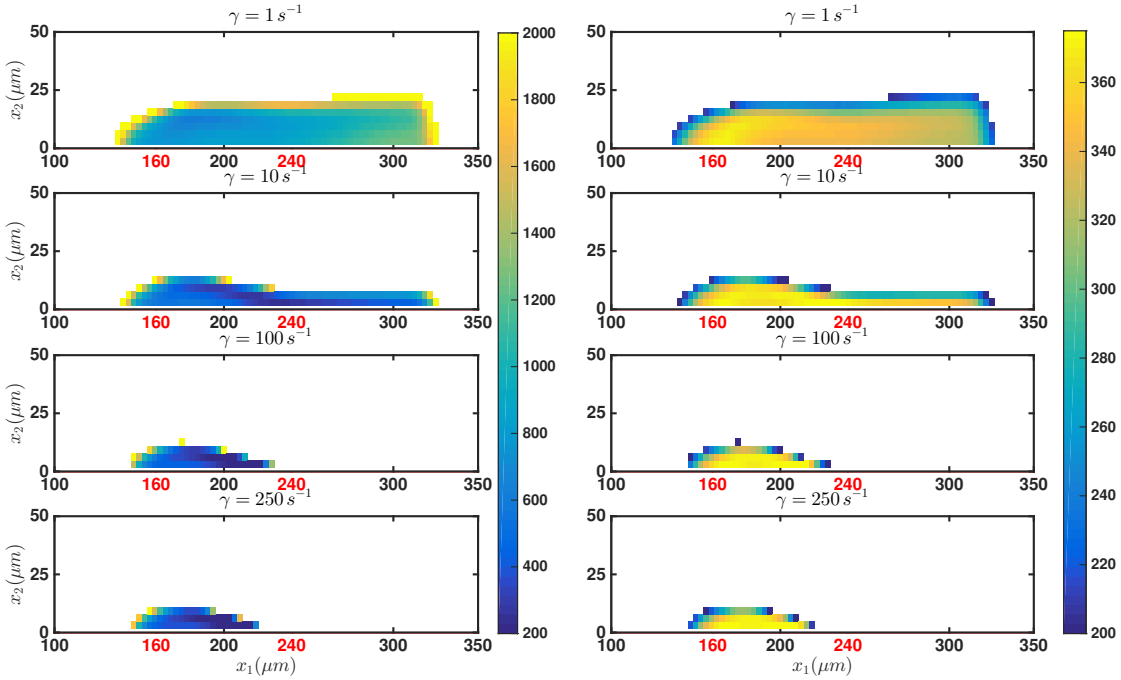

Figure 3.26: Clot structural properties plotted for different γ in flow. Left: Pore size (nm). Right: Fiber diameter (nm). Top to Bottom: $\gamma = 1\,s^{-1}$, $\gamma = 10\,s^{-1}$, $\gamma = 100\,s^{-1}$, $\gamma = 250\,s^{-1}$. At $t = 115\,s$. $\alpha = 10^{-5}\,cm\,\mu M/s$, $k_b = 1\,\mu M^{-2}s^{-1}$, and $f^{up} = 10\,\mu M$.

3.3.2 Thrombin Production Rate

When the fluid velocity is zero, the conversion of prothrombin to thrombin is limited by the diffusivity of prothrombin. Here, we explore how thrombin production is affected by the fluid velocity and the continual supply of prothrombin from upstream. Note that the bump creates a region in which the fluid velocity is sufficiently slow that diffusion is the essential transport process.

When the simulation starts, $z^{up} = 1$ and the flux of thrombin from the injury is approximently α. For large α, prothrombin is depleted quickly from the region just above the injury and the flux rate becomes limited by the rate at which prothrombin diffuses to wall from outside the depleted area. Unlike in the zero fluid velocity case with flow, prothrombin advects with the fluid, and the distance that prothrombin must diffuse to the injury zone is limited. For medium values of α, the depletion of prothrombin takes longer; however, once depleted, prothrombin exhibits the same behavior and has the same concentration profile as for the large α case. For small values of α, it takes even longer for prothrombin to become depleted; however, again it eventually yields the same source rate distribution as for large values of α. The source rate distributions for three values of α are shown in Figure 3.27. Early on, each value of α has a distinct source rate distribution. By $t = 143\,s$ the source rate distributions are similar for the two higher values of α. By $t = 285\,s$, the source rate distributions are even more similar for all three values of α, but the highest source rate in the low α case is found in a more restrictive region. This indicates that for this α, production of thrombin is both transport and reaction limited.

Because the source rates become similar for all values of α, they yield similar branch point density and fibrin mass density distributions. The pore size and fiber diameter for all three α's are shown in Figure 3.28. A smaller value of α yields a larger area with thicker fibers. This is consistent with experimental results that clots made with more thrombin have smaller fibers than clots formed with less thrombin.

3.3.3 Upstream Fibrinogen Concentration

Similar to the no flow case, if the upstream fibrinogen concentration is too low, no gel forms. Figure 3.29 shows the size of the gel for two upstream fibrinogen concentrations, $f^{up} = f_o = 10\mu M$ and $f^{up} = f_o/2 = 5\mu M$. For the low fibrinogen concentrations it takes more than twice as long for the gel to first appear. Unlike the no flow case, the continual supply of fibrinogen allows the gel to grow to the size of one formed with the normal fibrinogen concentration, but over a longer period of time. Figure 3.29 also shows that the

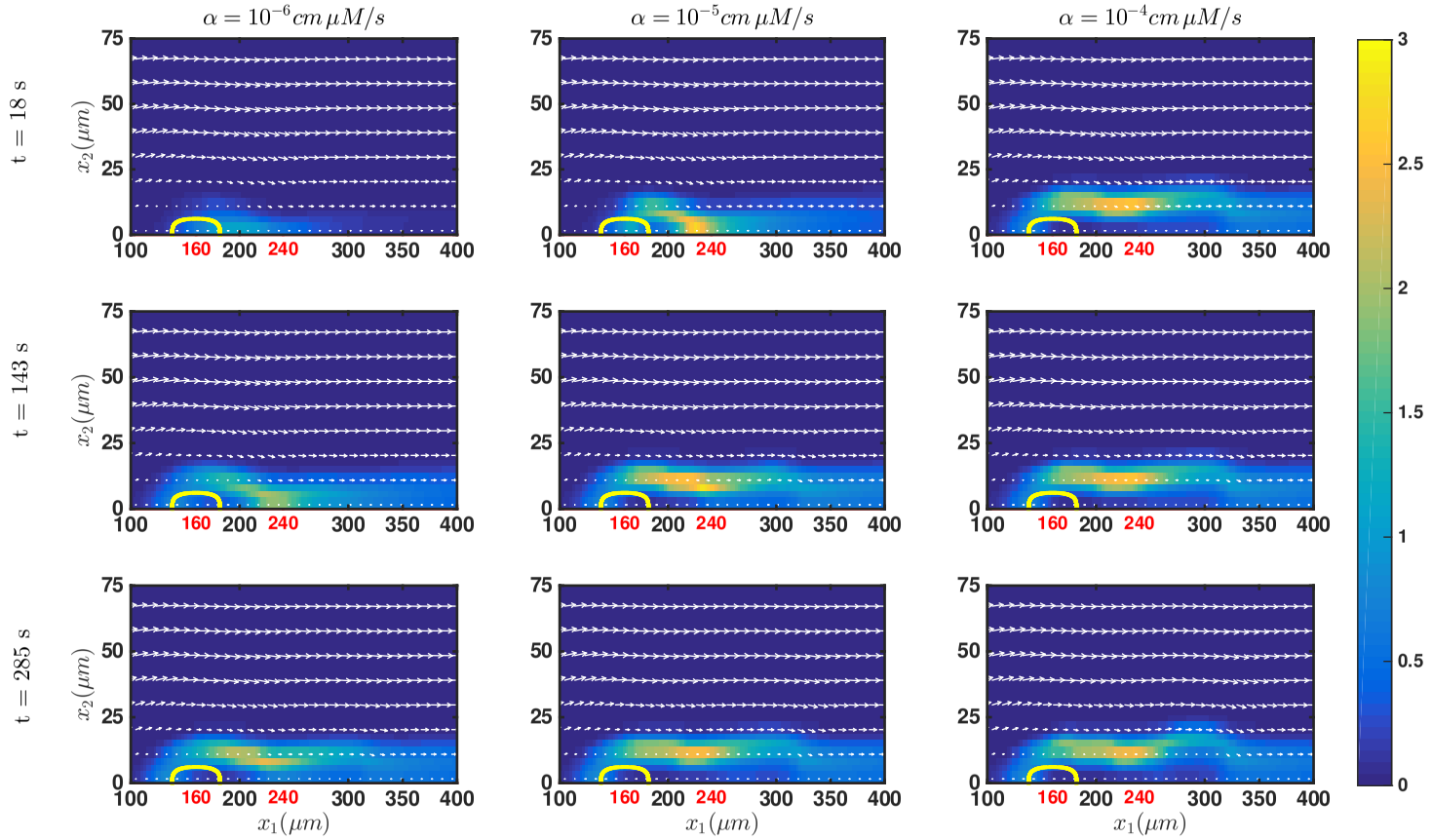

Figure 3.27: Source rate plotted for different α in flow. The source rate in $\mu M/s$ for three values of α at $t = 18\,s$ (top row), $t = 143\,s$ (center row), and $t = 285\,s$ (bottom row). $\gamma = 10 s^{-1}$, $k_b = 1\,\mu M^{-2} s^{-1}$, and $f^{up} = 10\,\mu M$.

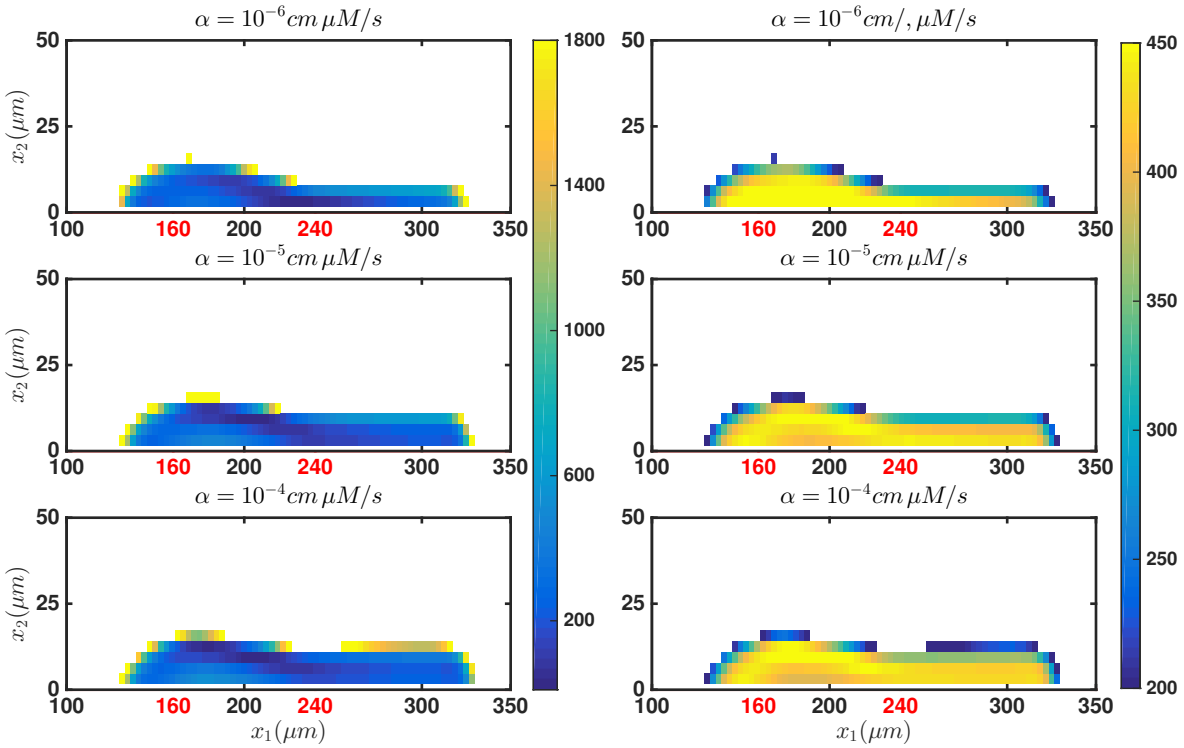

Figure 3.28: Clot structural properties plotted for different α in flow. Left: Pore size in (nm). Right: Fiber diameter in (nm). Top to Bottom: $\alpha = 10^{-6}\, cm\mu M/s$,$\alpha = 10^{-5}\, cm\mu M/s$, $\alpha = 10^{-4}\, cm\mu M/s$. At $t = 285\, s$.

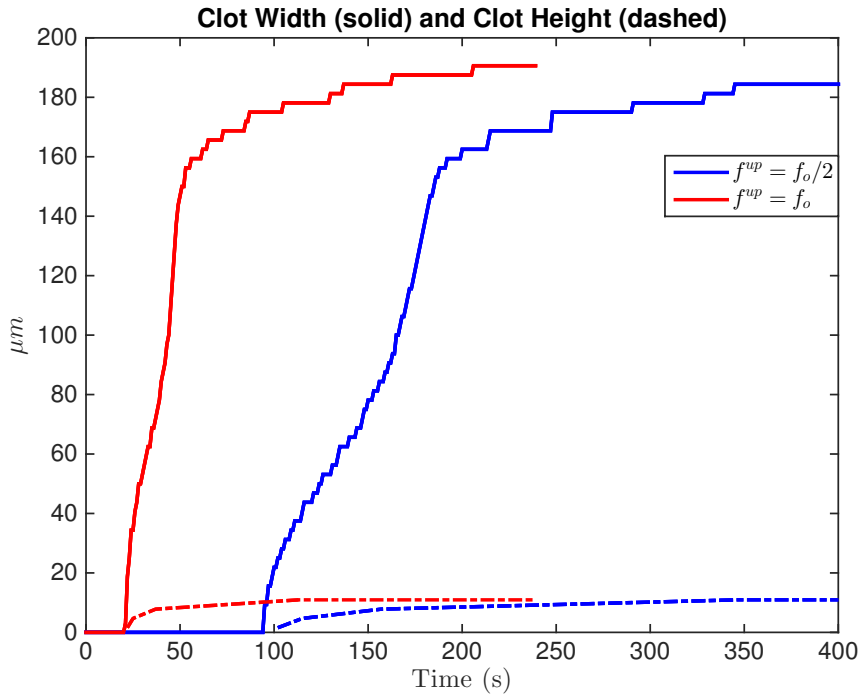

Figure 3.29: Clot structural properties plotted for different f^{up} in flow. The clot dimensions for $f^{up} = 10\mu M$ (red) and $f^{up} = 5\mu M$ (blue). $\gamma = 10\, s^{-1}$, $\alpha = 10^{-5}\, cm\, \mu M/s$, and $k_b = 1\, \mu M^{-2} s^{-1}$.

gel height plateaus around the same value for both fibrinogen concentrations. The fibers continue to thicken after the clot has plateaued. While the resulting clots have similar spatial extents, the fibers in them have different diameters. Figure 3.30 shows the pore size and fiber diameter for three gels. The first is a gel created with normal fibrinogen concentration at $t = 187\,s$, the second is a gel formed with low fibrinogen concentrations at $t = 187\,s$, and the third is a gel formed in with low fibrinogen concentrations at $t = 415\,s$. With higher fibrinogen concentration, gels have larger regions where the pores are small.

3.3.4 Rate of Branch Point Formation

The rate constant for branch point formation, k_b, affects not only the concentration of branches but also the gel growth rate. As a reminder to the reader, the overall branch point formation rate is $\frac{k_b}{6}\left(R^3 - (3R_sR_g^2 + R_g^3)\right)$ and the overall extension reaction rate is $\frac{k_l}{2}\left(R^2 - R_g^2\right)$. Unlike the situation for fibrin gels formed without flow (Figure 3.11), increasing k_b in the case of flow causes an increase in branch formation and a significant decrease in the rate of linear reactions. Figure 3.31 shows that for all k_b considered, the rate of linear reactions is higher than the rate of branch point formation. Increasing k_b by a factor of 10 from $k_o/10$ to k_o causes a 42% reduction in the maximum rate of linear reactions for all time and increases the rate of branch point formation by a factor of 5. With flow, it appears that the two types of reactions compete strongly with one another. This is different from what is seen in simulation without flow, where changes in k_b did not greatly change the rate of linear reactions. This difference could be due to the changes in the source rate distribution. With flow, the source rate is substantially higher in a small region on the downstream end of the injury zone. Without flow, the source rate is positive over a larger area but its maximum is much smaller than that in flow.

Table 3.3 shows the first time that a gel appears anywhere, the spatial average number of monomers per branch point, and the spatial average gel branch point density at $t = 45\,s$. For $k_b = k_o/10$, clots have many fewer branch points. As in the zero velocity case, increasing k_b causes the clot to be initiated sooner. This is also shown in Figure 3.32. Gels formed with larger k_b not only have higher branch point densities but are larger in area at any given time. We see that this model has diffusion limited behavior.

We are unable to answer the questions, will the gels converge to the same size and if they converge, does it happen within a physiologically relevant time frame? The simulations do reveal that for different values of k_b, gels contain different size fibers and pores shown in Figure 3.33. Fiber diameters increase when k_b decreases. For large k_b, pore sizes and

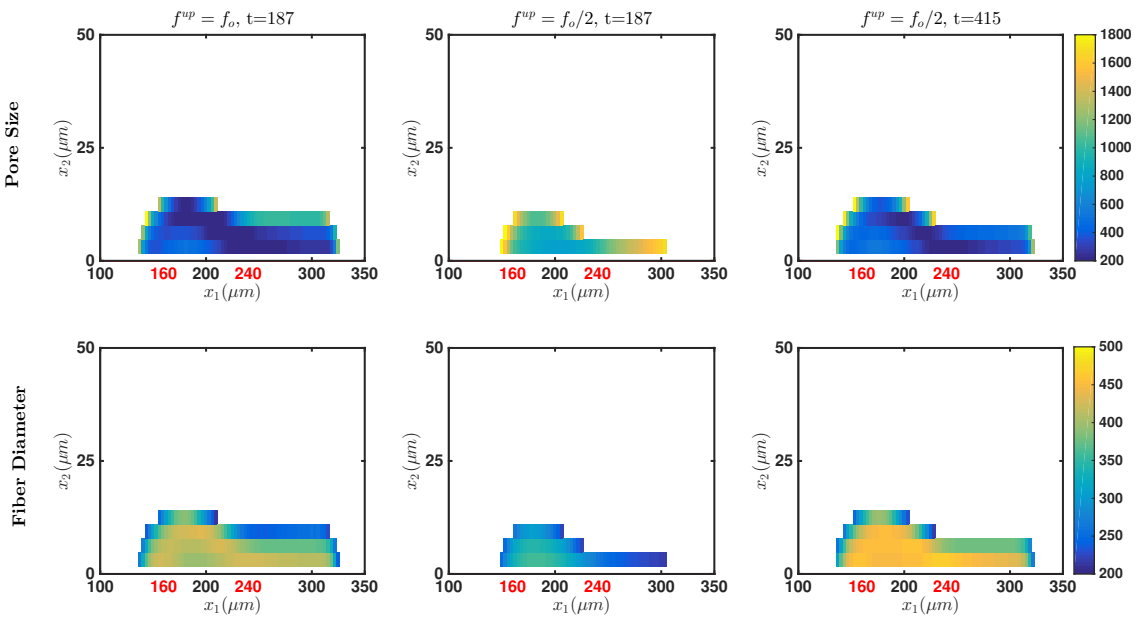

Figure 3.30: Clot size plotted for different f^{up} in flow. Top: Pore size in nm. Bottom: Fiber diameter in nm. Left: $f^{up} = 10\mu M$ at $t = 187\,s$, Middle: $f^{up} = 5\mu M$ at $t = 187\,s$, Right: $f^{up} = 5\mu M$ at $t = 415\,s$. $\gamma = 10\,s^{-1}$, $\alpha = 10^{-5}\,cm\,\mu M/s$, and $k_b = 1\,\mu M^{-2}s^{-1}$.

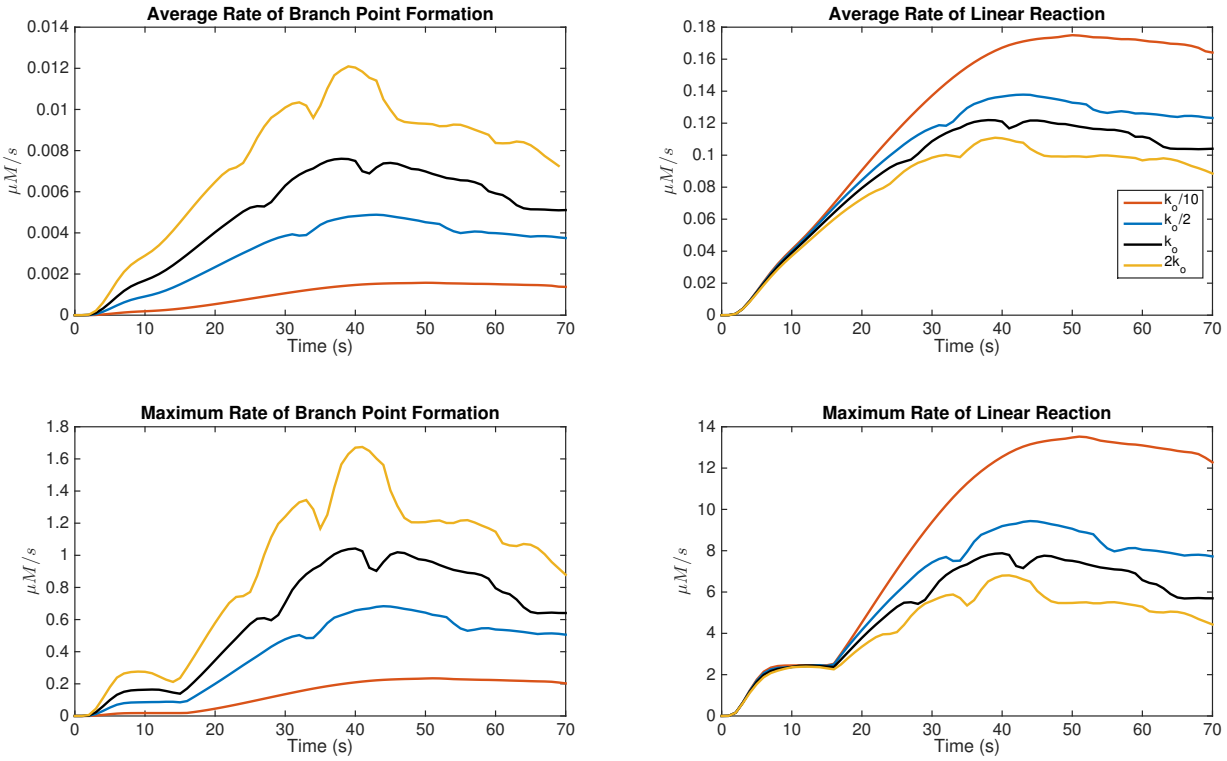

Figure 3.31: Rate of branch and linear reactions plot for different k_b. Top, left: Average rate of branch point formation. Top, Right: Linear reaction. Bottom, Left: Maximum rate of branch point formation. Bottom, Right: Linear reaction. For $k_b = k_o/10$, $k_b = k_o/2$, $k_b = k_o$, and $k_b = 2k_o$. $\gamma = 10\, s^{-1}$, $\alpha = 10^{-5}\, cm\, \mu M/s$, $k_o = 10\, \mu M^{-2} s^{-1}$, and $f^{up} = 10\, \mu M$

Table 3.3: Gel time, average number of monomers per branch point in gel, and average branch point density in gel. $k_o = 10\,\mu M^{-2}s^{-1}$, $\gamma = 10s^{-1}$ $\alpha = 10^{-4}cm\,\mu M/s$

k_b	First Gel Time t	Monomer/Branch Point	Average Branch Point Density in Gel (μM)
$k_o/10$	$21\,s$	609.45	0.0171
$k_o/2$	$10\,s$	59.59	0.234
k_o	$8\,s$	31.97	0.725
$2k_o$	$7\,s$	23.75	1.225

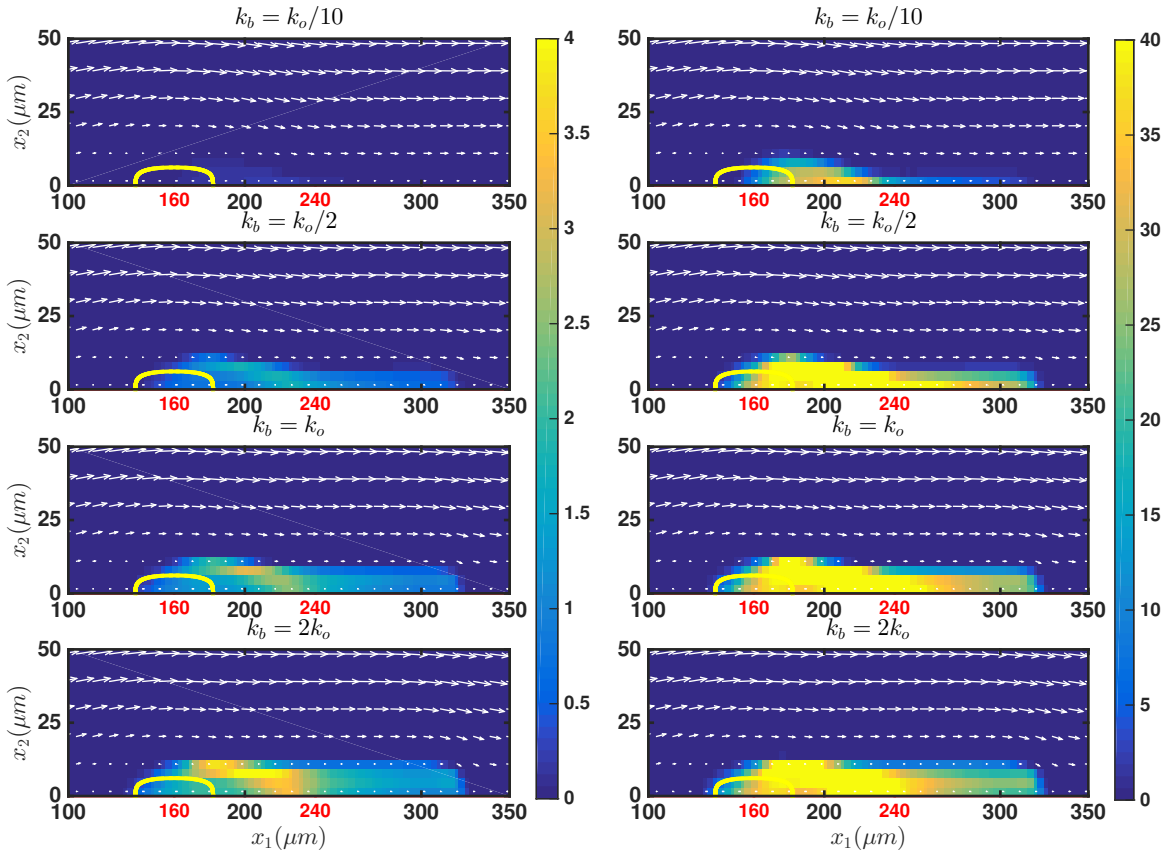

Figure 3.32: Branch point and fibrin mass density plotted for different k_b in flow. Left: Branch point density. (μM) Right: Fibrin mass density (μM). From top to bottom: $k_b = k_o/10$, $k_b = k_o/2$, $k_b = k_o$, and $k_b = 2k_o$ at $t = 45\,s$. $\gamma = 10\,s^{-1}$, $\alpha = 10^{-5}\,cm\,\mu M/s$, $k_o = 10\,\mu M^{-2}s^{-1}$, and $f^{up} = 10\,\mu M$

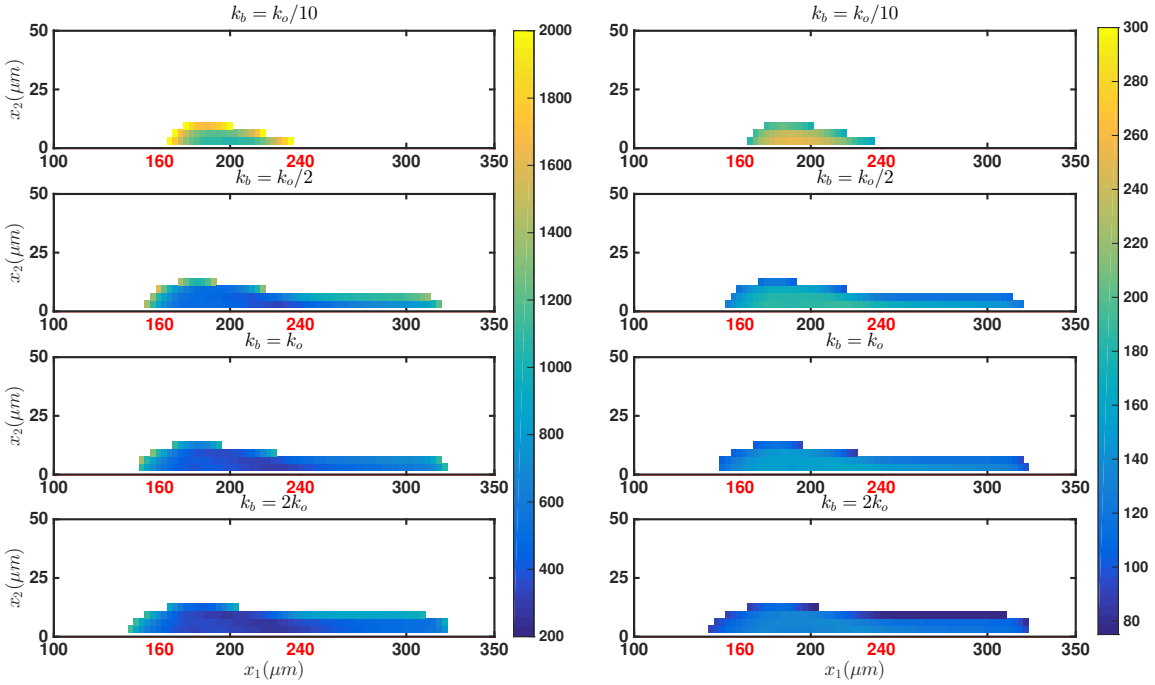

Figure 3.33: Clot structural properties, plotted for different k_b in flow. Left: Pore size (nm) Right: Fiber diameter (nm). From top to bottom: $k_b = k_o/10$, $k_b = k_o/2$, $k_b = k_o$, and $k_b = 2k_o$ at $t = 45\,s$. $\gamma = 10\,s^{-1}$, $\alpha = 10^{-5}\,cm\,\mu M/s$, $k_o = 10\,\mu M^{-2}s^{-1}$, and $f^{up} = 10\,\mu M$

diameter distribution show a clot filled with thin tightly packed fibers. As k_b decreases, fiber diameters and pore sizes become larger.

3.4 Limitations and Extensions

While this model creates a fibrin gel and gives a two-dimensional distribution of fiber diameter and pore size, the model does not explicitly model protofibril formation followed by lateral aggregation. Lateral aggregation is an important step in the thickening of fibers. The model currently uses a geometric argument that distributes the fibrin at a location evenly among branch points and uses this and the distance between branch points, i.e., $(1/B_g)^{1/3}$, to calculate fiber diameter (see Appendix A for details). This simplification does not allow for a distribution of fiber sizes at a single location. Also, it has been seen experimentally that fibers align with the fluid velocity, at least for sufficiently fast flows. Some experimentalists have seen thick fibers oriented in the direction of flow and with short thin fibers connecting them ([13], [5]). In order to model this type of behavior, the model would have account for fiber orientation and include fiber stresses and elasticity.

Currently, the model allows fibrin to accumulate in a single location without any limitation on the gel density there. This can lead to the volume fraction of fibrin becoming greater than one. At low volume fractions, proteins are able to diffuse through the fibrin gel as if it were plasma. When real fibrin accumulates, real proteins (especially large fibrin oligomers), should diffuse with a smaller diffusivity. Similarly, as the volume fraction of gel increases, so does the drag on proteins as they move through the gel. In Chapter 5, we modify the model to include some of the effects that gel has on transport while maintaining our current model framework. More extensive models, such as a 2-phase fluid model which treats fibrin gel as a fluid, might more accurately model this behavior.

CHAPTER 4

ALTERNATIVE MODEL FOR THROMBIN PRODUCTION

As shown in Chapter 3, there must be a region protected from flow for a fibrin gel to form over an injury zone. Platelets and other cells could provide such a barrier. Platelets collect on an injury site and provide a surface for the conversion of prothrombin to thrombin. In order to approximate thrombin production on platelets, not the vessel wall, we model prothrombin conversion in the fluid in and around porous beads.

4.1 Model

At the current resolution, we cannot model individual platelets. We instead model a platelet aggregate's contribution to thrombin production using a prescribed distribution of prothrombinase, that is located where a high Brinkman coefficient is prescribed to mimic the platelet thrombus' ability to hinder the flow. The aggregates are located over the injury zone, $(L_1 < x_1 < L_2)$.

This model contains four coagulation chemicals: prothrombin in the fluid, Z_2; bound prothrombin, Z_b; thrombin, E_2; and fibrinogen, F. Prothrombin in the fluid binds to prothrombinase complex P_r on platelet surfaces. The concentration of the P_r complexes is specified in each simulation. Bound prothrombin can unbind or it can be cleaved by prothrombinase to become thrombin. As before, thrombin cleaves fibrinogen into fibrin monomer. Let z_2, z_b, e_2, and f denote the concentration of prothrombin, bound prothrombin, thrombin and fibrinogen, respectively. These four concentrations are tracked by the following equations,

$$\begin{aligned}
\frac{\partial z_2}{\partial t} + \nabla \cdot (\mathbf{u} z_2) &= \nabla \cdot (D_z \nabla z_2) - k_{on}(p_r - z_b) z_2 + k_{off} z_b, && (4.1)\\
\frac{\partial z_b}{\partial t} &= k_{on}(p_r - z_b) z_2 - k_{off} z_b - k_{cat} z_b, && (4.2)\\
\frac{\partial e_2}{\partial t} + \nabla \cdot (\mathbf{u} e_2) &= \nabla \cdot (D_z \nabla e_2) - k_{at} e_2 + k_{cat} z_b, && (4.3)\\
\frac{\partial f}{\partial t} + \nabla \cdot (\mathbf{u} f) &= \nabla \cdot (D_f \nabla F) - \frac{k_f e_2 f}{k_{fs} + f}. && (4.4)
\end{aligned}$$

Here, k_{on} is the binding rate of prothrombin to prothrombinase, k_{off} is the unbinding rate, and k_{cat} is rate prothrombin is cleaved to thrombin. The parameter, p_r, is described below. Notice in Equation 4.2 that bound prothrombin does not advect or diffuse; thus the equation is effectively an ODE at each point in the domain. Along the top and bottom wall, the variables z_2, e_2, and f have no flux boundary conditions. The left and right boundaries are the same as those described in Chapter 2. All other parameters serve the same role as in the previous model. The equations for W, R, V, θ, and B are unchanged.

Because prothrombin actually binds first to a platelet's surface and then to prothrombinase, the number of prothrombin molecules bound to a platelet is limited to the smaller of the number of prothrombin receptors and the number of prothrombinase complexes. In general, the number of prothrombin receptors is the lower one and we use it to estimate the values of p_r.

It is estimated that platelets express 2000 prothrombin receptors on their membranes, or $26\, fmol/cm^2$ [4]. In the model, p_r is a volume concentration. We convert $26\, fmol/cm^2$ to a volume concentration by dividing by the average platelet aggregate height, $5.6\,\mu m$, to get $\approx 46nM$. We set the maximum receptor concentration, $\max(p_r) \equiv R_o = 50\, nM$. We simulate three p_r distributions, shown in Figure 4.1. The shape of the p_r distribution and Brinkman coefficient is given by

$$\begin{aligned} p_r &= \frac{1}{2}\tanh\left(25\left(\frac{x_1}{100} - \left(L_{mid} + \frac{3}{4}A\right)\right)\right) - \frac{1}{2}\tanh\left(25\left(\frac{x_1}{100} - \left(L_{mid} + \frac{7}{4}A\right)\right)\right) \\ &\quad \times \left(-0.5 * \tanh\left(25\left(\frac{x_2}{100} - .05\right)\right) + \frac{1}{2}\right). \end{aligned} \tag{4.5}$$

Here L_{mid} is the horizontal center of the aggregate and A describes the width of each aggregate and is selected to be 0.2133.

The initial Brinkmann coefficient is co-localized with each of the p_r distributions and is physiologically similar to those for platelet aggregates. The first distribution represents two aggregates that overlap; the centers of the aggregates are located at $x_1 = 186\,\mu m$ and $x_1 = 214\,\mu m$. The second distribution represents two aggregates whose centers are separated by $57\,\mu m$. The centers of these aggregates are located at $x_1 = 173\,\mu m$ and $x_1 = 230\,\mu m$. The third distribution represents two aggregates whose centers are separated by $103\,\mu m$. The centers of these aggregates are located at $x_1 = 148\,\mu m$ and $x_1 = 251\,\mu m$. Each aggregate represents about 100 platelets.

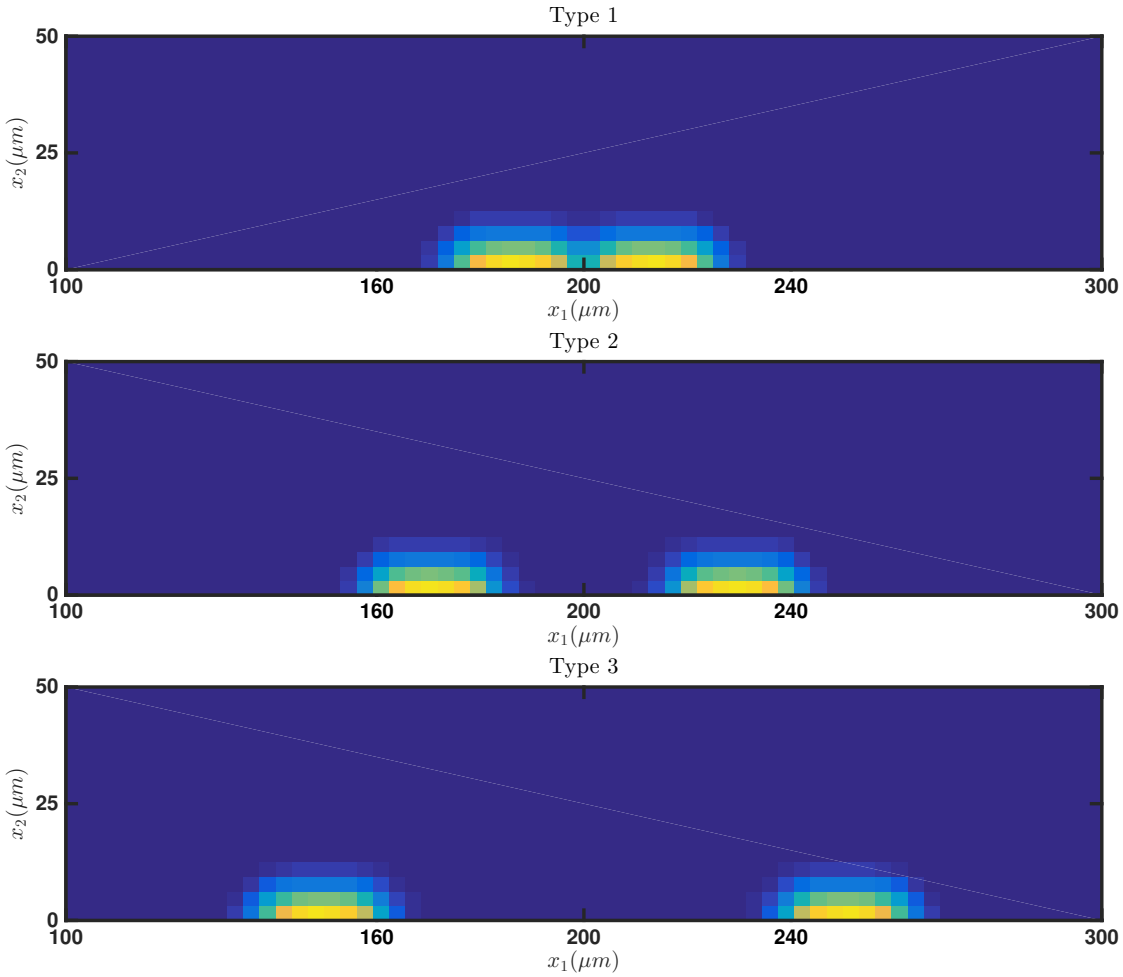

Figure 4.1: Prothrombinase/Factor II distributions. Three types of concentration distributions for p_r in nM. The white arrow indicates the relative magnitude and velocity of the fluid. The Brinkman coefficient distributions have the same form.

4.2 Results

We look at events in a blood vessel segment of length $400\,\mu m$ and height $100\,\mu m$. For all the results described below, the wall shear rate is $\gamma = 10\,s^{-1}$ and the branching rate is $k_b = 10^{-6}\,\mu M s^{-1}$. All other parameter values are listed in Appendix B.

There are several important differences between this model and the model described in Chapter 2. First, prothrombin is converted to thrombin in a portion of the fluid instead of on the wall. Second, the Brinkman coefficient is highest in the regions where thrombin is produced. For each of the p_r distributions, the fluid moves slowly in the region over the injury. This yields a Peclet number less than 1, which indicates that, in the region, diffusion is the dominant form of transport. Consequently, fibrin monomer production acts similarly to the zero velocity case described in Chapter 3.

Initially, thrombin and fibrin are produced over the entire region where prothrombinase is located (instead of only along the bottom wall). Then prothrombin and fibrinogen become depleted in the interior of the region. Although prothrombin and fibrinogen advect into the domain with the fluid, the nature of the velocity field near the platelet aggregates causes the proteins to move mostly up and around the platelet aggregates. Hence, fibrinogen is then converted to fibrin on the edge of the protected region giving rise to the distributions seen in the first row of Figure 4.2. Because the fibrinogen and prothrombin advect with the fluid, the upstream side of the platelet aggregates sees a higher source rate yielding a higher branch point density and a higher fibrin mass density.

The different p_r and Brinkman coefficient distributions result in different fluid profiles. The horizontal and vertical velocity profiles are shown in Figure 4.3. In the simulations using any of the three p_r and Brinkmann coefficient distributions, the vertical fluid component shows that the fluid flows toward the center of the vessel on the upstream side of the platelet aggregates and toward the vessel wall on the downstream side of the aggregates. The distance between the two aggregates affects the fluid profiles. In the simulation using the type 1 distribution, the two platelet aggregates act as a single aggregate. In the simulation using the type 3 distribution, the fluid flows between the platelet aggregates. In the simulation using the type 2 distribution, the fluid velocity between the platelet aggregates is slower compared to the type 3 distribution.

While all three types of p_r and Brinkman coefficient distributions represent the same number of platelets, the total fibrin density in each is different. Because type 3 has a larger region protected from flow and it has significant fluid flow between the platelet aggregates that advects more fibrinogen and prothrombin, it has the highest total fibrin

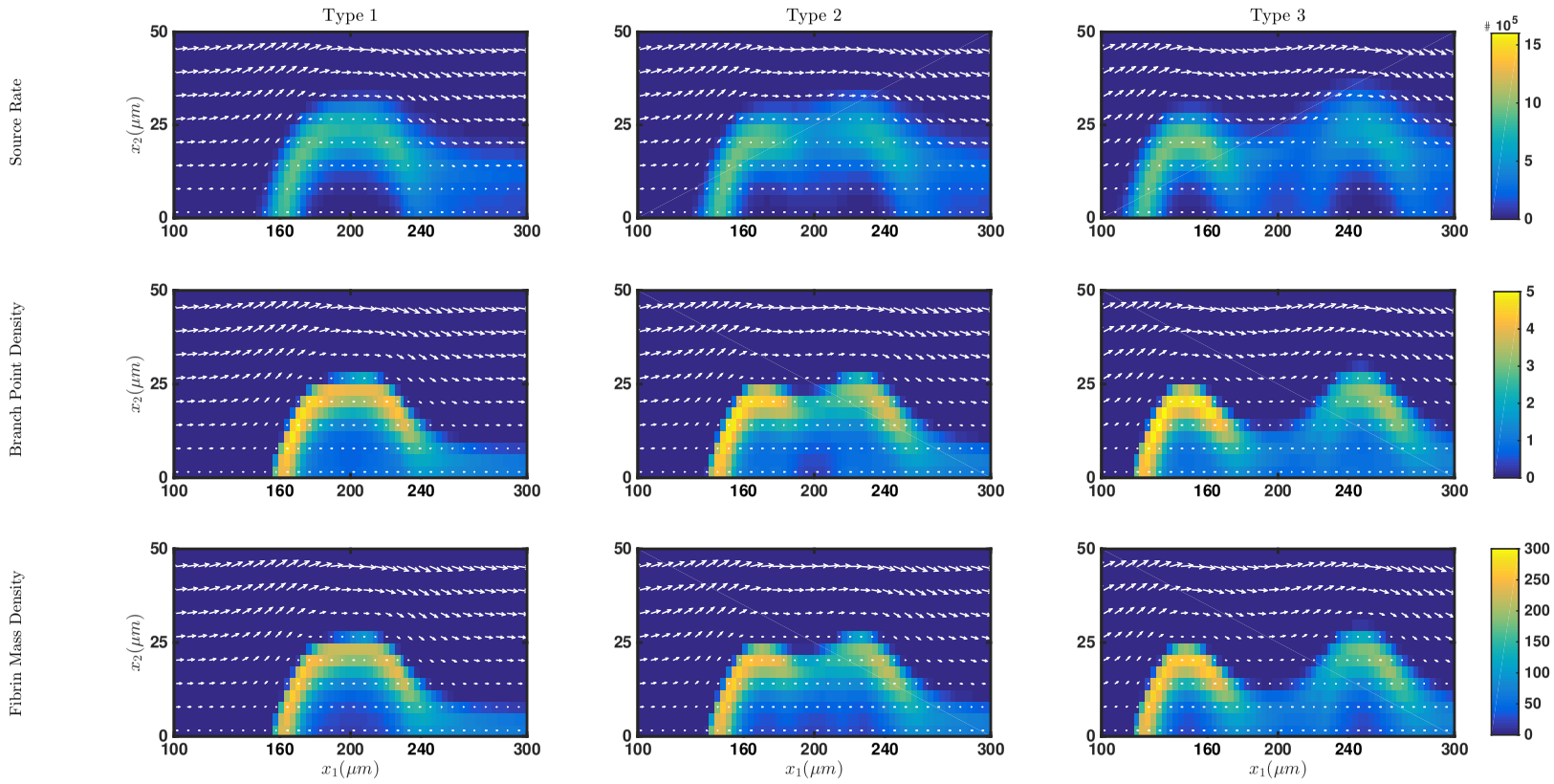

Figure 4.2: Source rate and gel distributions for alternative model. Top: Source Rate (top) in $\mu M/s$. Middle: Branch Point Density in the gel in μM. Bottom: Fibrin Mass Density in the gel in μM. Taken at t = 80 s. Each column is for a different p_r distribution from left to right: Type 1, Type 2, Type 3.

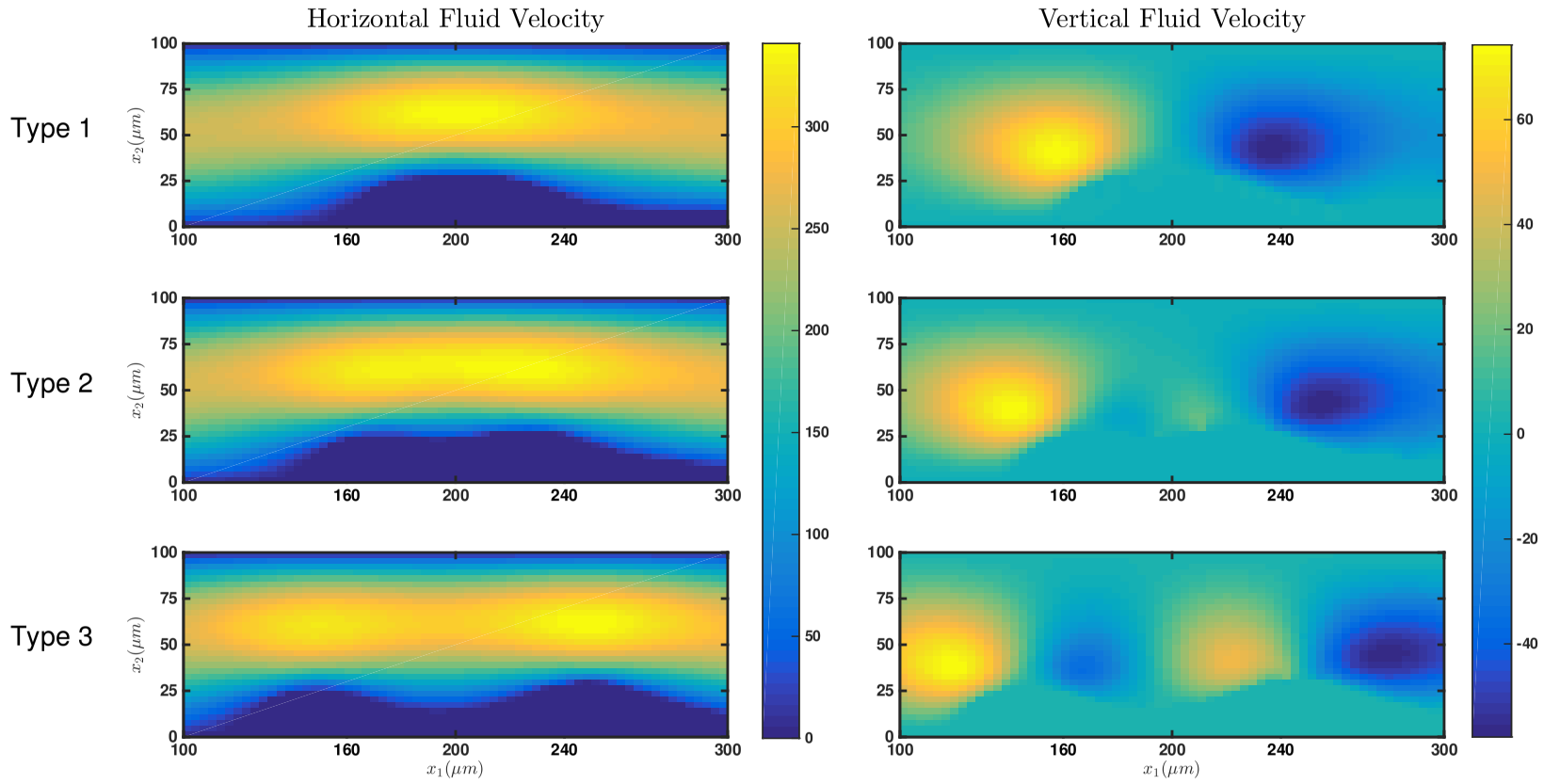

Figure 4.3: Horizontal and vertical fluid velocity profiles by p_r distribution types. Type 1 p_r distribution vertical fluid velocity component (top left), horizontal fluid velocity component (top right). Type 2 p_r distribution vertical fluid velocity component (middle left), horizontal fluid velocity component (middle right). Type 1 p_r distribution vertical fluid velocity component (bottom left), horizontal fluid velocity component (bottom right). The units are $\mu m/s$.

density ($3.97 \times 10^4 \mu M$), followed by type 2 ($3.45 \times 10^4 \mu M$), then by type 1 ($2.87 \times 10^4 \mu M$) at 250 seconds. Here the total fibrin density is defined as the sum of the fibrin mass density over the whole domain. This is also verified by looking at the difference between the source rate of fibrin over the whole domain and the rate that fibrin mass density in the sol leaves the domain with the fluid.

$$r(t) = \int_0^t \int_0^{100} \int_0^{400} Source(x_1, x_2, t) dx_1 dx_2 dt - \int_0^t \int_0^{100} u\theta_s dx_2 dt \tag{4.6}$$

Here u is the horizontal fluid velocity at $x_1 = 400\mu m$, the right edge of the domain. The function $r(t)$ describes the total amount of fibrin that is in the domain at time, t and is shown in Figure 4.4. For all time after seven seconds, type 3 has the most fibrin in the domain, followed by the type 2, then type 1.

Figure 4.5 shows the pore size, fiber diameter, and clotting time for each p_r and Brinkmann coefficient distribution type. From the clotting times, we see that most of each clot forms within the first 30 s. The median clotting times for Type 1, 2, and 3 are 21s, 20s, and 26.5s, respectively. For all three types, fiber diameters range from 100-300 nm. The fiber diameters are smallest near the horizontal center of the aggregates. The fibers on the outside of the platelet aggregate continue to thicken over time and therefore have a larger fiber diameter.

4.3 Conclusion

From the alternative model for thrombin production, we are able to see the effects that platelet aggregates have on fibrin clot formation and structure. Although the model did not include individual platelets, it did include the impact that platelet aggregates have on flow with the use of a Brinkman term. The flow around the platelet aggregates is slowed and allows enough of a protected area for fibrin fibers to form. The concentration of prothrombinase located in the same spacial positions as the large Brinkman term allows for thrombin to be produced in a larger area (not just at the vessel wall) which affects the fibers as well as the time the clot formation. The size and position of the platelet aggregates affects the structure properties of the fibrin clots that form.

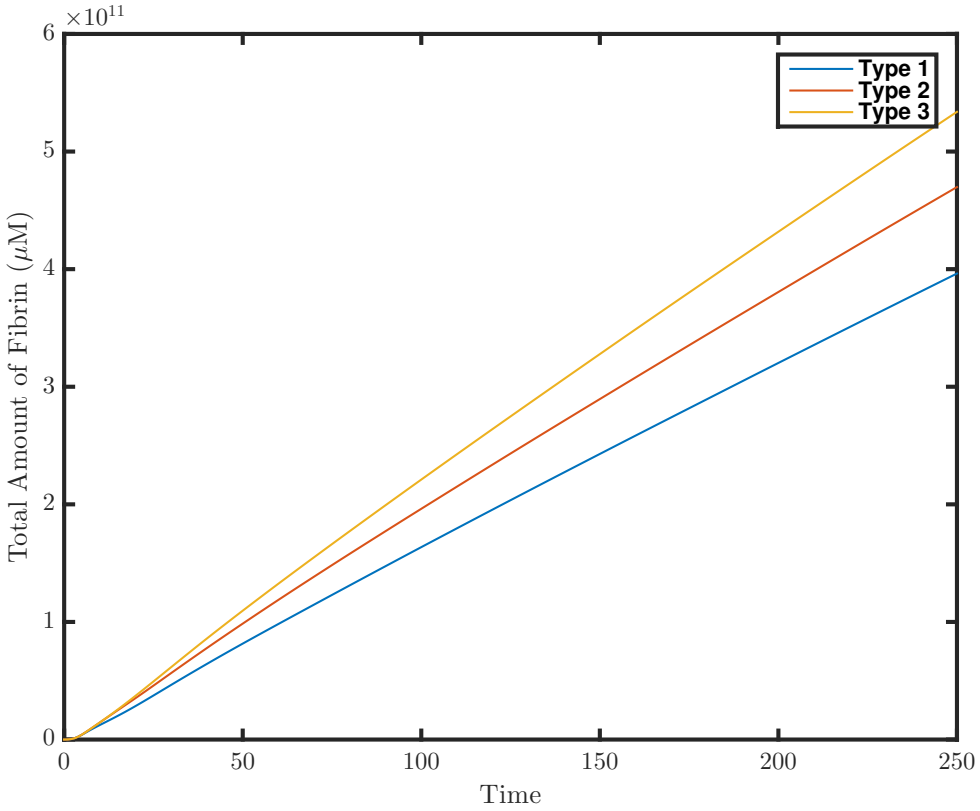

Figure 4.4: Total amount of fibrin by p_r type.

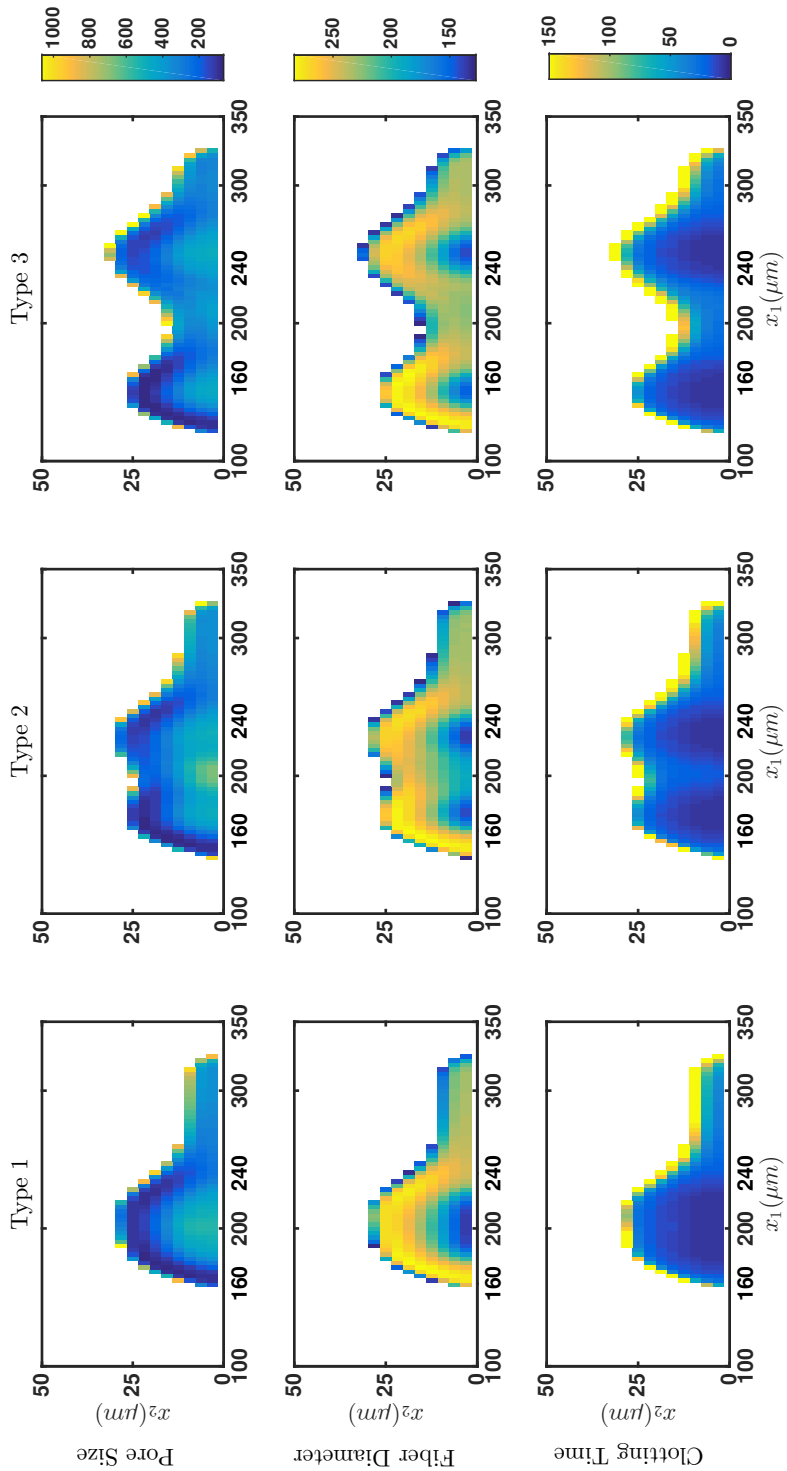

Figure 4.5: Clot structural properties for alternative model. Top row: Pore Size in nm. Middle Row: Fiber Diameter in nm. Bottom Row: Clotting Time in s. Taken at t = 80 s. Each column is for a different p_r distribution from left to right: Type 1, Type 2, Type 3.

CHAPTER 5

HINDERED TRANSPORT

Because fibrin gel, even with volume fraction less than 0.1, affects the diffusion coefficient of protein [41] and proteins moving through a gel (especially with high volume fraction) experience drag, we seek to create a model that includes effects of volume fraction exclusion without explicitly including a full two-state fluid/gel model. In order to derive the correct modifications, we follow Leiderman and Fogelson 2013 [21] and unpublished notes by Fogelson [9].

These changes also address a limitation of the model described in Chapter 2. That model does not contain any mechanisms that restrict the amount of fiber gel that can be present at each specific location. In fact, the volume fraction of gel can become greater than one. Clearly, this is not physiological. In this chapter we modify the model to include terms that hinder the advection and diffusion of coagulation proteins and oligomers in the presence of higher volume fraction of gel. By restricting the movement of molecules in the solvent, we limit gel accumulation.

5.1 Derivation

We begin by looking at a three species system of free protein, gel and fluid. Let $(\theta_{pr}, \mathbf{u}_{pr}), (\theta_g, \mathbf{u}_g)$, and $(\theta_f, \mathbf{u}_f)$ be the volume fraction and velocities of protein, gel, and fluid, respectively. The sum of the volume fractions must be one. The force balance equation for protein is

$$0 \;=\; \xi_{pr,f}\theta_{pr}\theta_f(\mathbf{u}_f - \mathbf{u}_{pr}) + \xi_{pr,g}\theta_{pr}\theta_g(\mathbf{u}_g - \mathbf{u}_{pr}) - \theta_{pr} \bigtriangledown \mu_{pr}. \tag{5.1}$$

Here, $\xi_{pr,f}$ is the drag coefficient between fluid and protein, $\xi_{pr,g}$ is the drag coefficient between the gel and protein, and μ_{pr} is the protein chemical potential. Typically, $\mu_{pr} = k_B T \log c_{pr}$, where c_{pr} is the concentration of protein, k_B is the Boltzmann constant, and T is the temperature in Kelvin. The concentration of a protein is defined as the amount per total volume. However, we are interested in a system where any given volume can be occupied by both fluid and gel. Since proteins reside only in the solvent, the effective concentration of protein is defined as the amount per solvent volume, $\tilde{c}_{pr} = c_{pr}/\theta_f$. Let

$\mu_{pr} = k_B T \log \tilde{c}_{pr}$ which is a reasonable choice if the protein is dilute. Assuming that the gel is stationary, $\mathbf{u}_g = 0$, and proteins are dilute, $\theta_{pr} << 1$, we can solve (5.1) for $\mathbf{u}_{pr}$,

$$\mathbf{u}_{pr} = \frac{\xi_{pr,f}(1-\theta_g)}{\xi_{pr,f} + (\xi_{pr,g} - \xi_{pr,f})\theta_g}\mathbf{u}_f - \frac{1}{\xi_{pr,f} + (\xi_{pr,g} - \xi_{pr,f})\theta_g} k_B T \bigtriangledown \log \frac{c_{pr}}{\theta_f}. \tag{5.2}$$

Define r to be the ratio of the drag coefficients, $r = \xi_{pr,g}/\xi_{pr,f}$, and define the unhindered diffusion coefficient of protein in fluid to be $D_o = k_B T/\xi_{pr,f}$. Then (5.2) can be rewritten as

$$\mathbf{u}_{pr} = \frac{(1-\theta_g)}{1 + (r-1)\theta_g}\mathbf{u}_f - \frac{1}{1 + (r-1)\theta_g} D_o \bigtriangledown \log \frac{c_{pr}}{\theta_f}. \tag{5.3}$$

Applying the quotient rule for derivatives, and using $\theta_f \approx 1 - \theta_g$, since $\theta_{pr} << 1$,

$$\mathbf{u}_{pr} = \frac{(1-\theta_g)}{1 + (r-1)\theta_g}\mathbf{u}_f - \frac{D_o}{1 + (r-1)\theta_g}\left(\bigtriangledown c_{pr} - c_{pr}\frac{\bigtriangledown(1-\theta_g)}{1-\theta_g}\right). \tag{5.4}$$

The continuity equation for protein is

$$\frac{\partial \theta_{pr}}{\partial t} + \bigtriangledown \cdot (\mathbf{u}_{pr}\theta_{pr}) = Rxn(\theta_{pr}). \tag{5.5}$$

Here Rxn represents general reaction terms for reactions that change c_{pr}. We are interested in rewriting Equation 5.5 in terms of c_{pr}, the amount of protein per total volume. Let V_{pr} be the volume of a mole of protein. Then $c_{pr} = V_{pr}\theta_{pr}$, and

$$\frac{\partial c_{pr}}{\partial t} + \bigtriangledown \cdot (\mathbf{u}_{pr} c_{pr}) = Rxn(c_{pr}) \tag{5.6}$$

$$\frac{\partial}{\partial t}(\theta_f \tilde{c}_{pr}) + \bigtriangledown \cdot (\mathbf{u}_{pr}\theta_f \tilde{c}_{pr}) = Rxn. \tag{5.7}$$

Since,

$$\theta_f \tilde{c}_{pr}\mathbf{u}_{pr} = \frac{(1-\theta_g)}{1 + (r-1)\theta_g}\mathbf{u}_f \theta_f \tilde{c}_{pr} - \frac{D_o \theta_f \tilde{c}_{pr}}{1 + (r-1)\theta_g}\left(\bigtriangledown c_{pr} - c_{pr}\frac{\bigtriangledown(1-\theta_g)}{1-\theta_g}\right), \tag{5.8}$$

we obtain the expression,

$$\begin{aligned} \frac{\partial c_{pr}}{\partial t} &+ \bigtriangledown \cdot \left\{\frac{(1-\theta_g)}{1 + (r-1)\theta_g}\mathbf{u}_f c_{pr}\right\} + \bigtriangledown \cdot \left\{\frac{D_o c_{pr}}{1 + (r-1)\theta_g}\frac{\bigtriangledown(1-\theta_g)}{1-\theta_g}\right\} \\ &= \bigtriangledown \cdot \left\{\frac{D_o}{1 + (r-1)\theta_g} \bigtriangledown c_{pr}\right\} + Rxn. \end{aligned} \tag{5.9}$$

We identity the hindrance terms to be

$$H_u = \frac{(1-\theta_g)}{1 + (r-1)\theta_g} \tag{5.10}$$

$$H_d = \frac{1}{1 + (r-1)\theta_g} \tag{5.11}$$

$$\mathbf{u}_{vol} = \frac{1}{1 + (r-1)\theta_g}\frac{\bigtriangledown(1-\theta_g)}{1-\theta_g}. \tag{5.12}$$

Here, H_u accounts for the drag a protein feels from the presence of a gel, H_d accounts for the reduced diffusion of protein because of the presence of gel , and $\mathbf{u}_{vol}$ is a velocity term that

moves proteins from regions of high gel volume fraction to regions of low volume fractions at a rate proportional to the gradient of gel volume fraction.

Next, we look at the reaction terms by following unpublished notes by Fogelson [10]. We consider a condensation reaction,

$$C_i + C_j \underset{k_-}{\overset{k_+}{\rightleftharpoons}} C_k. \tag{5.13}$$

Let Ω be a domain with volume V_Ω. The above reactions occur only in the fluid, therefore the concentration that appears in mass action terms should be the concentration per solvent volume; $\tilde{c}_i, \tilde{c}_j$, and $\tilde{c}_k$. The equations which describes the rate of change of the number of C_k molecules in volume V_Ω is

$$V_\Omega \frac{d}{dt} c_k = \left(k_+ \tilde{c}_i \tilde{c}_j - k_- \tilde{c}_k\right) \theta_f V_\Omega. \tag{5.14}$$

Then substituting $c_n = \frac{\tilde{c}_n}{\theta_f}$, where $n \in \{i, j, k\}$, we find that

$$\begin{aligned} \frac{d}{dt} c_k &= \left(k_+ \frac{c_i}{\theta_f} \frac{c_j}{\theta_f} - k_- \frac{c_k}{\theta_f}\right) \theta_f & (5.15) \\ &= \frac{k_+}{\theta_f} c_i c_j - k_- c_k. & (5.16) \end{aligned}$$

For bimolecular reaction, the reaction rate is scaled by the volume fraction of fluid. For degradation reactions and other reactions involving only one protein, there is no scaling. We perform the same analysis on trimolecular reactions and find that the reaction rate must be scaled by θ_f^2. For the general enzymatic reaction,

$$S + E \underset{k_-}{\overset{k_+}{\rightleftharpoons}} C \xrightarrow{k_{cat}} P + E, \tag{5.17}$$

we can follow the same analysis as above and the standard quasi-steady state reduction to find that the modified Michaelis-Menten rate is

$$\frac{k_{cat} S E}{\theta_f k_M + S}, \tag{5.18}$$

where $k_M = \frac{k_- + k_{cat}}{k_+}$.

5.2 Model

We use the analysis above to modify the equations in Chapter 2 to include a coefficient describing resistance to fluid advection, $H_{u,i}$, a coefficient describing hindered diffusion, $H_{d,i}$ and a new advection term that moves proteins due to a gradient in volume fraction, $\mathbf{u}_{vol,i}$. Here $i \in \{z, f, c\}$. The subscript z is used for the prothrombin and thrombin equations.

The subscript f is used for the fibrinogen equation. The subscript c is used for the gelation equations. This choice is consistent with the assumption that diffusion it not dependent on oligomer size. The complete list of equations is given in Appendix C. Below is the modified equation for R as an example for the reader.

$$\begin{aligned} \frac{\partial R(\mathbf{x},t)}{\partial t} &+ \nabla\cdot(H_{u,c}\mathbf{u}R_s) + \bigtriangledown\cdot(D_c\mathbf{u}_{vol,c}R_s) \\ &= \nabla\cdot(H_{d,c}D_c\nabla R_s) - \frac{k_l}{\phi_f}\left(R^2-R_g^2\right) - \frac{k_b}{2\phi_f^2}\left(R^3-\left(3R_sR_g^2+R_g^3\right)\right) + 2\tilde{S}_{10}. \end{aligned} \tag{5.19}$$

Here $\tilde{S}_{10} = \frac{k_f e_2 f}{\phi_f k_{fs}+f}$. The boundary conditions for R along the top and bottom walls are also modified to include the additional flux terms. Define $v_{vol,i}$ to be the component of $\mathbf{u}_{vol,i}$ in the x_2-direction. Because the right boundary condition is nonphysical and the left boundary condition is not dependent on flux, they are not altered.

$$R(0,x_2,t) = 0, \tag{5.20}$$

$$\frac{\partial R(L_{x_1},x_2,t)}{\partial x_1} = 0, \tag{5.21}$$

$$-D_c\frac{\partial R(x_1,L_{x_2},t)}{\partial x_2} = -D_c\frac{\partial R_g}{\partial x_2} - \frac{D_c v_{vol,c}}{H_{d,c}}\left(R-R_g\right), \tag{5.22}$$

$$-D_c\frac{\partial R(x_1,0,t)}{\partial x_2} = -D_c\frac{\partial R_g}{\partial x_2} - \frac{D_c v_{vol,c}}{H_{d,c}}\left(R-R_g\right). \tag{5.23}$$

5.2.1 Ratio of Drag Coefficients

The parameter, r, is the ratio of the drag coefficients between fluid and protein and gel and protein. We find this parameter for each protein type using data published, figure 22.7 in ([41]) where the diffusivities of macromolecule tracers were calculated as a function of the volume fraction of fibrin. Two of the macromolecule tracers used were 70 kDa and 500 kDa, which are similar to the size of prothrombin (72 kDa) and fibrinogen (340 kDa), respectively. We use these experimental data to estimate r_z and r_f. Because oligomers are composed of fibrin monomers, we let $r_c = r_f$. We rearrange Equation 5.11 to solve for r,

$$r = \frac{1-H_d}{H_d\phi_g} + 1. \tag{5.24}$$

Figure 5.1 shows the values of r calculated by fitting a line to experimental data from ([41]). We find

$$r_z = 26.55\,\phi_g + 1 \tag{5.25}$$

$$r_f = 47.53\,\phi_g + 1. \tag{5.26}$$

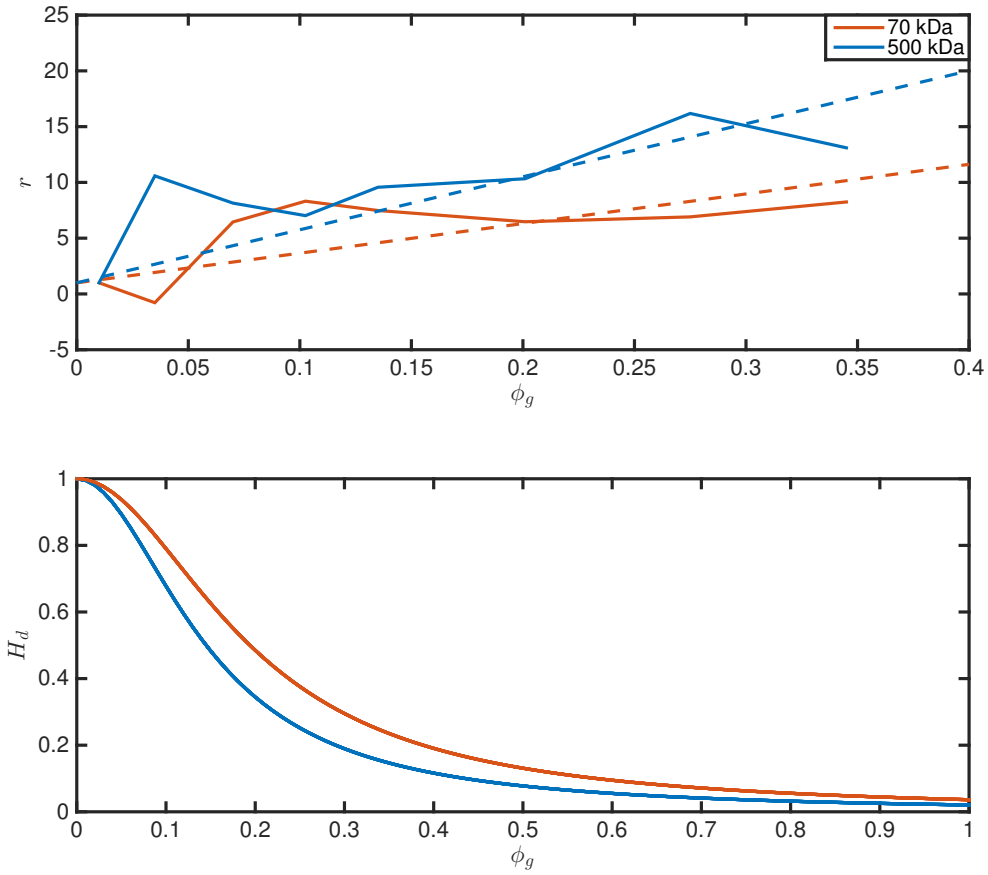

Figure 5.1: Drag coefficient ratio for hindered transport. The top plot shows the value r as a function of volume fraction of gel. The solid line is data, the dash line is a linear fit. The bottom plot shows H_d as a function of ϕ_g using the linear equation for r. In both plots, red and blue use data for macromolecules that are 70 kDa and 500 kDa, respectively.

5.3 Results

We look at events in the blood vessel segment of length $400\mu m$ and height $100\mu m$. In the injury zone, there are two separated "bumps" with high Brinkman coefficients. Thrombin is produced along the bottom vessel wall where the bumps are located. The Brinkman coefficient distribution and spacial dependence of α is shown in Figure 5.2.

For the simulations described below, $\gamma = 10s^{-1}$ and $k_b = 1\mu M^{-2}s^{-1}$. The volume fraction of the gel is a function of the fibrin mass density, we take

$$\phi_g = N_a V_f \theta_g, \tag{5.27}$$

where N_a is Avogadro's number, V_f is the volume of a single fibrin molecule. In order to decrease computational time, we take

$$\phi_g = 50 N_a V_f \theta_g, \tag{5.28}$$

to increase the influence fibrin mass has on the hindered transport coefficients and velocities.

We compare the hindered transport model with a baseline model, where $H_{d,i} = 1$, $H_{u,i} = 1$, and $\mathbf{u}_{vol,i} = 0$ for $i \in \{z, f, c\}$. Initially, the two models behave similarly. Once a gel appears the diffusivity and advection of proteins inside of the gel is lowered. This causes a decrease in the source rate of fibrin monomer. Figure 5.3 shows how the spatial-average of the fibrin source rate varies over time for simulation with the two models. The two curves diverge once the gel begins to hinder the transport of prothrombin, thrombin, and fibrinogen. Figure 5.4 shows the fibrinogen and thrombin concentration and the monomer source rate distributions for both models. It also includes the difference between them (baseline concentrations minus hindered transport concentrations). Figure 5.5 shows the branch point density in sol and the branch point and fibrin mass densities in the gel for both models as well as their difference. Both figures are taken at $t = 75s$. At this time, two gels have formed in the areas where the Brinkman coefficient is highest. The high density of fibrin mass in the gel affects the transport of the proteins. Figure 5.4 shows that in the hindered transport model, the fibrinogen concentration is higher outside of the gel than in the baseline model. This is due to fibrinogen's hindered diffusivity. Because the thrombin concentration is lowered on the exterior of the gel and the fibrinogen concentrations are lowered inside the gel, the fibrin source rate is slower almost everywhere as compared with the baseline model. Figure 5.4 shows that in particular there is a significant reduction of fibrin source inside of the gel near the wall. In regions with the highest fibrin mass densities, the diffusion coefficients for fibrinogen and fibrin oligomers are lowered by almost 75%. Figure 5.5 shows

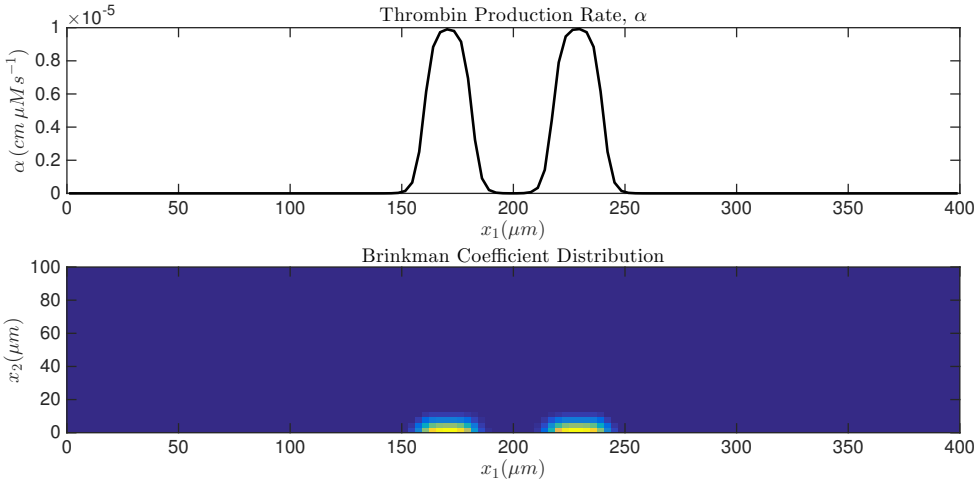

Figure 5.2: Spatial dependence of thrombin production rate and Brinkman coefficient. Top: Thrombin production rate along the bottom wall with maximum value of $10^{-5}\,cm\mu Ms^{-1}$. Bottom: Brinkman coefficient distribution.

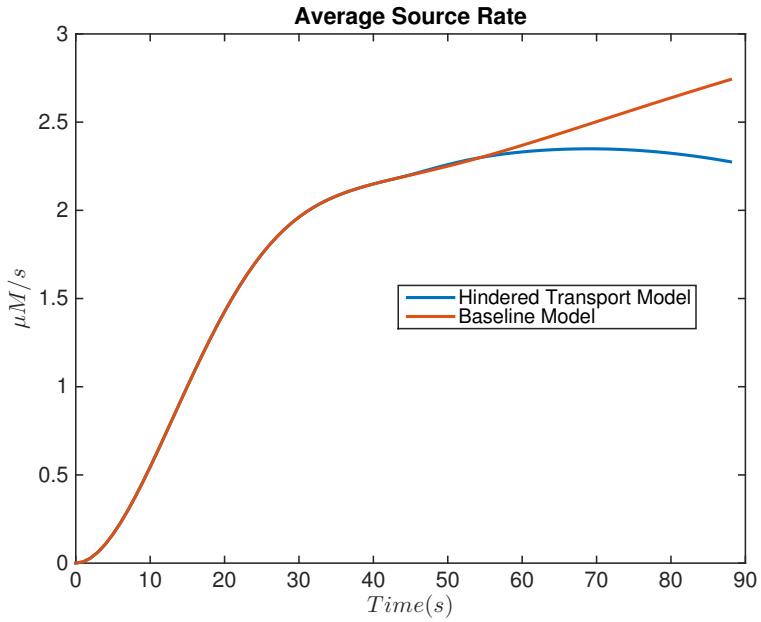

Figure 5.3: Average source rate with hindered transport. The spatial-average of the fibrin monomer source rate over time for the hindered transport model (blue) and the baseline model (red).

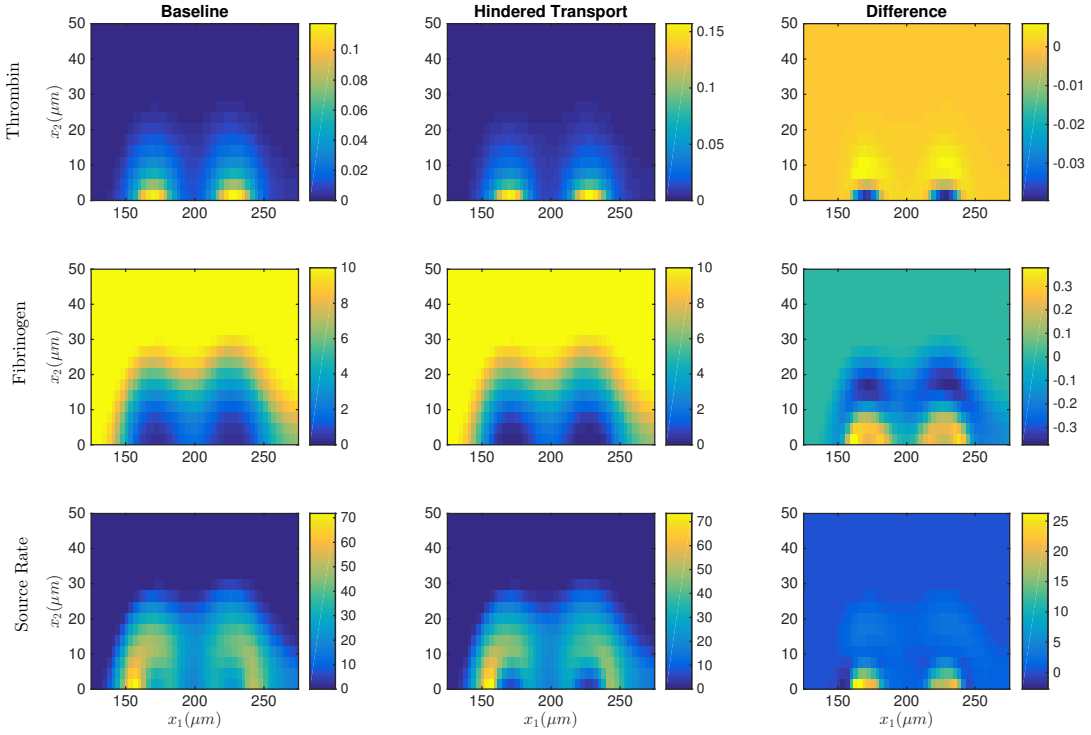

Figure 5.4: Thrombin, fibrinogen and source rate distributions with hindered transport. Top: Thrombin distribution in μM. Middle: Fibrinogen distribution in μM. Bottom: Source rate of fibrin monomer in $\mu M/s$. From left to right, baseline concentrations, hindered transport concentrations, and the difference between the two. $t = 75s$

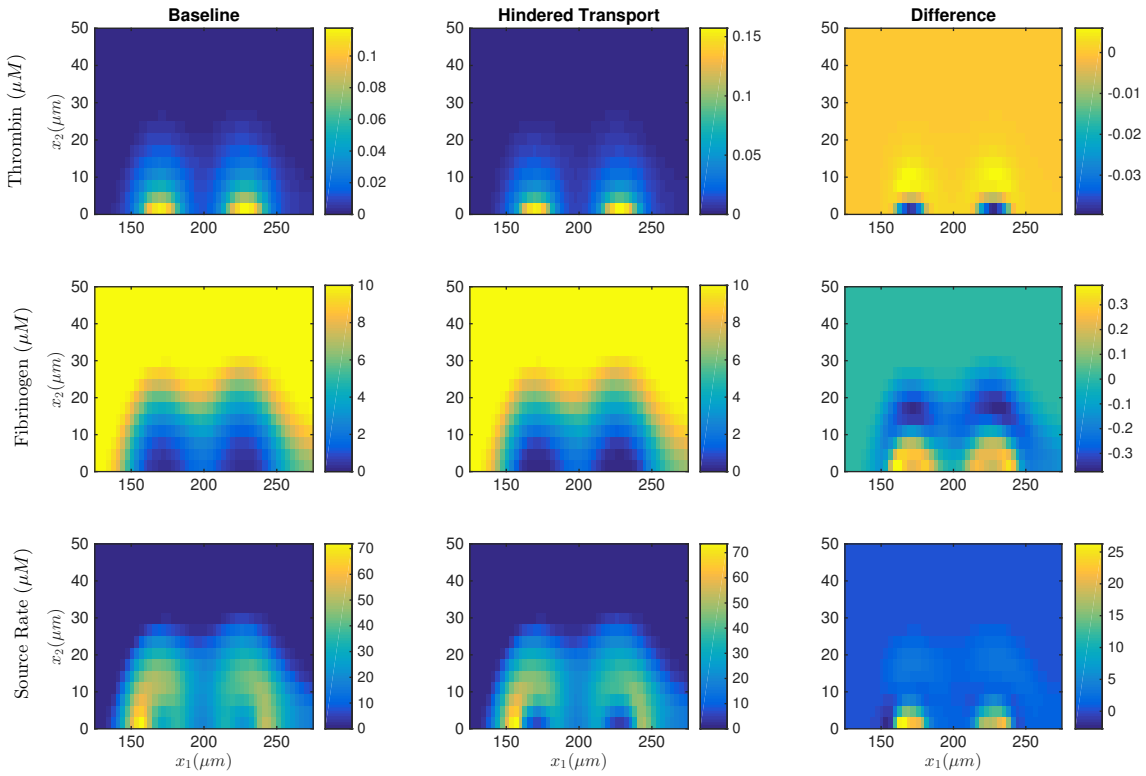

Figure 5.5: Branch point density and fibrin mass density distributions with hindrance. Top: Branch point density distribution in sol in μM. Middle: Branch point density distribution in the gel in μM. Bottom: Fibrin mass density in gel μM. From left to right, baseline concentrations, hindered transport concentrations, and the difference between the two. $t = 75s$

that in the center of the gel there is a lower branch point density and fibrin mass density for the hindered transport model than for the baseline model. The lower densities are due to a decrease in the source rate of fibrin monomers. Proteins are moved out of the region of high fibrin mass densities in the gel.

The velocity $\mathbf{u}_{vol}$ moves proteins away from areas with a high volume fraction of gel. Figure 5.6 shows the velocity vectors for $\mathbf{u}_{vol,c}$ and the distribution of fibrin mass density in the gel at $t = 75\,s$. The maximum value of $\mathbf{u}_{vol}$ is $0.1403\,\mu m/s$ which is on the same order of magnitude as the horizontal fluid velocity within the gel.

The magnitude and direction of $\mathbf{u}_{vol}$ are functions of the gradient of the volume fraction of gel. The volume fraction of gel is highest at the bottom vessel wall and decreases as one moves toward the center of the vessel so the vertical component of $\mathbf{u}_{vol}$ is generally pointed upward. The horizontal component points outward from the local maximum volume fraction. Along the lower wall, where the fibrin density is highest, $\mathbf{u}_{vol}$ appears to be essentically zero (no velocity vector is visible). The vectors actually point downward and to the left but are not visible in the figure. It should be noted that due to the boundary condition (which includes the flux terms attributed to $\mathbf{u}_{vol}$), proteins do not cross the boundary.

We have presented a model of fibrin polymerization which includes hindered transport due to the resulting gel. This is dynamically a more realistic model of the gelation process than the model described in Chapter 2. However, this modified model is not fully explored here and is shown more as a proof of concept. There are several possible attributes of the model that cause concern. Because the fluid velocity and $\mathbf{u}_{vol}$ are on the same order of magnitude, it is possible that summing their components, as one does when advecting proteins, can result in enhanced motion, hindered motion, or no net motion. If there is no net motion, this can result in an accumulation point. Accumulation points are a concern because the hinder transport model has a singularity when the volume fraction of fluid is zero. The model needs to be further tested to verify its validity and limitations, especially when the volume fraction of fluid is low.

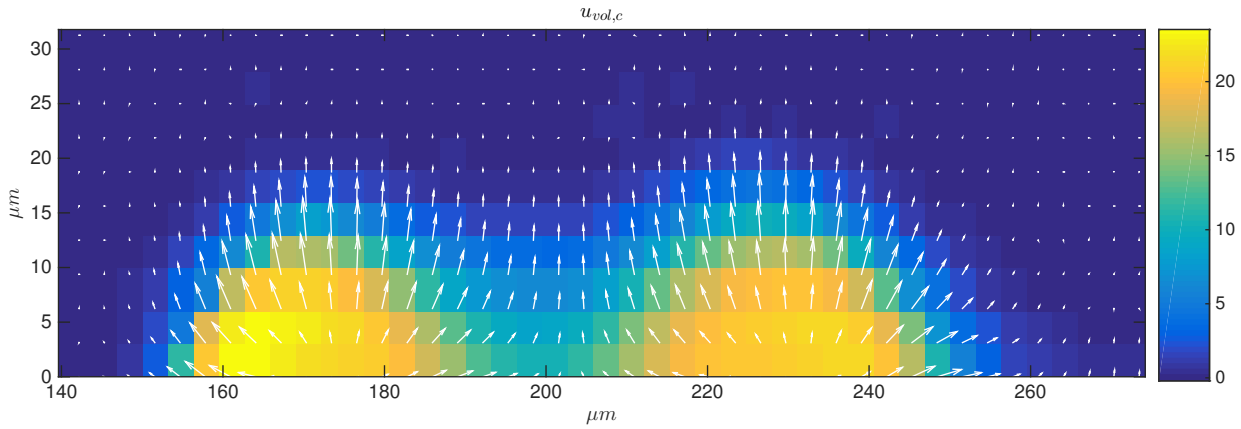

Figure 5.6: Hindrance velocity in a fibrin mass density distribution (μM). The vectors represent the velocity, $\mathbf{u}_{vol,c}$ at $t = 75s$ in $\mu m/s$. The largest arrow describes a velocity of 0.1403 μ/s.

CHAPTER 6

NUMERICS

To simulate the models described in the previous chapters, we use finite difference and finite volume methods. Toward that purpose, we discretize the domain Ω using an $N_x \times N_y$ Cartesian grid with equal spacing h in the x_1 and x_2 directions. Figure 6.1 shows the grid and the indexing conventions used throughout this chapter for a generic concentration c. the time step is denoted k. Let $c^n(x)$ denote the numerical approximation to the exact solution $c(x, nk)$ at grid points x. The independent variable z is discretized using N_z variably spaced points.

The modified Navier-Stokes equations are simulated using a finite-difference-based projection method. For these equations, a Marker-and-Cell (MAC) grid is used. The x_1 component of the fluid velocity is defined at the centers of the left and right (LR) cell edges, and the x_2 component of the velocity is defined at the centers of the top and bottom (TB) cell edges. The pressure is defined at the center of cells. The coagulation and gelation equations are discretized with finite-difference and finite-volume methods. All concentrations are defined at the cell centers.

During each time step of size k, the following steps occur

1. Fluid velocities with an updated Brinkman term are calculated using a second-order projection method.

2. The discretized coagulation equations for z_2, e_2, and f, are updated using Leveque's High-Resolution Advection Algorithm for advection, Alternating Direction Implicit method (ADI) for diffusion, and second-order Runge-Kutta (RK) for reactions to obtain a source rate of fibrin monomer, S_{10}.

3. For the equations for W, R, and V, Leveque's algorithm is used for advection in $\mathbf{x}$, ADI is used for diffusion in $\mathbf{x}$, and a weighted average of Lax-Wendroff and Beam Warming is used for advection in the dummy variable z in the W and V. Reaction terms are calculated using Forward Euler. The order in which these equations are solved is important.

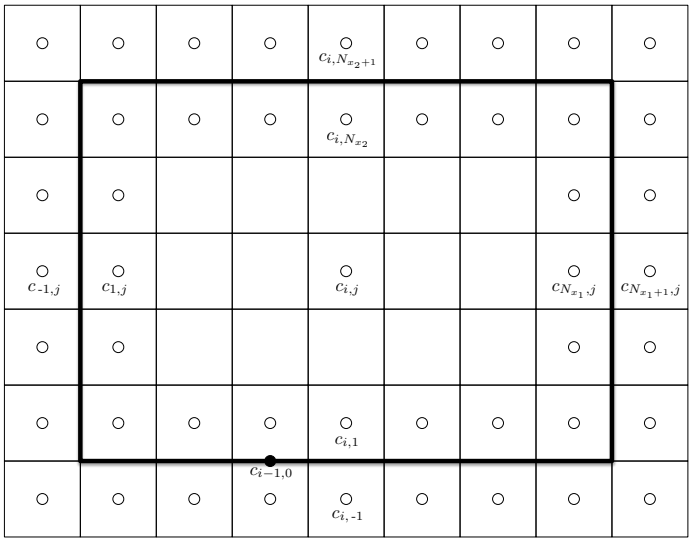

Figure 6.1: The computational mesh used for the numerical schemes described in this chapter. The bold line marks the boundary of the domain. Outside of the boundary there is one level of ghost cells. The value of c at the lower wall ($x_1 = 0$) is labeled as $c_{j-1,0}$.

(a) The advection in the z variable for W is calculated first using Lax-Wendroff and Beam Warming.

(b) W at $z = 1$ is not changed by advection in $\mathbf{x}$ or by diffusion. It can be calculated from (a) and using Forward Euler for reaction terms.

(c) Using W at $z = 1$, Leveque's Algorithm is used to calculate advection in $\mathbf{x}$ for $z < 1$. Then ADI is use to calculate diffusion in $\mathbf{x}$ for $z < 1$.

(d) With $R_g = -W|_{z=1}$, the above methods are used to update R. Then $R_s = R - R_g$.

(e) Finally, V is updated using the same methods as used for W.

4. The structure variables, θ_s and B_s, are calculated by integrating W and V using the trapezoid rule. Then θ can be calculated explicitly by applying a discrete advection and diffusion operator to θ_s and using Forward Euler for the reaction terms. Since $B_g = R_g$, B is calculated using simple addition, $B = B_s + B_g$.

5. The Brinkman term is updated as are ϕ_g, and the hindered diffusion and hindered advection terms from the hindered transport model.

6. Repeat until desired time is reached.

In the sections below, we describe the numerical methods used in more depth. We begin with the modified Navier-Stokes equations.

6.1 Fluid

We use finite differences and an exact projection method to find approximate solutions to equations 2.43-2.44. First, we solve a linear system to find an intermediate velocity value, $\mathbf{u}^*$, using the momentum equation. Then we solve a Poisson problem for the pressure and use it to correct $\mathbf{u}^*$ to $\mathbf{u}^{n+1}$ which is discretely divergence free.

We find $\mathbf{u}^*$ by applying finite difference methods to equation 2.43 without the pressure term.

$$\frac{\mathbf{u}^* - \mathbf{u}^n}{k} + \mathbf{a}^{n+1/2} = \mu\Delta^h\left(\frac{\mathbf{u}^* + \mathbf{u}^n}{2}\right) - \mu\alpha_1\mathbf{u}^* \tag{6.1}$$

The term $\mathbf{a}^{n+1/2}$ approximates to the advection term by,

$$\mathbf{a}^{n+1/2} = \frac{3}{2}\mathbf{a}^n - \frac{1}{2}\mathbf{a}^{n-1}. \tag{6.2}$$

The term Δ^h is the discrete 5-point Laplacian operator. In the Brinkman term, $\mathbf{u}^*$ is used instead of $\mathbf{u}^{\mathbf{n}}$ for numerical stability. Equation 6.1 is a linear system for $\mathbf{u}^*$. In order to

solve this system, we use the iterative method, Successive Overrelaxation (SOR). The value $\mathbf{u}^*$ does not satisfy $\nabla^h \cdot \mathbf{u}^* = 0$, where $\nabla^h \cdot$ is the discrete divergence operator defined in detail below.

Next, we take $\mathbf{u}^*$ to $\mathbf{u}^{n+1}$ using the pressure gradient. We discretize the remaining terms of the momentum equation and the incompressibility equation.

$$\begin{aligned} \frac{\mathbf{u}^{n+1} - \mathbf{u}^*}{k} &= -\nabla^h p & (6.3) \\ \nabla \cdot \mathbf{u}^{n+1} &= 0, & (6.4) \end{aligned}$$

Here ∇^h is the discrete gradient operator and is defined in detail below. Rearranging Equation 6.3, we see that $\mathbf{u}^{n+1}$ is a projection of $\mathbf{u}^*$ onto the divergence free velocity field. We apply the discrete divergence operator to both sides of Equation 6.3 and use Equation 6.4 to obtain an equation for p.

$$\Delta^h p = \frac{1}{k} \nabla^h \cdot \mathbf{u}^*. \tag{6.5}$$

This is a Poisson equation for p. A multigrid method is used to solve this equation. The multigrid method uses red-black Gauss-Seidel as the smoothing operator, full weighting as the restriction operator, and bilinear interpolations as the prolongation operator. Once we have obtained p, we compute $\mathbf{u}^{n+1}$ as

$$\mathbf{u}^{n+1} = \mathbf{u}^* + k \nabla^h p. \tag{6.6}$$

The discrete divergence operator takes a vector defined on the cell edges and returns a scalar located in the center of the cell. When applied to $\mathbf{u}^*$ in cell (i, j), the result is

$$\nabla^h \cdot \mathbf{u}^* = \frac{u^*_{i+\frac{1}{2},j} - u^*_{i-\frac{1}{2},j}}{h} + \frac{v^*_{i,j+\frac{1}{2}} - v^*_{i,j-\frac{1}{2}}}{h}. \tag{6.7}$$

The discrete gradient operator takes scalar values located in the cell centers and returns vectors located on cell edges. The first component of $\nabla^h p$ for cell (i, j), located on the right cell edge, is

$$\frac{p_{i+1,j} - p_{i,j}}{h}, \tag{6.8}$$

and the second component, located on the top cell edge, is

$$\frac{p_{i,j+1} - p_{i,j}}{h}. \tag{6.9}$$

6.2 Diffusion

We use the Peaceman-Rachford [31] version of the ADI method to model diffusion in our 2-D physical domain. Like Crank-Nicolson, ADI is a second order method; however, ADI is a 2-step method. In each step of ADI, one direction of diffusion is modeled explicitly while the other direction is modeled implicitly. The roles reverse in the successive step. This results in decoupled, tridiagonal solves in each step. The basic diffusion equation can be written as,

$$\frac{\partial c}{\partial t} = D\nabla^2 c. \tag{6.10}$$

We begin with treating diffusion in the x_2 direction implicitly and diffusion in the x_1 direction explicitly. The complexity of the nonlinear Robin condition in z_2 dictates this choice at the $x_2 = 0$ boundary. The steps used to obtain c^{n+1} from c^n are

$$(I - \frac{k}{2}D\nabla^2_{h,x_2})c^* = (I + \frac{k}{2}D\nabla^2_{h,x_1})c^n, \tag{6.11}$$

$$(I - \frac{k}{2}D\nabla^2_{h,x_1})c^{n+1} = (I + \frac{k}{2}D\nabla^2_{h,x_2})c^*. \tag{6.12}$$

Here $\nabla^2_{h,i}$ is the standard three-point stencil in the i direction. We modify Equations 6.11 - 6.12 to

$$(I - \frac{k}{2}D\nabla^2_{h,x_2})c^* = (I + \frac{k}{2}D\nabla^2_{h,x_1})c^n + k(\mathrm{Adv}_x + \mathrm{Adv}_z + \mathrm{Rxn}) \tag{6.13}$$

$$(I - \frac{k}{2}D\nabla^2_{h,x_1})c^{n+1} = (I + \frac{k}{2}D\nabla^2_{h,x_2})c^*. \tag{6.14}$$

Here Adv_x is the advection term in $\mathbf{x}$ calculated from Leveque's Algorithm, Adv_z is the advection term in z calculated using Lax-Wendroff and Beam-Warming, and Rxn is the reaction term treated with either Forward Euler or Runge-Kutta as noted in the algorthim list at the beginning of this chapter.

In order to solve Equations 6.13-6.14, we extend the discrete varible c to a larger domain that includes one level of ghost cells on all 4 edges. This is accomplished using the boundary conditions. Since the boundary itself is midway between cell-centers (-1, j) and (1, j), we set the ghost cell value $c_{\text{-}1,j}$ so that the average of $c_{1,j}$ and $c_{\text{-}1,j}$ is c^{up}, i.e. $c_{\text{-}1,j} = 2\,c^{up} - c_{1,j}$. For the top wall and downstream boundary, the homogenous Neumann boundary condition is discretized using centered differencing and used to fill in the appropriate ghost cells values,

$$c_{i,N_{x_2}+1} = c_{i,N_{x_2}} \tag{6.15}$$

$$c_{N_{x_1}+1,j} = c_{N_{x_1},j}. \tag{6.16}$$

For f and the gelation variables, the homogenous Neumann boundary conditions along the bottom wall is also discretized using center differencing and used to fill in the ghost cell values,

$$c_{i,\text{-}1} \;=\; c_{i,1}. \tag{6.17}$$

The nonlinear Robin boundary condition for z_2,

$$-D\frac{\partial z_2}{\partial x_2} = -\frac{\alpha z_2}{\beta + z_2}, \tag{6.18}$$

requires more work. For ease of notation, let $z_2(ih, jh, nk) = Z^n_{i,j}$ and $e_2(ih, jh, nk) = E^n_{i,j}$. Discretizing equation 6.18,

$$-D_z\left(\frac{Z^n_{i,1} - Z^n_{i,\text{-}1}}{h}\right) = -\frac{\alpha Z^n_{i,0}}{\beta + Z^{n-1}_{i,0}}. \tag{6.19}$$

The left side of Equation 6.19 involves center differencing about $x_2 = 0$. For right side, the numerator, $Z^n_{i,0}$ is approximated using quadratic interpolation (involving points $Z^n_{i,\text{-}1}, Z^n_{i,1}$, and $Z^n_{i,2}$) at the current time level. In the denominator, $Z_{i,0}$ is approximated using quadratic interpolation at the previous time step. After some algebraic manipulation, one can find an expression for $Z_{i,\text{-}1}$ as a function of values at interior grid points of Z. The boundary condition along the bottom wall for e_2 is the same as that for z_2 except for a sign change on the right hand side. Numerically, we maintain consistency by using the same approximate values for $Z_{i,0}$ in e_2 as in the boundary condition for z_2, namely

$$-D_z\left(\frac{E^n_{i,1} - E^n_{i,\text{-}1}}{h}\right) = \frac{\alpha Z^n_{i,0}}{\beta + Z^{n-1}_{i,0}}, \tag{6.20}$$

where $Z^n_{i,0}$ and $Z^{n-1}_{i,0}$ are as just described.

The equations for W and R, must be written in the form of the Equation 6.10 in order to use ADI. As a reminder for the reader, the evolution of W is described by

$$\frac{\partial W}{\partial t} = \nabla \cdot \left(D_c \nabla \left(W - zW\big|_{z=1}\right)\right) + \Delta t(\text{Adv}_x + \text{Adv}_z + \text{Rxn}). \tag{6.21}$$

Splitting the diffusion term,

$$\frac{\partial W}{\partial t} = \nabla \cdot (D_c \nabla W) - \nabla \cdot \left(D_c \nabla zW\big|_{z=1}\right) + ... \tag{6.22}$$

Let $W(ih, jh, kn, z_l) = W^n_{i,j,l}$, where $\{z_l\}$, $l = 0, 1, ..N_z$ are discrete grid points on the z-interval $[0, 1]$. By this stage in which we update W to account for diffusion in $\mathbf{x}$, we have already updated W to account for advection in z so W^{n+1}_{i,j,N_z} is known. We apply a five-point

discrete Laplacian, $\nabla^2_{5,h}$, to the average of W^{n+1}_{i,j,N_z} and W^n_{i,j,N_z}. Call this average, $W^{n+1/2}_{i,j,N_z}$. For W, the ADI method is modified to

$$\begin{aligned}(I - \frac{k}{2}D_c\nabla^2_{h,x_2})W^* &= (I + \frac{k}{2}D_c\nabla^2_{h,x_1})W^n - k\,D_c z\nabla^2_{5h}(W^{n+1/2}_{i,j,N_z}) \\ &+ k(\mathrm{ADV}_x + \ \mathrm{ADV}_z + \mathrm{Rxn}). \qquad (6.23)\\ (I - \frac{k}{2}D_c\nabla^2_{h,x_1})W^{n+1} &= (I + \frac{k}{2}D_c\nabla^2_{h,x_2})W^*. \qquad (6.24)\end{aligned}$$

The diffusion term for R is rewritten by making the substitution $R_s = R - R_g$,

$$\frac{\partial R(\mathbf{x},t)}{\partial t} = \nabla\cdot(D_c\nabla(R - R_g)) + k(\mathrm{ADV}_x + \mathrm{Rxn}). \qquad (6.25)$$

As for W, the ADI method for diffusion of R is modified to include $D_c\nabla^2 R_g$, discretized with a 5-point Laplacian on the right hand side of the first step.

$$\begin{aligned}(I - \frac{k}{2}D_c\nabla^2_{h,x_2})R^* &= (I + \frac{k}{2}D_c\nabla^2_{h,x_1})R^n - kD_c\nabla^2_{5h}R_g \qquad (6.26)\\ &+ k(\mathrm{Adv}_x + \mathrm{Adv}_z + \mathrm{Rxn})\\ (I - \frac{k}{2}D_c\nabla^2_{h,x_1})R^{n+1} &= (I + \frac{k}{2}D_c\nabla^2_{h,x_2})R^*. \qquad (6.27)\end{aligned}$$

In order to apply the 5-point Laplacian stencil over the whole domain, R_g must be extended to one level of ghost cells around the domain $\mathbf{x}$. Because R_g does not advect or diffuse, it does not have a boundary condition. Therefore, R_g is extrapolated to each ghost cell by fitting a polynomial to the first three interior points along the normal to the boundary.

Finally, the ghost cells values for R are filled in using the boundary conditions for R_s and R_g. R_s has homogenous Neumann boundary conditions along the top and bottom walls. As before, we approximate the normal derivatives using a centered difference at the boundary. The ghost cells for R must satisfy $R = R_g + R_s$ and are filled accordingly. The upstream boundary condition is $R = 0$. We set the ghost cell value, $R_{\text{-}1,j}$ so that the average of $R_{1,j}$ and $R_{\text{-}1,j}$ is identically zero.

The homogenous Neumann downstream boundary condition is discretized using center differencing and used to fill in the ghost cell values on the right boundary.

6.3 Advection in x

Advection in the $\mathbf{x}$ domain is handled using Leveque's conservative algorithm for advection [22]. This algorithm begins with the upwind method then offers a series of corrections

to increase the accuracy and stability of the solution. The algorithm is used on equations of the form

$$\frac{\partial c}{\partial t} + \nabla \cdot (\mathbf{u}c) = 0. \tag{6.28}$$

From the fluid solver, velocities are located at cell edges (unlike concentrations which are located at cell centers). This shown in Figure 6.2. Let u be the fluid velocity in the x_1-direction and v be the fluid velocity x_2-direction. We now calculate the flux into cell (i, j). Let $F_{i-1/2,j}$ and $F_{i+1/2,j}$ be the fluxes to the right across the left and right cell edges, respectively, of cell (i, j). Similarly, $G_{i-1/2,j}$ and $G_{i+1/2,j}$ are the upward fluxes across the bottom and top edges of the cell. Although LeVeque's algorithm can handle velocity components of either sign, for simplicity, we describe if for the case $u_{i\pm1/2,j} > 0$ and $v_{i,j\pm1/2} > 0$. To begin with, we apply the upwind method over all i, j,

$$F_{i-1/2,j} = u_{i-1/2,j}c_{i-1,j} \tag{6.29}$$

$$G_{i,j-1/2} = v_{i,j-1/2}c_{i,j-1}. \tag{6.30}$$

We can improve on the upwind fluxes by accounting for transverse propagation. The transverse propagation in the x_1 direction affects the flux through the top and bottom of the cell, and that in the x_2 direction affects the fluxes across the left and right cell edges.

$$G_{i,j-1/2} = G_{i,j-1/2} + \frac{1}{2}u_{i-1/2,j}v_{i-1/2,j}\left(c_{i,j} - c_{i-1,j}\right), \tag{6.31}$$

$$F_{i-1/2,j} = F_{i-1/2,j} + \frac{1}{2}u_{i,j-1/2}v_{i,j-1/2}\left(c_{i,j} - c_{i,j-1}\right). \tag{6.32}$$

Currently, as described this is a first-order method with higher accuracy than the upwind method alone. Equations 6.31-6.32 are further corrected using the Lax-Wendroff method with a flux-limiter. Lax-Wednroff is a second-order method but creates oscillations when there are steep gradients. Therefore, we use a flux-limiter, Φ.

$$F_{i-1/2,j} = F_{i-1/2,j} + \frac{1}{2}\left|u_{i-1/2,j}\right|\left(1 - \frac{k}{h}\left|u_{i-1/2,j}\right|\right)\left(c_{i,j} - c_{i-1,j}\right)\Phi_{1,(i,j)} \tag{6.33}$$

$$G_{i,j-1/2} = G_{i,j-1/2} + \frac{1}{2}\left|v_{i,j-1/2}\right|\left(1 - \frac{k}{h}\left|v_{i,j-1/2}\right|\right)\left(c_{i,j} - c_{i,j-1}\right)\Phi_{2,(i,j)}, \tag{6.34}$$

where $\Phi_{1,(i,j)} = \phi(\theta_{1,(i,j)})$ and $\Phi_{2,(i,j)} = \phi(\theta_{2,(i,j)})$. The function ϕ can be any for a number of flux-limiter methods including monotonized centered, superbee, or minmond. The value of $\theta_{1,(i,j)}$ and $\theta_{2,(i,j)}$ are each ratios of approximate first derivatives of c in the x_1 and x_2 directions using cells neighboring the i, j^{th} cell.

$$\theta_{1(i,j)} = \frac{c_I - c_{I-1}}{c_{i,j} - c_{i-1,j}}, \tag{6.35}$$

$$I = \begin{cases} i-1, j & \text{if } u_{i,j} > 0 \\ i+1, j & \text{if } u_{i,j} \leq 0. \end{cases} \tag{6.36}$$

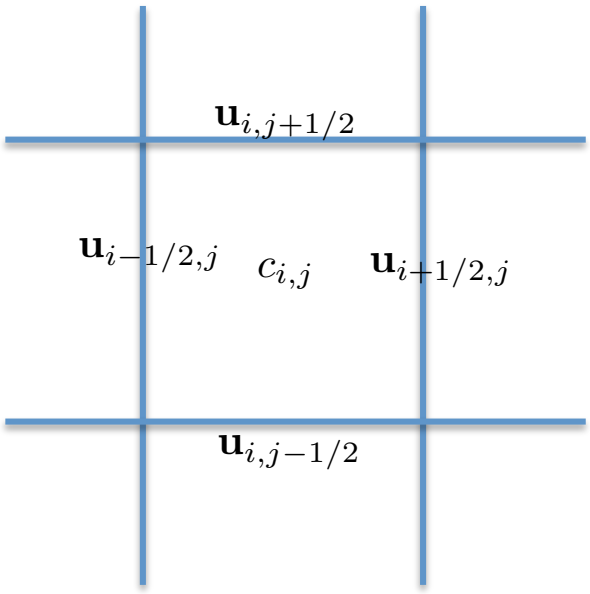

Figure 6.2: M.A.C. grid. Fluid velocities, $\mathbf{u}$, are located at cell edges and are used to calculate the flux of c into cell i, j. Concentrations, c, are located at cell centers.

The argument $\theta_{2,(i,j)}$ function of $\Phi_{2,(i,j)}$ is defined similarly but using differences in the x_2 direction. If the gradient is steep, $\theta = 0$ and equations 6.33 - 6.34 reduce to the upwind method. If the gradient is not steep, 6.33-6.34 is close to the Lax-Wendroff Method. Next, we add a correction to account for the transverse propagation of these second-order fluxes,

$$\begin{aligned} G_{i,j-1/2} &= G_{i,j-1/2} \qquad (6.37)\\ &+ \frac{k}{2h} v_{i-1/2,j} \left|u_{i-1/2,j}\right| \left(1 - \frac{k}{h}\left|u_{i-1/2,j}\right|\right) (c_{i,j} - c_{i-1,j})\, \Phi_{1,(i,j)},\\ G_{i-1,j+1/2} &= G_{i-1,j+1/2} \qquad (6.38)\\ &- \frac{k}{2h} v_{i-1/2,j} \left|u_{i-1/2,j}\right| \left(1 - \frac{k}{h}\left|u_{i-1/2,j}\right|\right) (c_{i,j} - c_{i-1,j})\, \Phi_{1,(i,j)},\\ F_{i-1/2,j} &= F_{i-1/2,j} \qquad (6.39)\\ &+ \frac{k}{2h} u_{i,j-1/2} \left|v_{i,j-1/2}\right| \left(1 - \frac{k}{h}\left|v_{i,j-1/2}\right|\right) (c_{i,j} - c_{i,j-1})\, \Phi_{2,(i,j)},\\ F_{i-1/2,j-1} &= F_{i-1/2,j-1} \qquad (6.40)\\ &- \frac{k}{2h} u_{i,j-1/2} \left|v_{i,j-1/2}\right| \left(1 - \frac{k}{h}\left|v_{i,j-1/2}\right|\right) (c_{i,j} - c_{i,j-1})\, \Phi_{2,(i,j)}. \end{aligned}$$

Finally, $c_{i,j}^{n+1}$ is calculated as the sum of the fluxes.

$$c_{i,j}^{n+1} = c_{i,j}^{n} - \frac{k}{h}\left(F_{i+\frac{1}{2},j} - F_{i-\frac{1}{2},j} + G_{i,j+\frac{1}{2}} - G_{i,j-\frac{1}{2}}\right) \qquad (6.41)$$

And Adv_x is

$$\mathrm{Adv}_x = -\frac{1}{h}\left(F_{i+\frac{1}{2},j} - F_{i-\frac{1}{2},j} + G_{i,j+\frac{1}{2}} - G_{i,j-\frac{1}{2}}\right) \qquad (6.42)$$

6.4 Advection in z

The equations for W and V each contain a term that describes advection in z. We know from similar models [42] that W experiences a singularity ($W_z|_{z=1} \to \infty$) at $z = 1$ at the time t_g when a gel first appears. We refer to t_g as gel time. W is always smooth for $0 \le z < 1$ and W is smooth at $z = 1$ except at $t = t_g$. The advection velocities in z for W and V are positive for information propagating from left to right. Therefore, we use a modified Beam-Warming method which is a one-sided, second-order method to handle the z-advection [23]. Given an equation of the the form,

$$\frac{\partial c}{\partial t} + f(c)_z = 0, \qquad (6.43)$$

Here $f(c)$ is some functional dependence on c. The modified Beam-Warming method is

$$\begin{aligned} c_i^{n+1} &= c_i^n - f(c)_z k \qquad (6.44)\\ &= c_i^n - \frac{k}{2h}\left(3f(c)_i^n - 4f(c)_{i-1}^n + f(c)_{i-2}^n\right), \qquad (6.45) \end{aligned}$$

if $f(c)_z$ is approximated with a one-sided second order finite-difference. Due to the definition of W and V, they are zero at $z = 0$ for all time. The first interior point value, c_1, is found using first-order upwinding.

Because R_g is defined as W at $z = 1$, it is important to be accurate at this point. We achieve this level of accuracy, while keeping our computational cost low, by using a nonuniform discretization of z (Figure 6.3). The nonuniform discretization modifies equations 6.45 by

$$c_i^{n+1} = c_i^n - k\left(bw_1\, f(c)_i^n - bw_2\, f(c)_{i-1}^n + bw_3\, f(c)_{i-2}^n\right). \tag{6.46}$$

Here $bw_3 = \frac{h_i}{h_{i-1}(h_i+h_{i-1})}$, $bw_2 = -\frac{h_i+h_{i-1}}{h_{i-1}h_i}$, and $bw_1 = -(bw_3 + bw_1)$. Let $Adv_{BW,i} = bw_1\, f(c)_i^n - bw_2\, f(c)_{i-1}^n + bw_3\, f(c)_{i-2}^n$.

Using the above method, W and V at $z = h_1$, is found using only a first-order method. However, we are interested in integrating W and V in z from $[0, 1]$. In order to obtain a more accurate value of V, W, we use a linear combination of Lax-Wendroff and Beam-Warming. Lax-Wendroff is a two-sided, second-order method that models advection [23]. For an equation of the form 6.43 and for a nonuniform discretization,

$$\begin{aligned} c_i^{n+1} &= c_i^n - \frac{k}{h_i + h_{i+1}}\left(f(c_{i-1}^n) + f(c_{i+1}^n)\right) \\ &+ \frac{k^2}{h_{i+1}+h_i}\left\{\frac{1}{h_{i+1}} f\left(\frac{c_i^n + c_{i+1}^n}{2}\right)\left(f(c_{i+1}^n) - f(c_i^n)\right)\right\} \\ &- \frac{k^2}{h_{i+1}+h_i}\left\{\frac{1}{h_i} f\left(\frac{c_{i-1}^n + c_i^n}{2}\right)\left(f(c_i^n) - f(c_{i-1}^n)\right)\right\}. \end{aligned} \tag{6.47}$$

Let

$$\begin{aligned} Adv_{LW,i} &= -\frac{1}{h_i + h_{i+1}}\left(f(c_{i-1}^n) + f(c_{i+1}^n)\right) \\ &+ \frac{k}{h_{i+1}+h_i}\left\{\frac{1}{h_{i+1}} f\left(\frac{c_i^n + c_{i+1}^n}{2}\right)\left(f(c_{i+1}^n) - f(c_i^n)\right)\right\} \\ &- \frac{k^2}{h_{i+1}+h_i}\left\{\frac{1}{h_i} f\left(\frac{c_{i-1}^n + c_i^n}{2}\right)\left(f(c_i^n) - f(c_{i-1}^n)\right)\right\}. \end{aligned} \tag{6.48}$$

We then define Adv_z by

$$\begin{aligned} Adv_{z,i} &= Adv_{LW,i}(1 - 0.5\tanh(20(z_i - 0.25)) - 0.5) \\ &+ Adv_{BW,i}(0.5\tanh(20(z_i - 0.25)) + 0.5). \end{aligned} \tag{6.49}$$

For values of z near 0, this advection term is essentially that from the Lax-Wendroff Method. For values of z near 1, is is essentially that from the Beam-Warming Method. For intermediate values of z, it is a weight average of the Lax-Wendroff and Beam Warming advection terms.

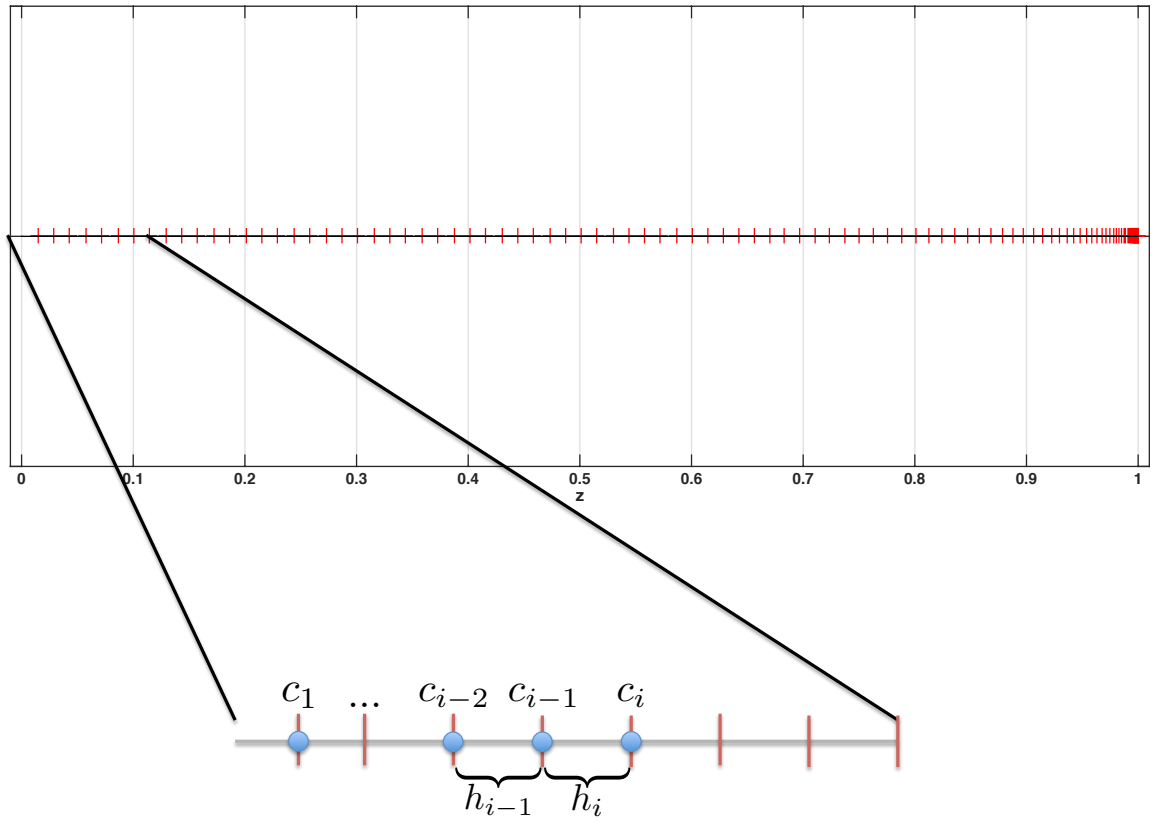

Figure 6.3: Nonuniform z-grid for beam-warming method. The Beam-Warming method is a one-sided method. In order to achieve a more accurate computation of R_g, the z dimension has nonuniform spacing with point space more closely near $z = 1$. This is an example of the nonuniform spacing of $z \in [0, 1]$ with the number of points, $N_z = 100$.

6.5 Reactions

A secord-order, two-step Runge-Kutta method is used to treat the specified reactions [23]. We illustrate the method on the sample equation,

$$\frac{\partial c(x_1, x_2)}{\partial t} = \mathrm{Rxn}\left(c\left(x_1, x_2\right)\right), \tag{6.50}$$

where $\mathrm{Rxn}\left(c\left(x_1, x_2\right)\right)$ is a function of reaction terms that involve only quantities in (x_1, x_2). Beginning at time level n,we advance c^n to c^{n+1} using the following method,

$$c^* = c^n + \frac{1}{2} k\, \mathrm{Rxn}(c^n) \tag{6.51}$$

$$c^{n+1} = c^n + k\, \mathrm{Rxn}(c^*). \tag{6.52}$$

CHAPTER 7

CONCLUSION

In this dissertation, we present a two-dimensional model of fibrin polymerization and gelation in flow with feedback on the fluid. The model includes a spatial-temporal source of fibrin monomers from a simplified coagulation model and a polymerization process based on the Branching Model [11]. The polymerization submodel begins with a doubly-infinite set of PDEs that describes the transport of oligomers and condensation reactions between fibrin oligomers. Through the use of a generating function and a change of variables, we are able to reduce the system to two PDEs (W and R). It is necessary to add two dummy variables in order to perform this reduction, one of which we are able to take as a constant value. We include three other PDEs, V, B, and θ, and three algebraic expressions that enables us to track the branch point density and fibrin mass density in the gel (as well as concentrations in the solvent). Branch point density and fibrin mass density are used to calculate the gel's structural properties which, in turn, provide feedback on the fluid through a Brinkmann term.

Through numerical simulation with and without fluid flow, we are able to examine the process of fibrin clot formation. Most importantly, we see that fibrin gel cannot form along a flat wall. It is essential to have a region protected from flow for clots to form. Biologically, this protected region could be from small platelet aggregates, which are necessary for thrombin production, or other cells that bind to the blood vessel wall. We add an area upstream of the injury that has low permeability which we call a "bump" to simulate clot growth in flow.

We find that the branch point density, fibrin mass density, and structural properties of a clot are dependent on several conditions during gelation, one of which is the source rate of fibrin monomers. Clots formed with fluid velocity identically zero have three distinct areas. Near the wall, there is an inner core with the smallest fibers and smallest pores that is a result of a high initial source rate. Just outside of the inner core, there is a shell of medium fiber diameters and pores that results from the depletion of fibrinogen and prothrombin at the wall. Outside of the shell, there is a small area of fibers that have just become gel. In

this area, there are large pores and medium fiber diameters. In flow, the fluid dynamics affect the distribution of the fibrin monomer source rate. By adding an area with a high brinkman coefficient, we create a region over the injury zone where the Péclet number is less than one. This region is larger for low shear rates. For all shear rates attempted, there is enough fibrin monomer accumulation that a gel can form over the injury zone. Within a single clot made in flow, the fiber diameter and pore sizes have little variability.

We find that the rate of thrombin production, α, affects initial thrombin production but does not affect the width or height of the resultant clot. Without flow, a high thrombin production rate causes a smaller fiber diameter near the vessel wall than a smaller rate. However, it has little influence on the fiber diameters away from the wall because the production of thrombin becomes diffusion limited. In flow, we change the thrombin production rate by several orders of magnitude and see only a small variation in fiber diameter.

The rate of branch point formation has a significant effect on both the clotting time and the resulting clot structure. Gels formed with a larger k_b, grow faster, have smaller fiber diameters, and have smaller pores. We also show that the biological upstream fibrinogen concentration is necessary for normal clotting. When the upstream fibrinogen concentration was decreased by a factor of two, clots took significantly longer to initiate. When the upstream fibrinogen concentration was decreased by a factor of 10, there was no clot formation within 2000 s, with or without flow. There must be a significant accumulation of branch points in order for gelation to occur.

We modify the model in two ways. We simulate thrombin production on platelet aggregates that are located in the fluid. We show that several different distributions of platelet aggregates provide the necessary region protected from flow for fibrin gelation to occur. We also modify the model to include more realistic transport dynamics. Realistically, as the gel accumulates, the diffusivity of proteins decrease so we include a coefficient that hinders diffusion of proteins as a function of gel volume fraction. Also, the drag on proteins as they advect past gel increases with increasing gel volume fraction so we include a coefficient to hinder the advection flux of proteins in relation to gel volume fraction. We also include a third component to the hindered transport model which creates a velocity that moves proteins out of areas with high gel volume fraction and into areas with low volume fraction.

While this dissertation studies the process of fibrin polymerization in flow, it does not provide a complete understanding of the complex interplay between coagulation, fibrin gelation, and fluid dynamics. Several extensions and future works have previously been

mentioned in this paper including further understanding of the hindered transport model, exploring the dynamics necessary to include the lateral aggregation of protofibrils, and possibly a completely different type of model to study fibrin orientation in flow.

The framework for at least one possible extension was laid out in Fogelson et al. 2015 [12]. Physically, each k-mer has a diffusivity that is related its size and structure. In the models described in this dissertation, all oligomers have the same diffusivity. Fogelson et al. show it is possible to include any finite number of oligomers diffusing with different diffusivities. However, in this model framework, for each additional oligomer diffusion coefficient included, a PDE for the respective k-mer must be added to the system and the diffusion coefficients for the variables in the current model become more complicated. It is more realistic to include two different diffusivities: monomers maintain the same diffusivity as fibrinogen and larger oligomers have a smaller diffusivity or are stationary.

In the author's opinion, the most obvious and necessary extension to this work is to couple the fibrin polymerization model with a model for coagulation and platelet aggregation. Both fibrin and platelets are primarily components of a thrombus. Platelets play an important spatial and temporal role in thrombin production that is essential for fibrin polymerization. Fibrinogen is also a necessary component of platelet aggregation. Fibrinogen connects two platelets by binding to αIIbβ3 integrins receptors located on the membrane of platelets [3]. Fibrin gel also provides necessary structural support that prevents the thrombus from embolizing. The fibrin polymerization model can be combined with a two-dimensional model of the coagulation cascade and platelet aggregation such as [21]. As platelets aggregate, they hinder the flow around the injury zone. With sufficient hindrance on the fluid flow and thrombin production, fibrin polymerization can occur.

APPENDIX A

FIBER DIAMETER AND PORE SIZE

From the model described in Chapter 2, we are able to track branch point density and fibrin mass density. We use a geometric argument to find a mathematical relationship between these densities and structural properties of the gel (i.e., pore size and fiber diameter). The reader should imagine a 2-D domain filled with fibers that are connected by branch points. If all the fibers are of equal length and equally spaced apart, the domain would be tessellated with hexagon where branch points are the vertices and fibers are the edges, shown in Figure A.1.

We focus on the area around a single branch point denoted by a green triangle in Figure A.2. From the area of the triangle, we calculate a length scale. Let L_t be the scale of the triangle, then

$$L_t = \frac{3^{1/4}}{2}\left(P + 2r\right). \tag{A.1}$$

Then we can calculate the branch point concentration, C_b, is

$$C_b = \frac{1}{L_t^3}. \tag{A.2}$$

This quantity must equal the branch point density from the model (once converted into the same units).

$$B_g = \frac{1}{N_a L_t^3}. \tag{A.3}$$

Here N_a is Avogadro's number. The area of fiber, A_f, in the green triangle is approximately,

$$A_f = 3(P + a)a. \tag{A.4}$$

Assuming the fibers are cylinders, the volume fraction of fibers is Φ_g

$$\phi_g = \frac{3\pi(P + a)a^2}{L_t^3} \tag{A.5}$$

We can find the volume fraction of fibers in the model from the fiber mass density,

$$\phi_g = N_a V_f \theta_g. \tag{A.6}$$

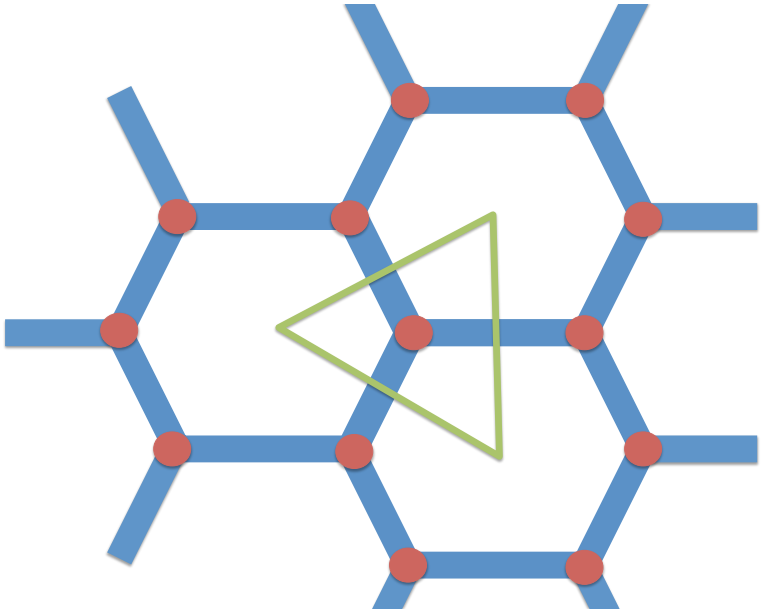

Figure A.1: Idealized branch point and fiber networks. Branch points represented by red dots. Fibers are blue lines.

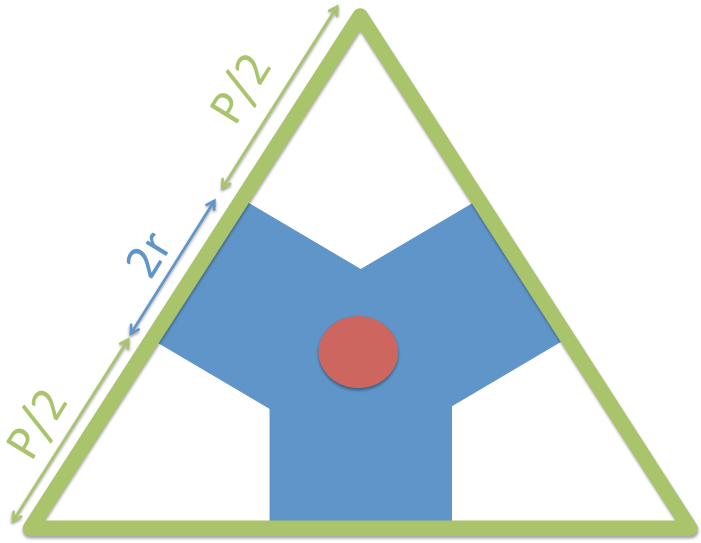

Figure A.2: Area around a single branch point. The length of the pore is P, the radius of a fiber is r.

Here $V_f = 4.2 \times 10^{-19}\, cm^3$ is the volume of a single fibrin monomer. We are left with the following systems of equations,

$$B_g = \frac{1}{N_a L_t^3} \tag{A.7}$$

$$N_a V_f \theta_g = \frac{3\pi(P+a)a^2}{Lt^3}. \tag{A.8}$$

We solve (A.7)-(A.8) for P and a and find the pore size and fiber diameter for each point in the domain,

$$P = \frac{F_B(B_g)}{1 + F_\phi(\phi_g)} \tag{A.9}$$

$$a = F_\phi(\phi_g) P. \tag{A.10}$$

Here $F_B(B_g) = \frac{2}{3^{1/4}(N_a B_g)^{1/3}}$, $F_\phi(\phi_g) = -\frac{3\phi_g + 3^{7/8}\sqrt{\pi\phi_g}}{-3^{3/4}\pi + 3\phi_g}$.

APPENDIX B

MODEL PARAMETERS

Table B.1: Domain parameters.

Parameter	Value
L_{x_1}	400 μm
L_{x_2}	100 μm
L_1	160 μm
L_2	240 μm

Table B.2: Coagulation parameters. a) The cleavage rates of prothrombin to thrombin were tuned to be within ranges that match from [29].
b) [17], [19]. c) [16]. d)[33]. e) [2]. f)[17].

Parameter	Value	Reference
Z^{up}	$1\,\mu$M	
F^{up}	$10\,\mu$M	
α	$1 \times 10^{-5}\, cm\, \mu$M/s	a
β	$5 \times 10^{-6}\,\mu$M	a
k_{at}	$0.1\, s^{-1}$	b
k_f	$100\, s^{-1}$	c
k_{fs}	$10\,\mu$M	d
D_z	1×10^{-7} cm^2/s	e
D_f	1×10^{-7} cm^2/s	f

Table B.3: Gelation parameters. Fibrin monomer binding $6 \times 10^{-1} - 1\mu M^{-1}s^{-1}$ [15], [39], [24]

Parameter	Value
k_l	$1\,\mu$M^{-1}s^{-1}
k_b	$10\,\mu$M^{-2}s^{-1}
D_c	1×10^{-7} cm^2/s

Table B.4: Fluid parameters.

Parameter	Value
ρ	1 g/cm^3
μ	.04 P

Table B.5: Alternative model for thrombin production parameters.[19]

Parameter	Value
k_{on}	$1 \times 10^8\, M^{-1} s^{-1}$
k_{off}	$5.9\, s^{-1}$
k_{cat}	$50\, s^{-1}$
R_o	$50\, nM$

APPENDIX C

HINDERED TRANSPORT EQUATIONS

The following equations are used to describe fibrin polymerization and gelation with hindered advection and hindered diffusion. The term $H_{u,i}$ is the hindrance due to drag between gel and proteins in the fluid. The term $H_{d,i}$ describes how much diffusion is hindered due to the presence of gel, and $\mathbf{u}_{vol,i}$ describes the transport of proteins out of a volume due to occupation by gel. Here $i \in \{z, f, c\}$. The exact form of the hindrance terms are described in Chapter 5. The boundary conditions along the top and bottom wall contain the x_2 component of $\mathbf{u}_{vol,i}$ which is denoted by $v_{vol,i}$.

C.1 Coagulation Proteins

$$\frac{\partial z_2}{\partial t} + \nabla \cdot (H_{u,z}\mathbf{u} z_2) + \bigtriangledown \cdot (D_z \mathbf{u}_{vol,z} z_2) = \nabla \cdot (H_{d,z} D_z \nabla z_2) \tag{C.1}$$

$$\frac{\partial e_2}{\partial t} + \nabla \cdot (H_{u,z}\mathbf{u} e_2) + \bigtriangledown \cdot (D_z \mathbf{u}_{vol,z} e_2) = \nabla \cdot (H_{d,z} D_z \nabla e_2) - k_{at} e_2 \tag{C.2}$$

$$\frac{\partial f}{\partial t} + \nabla \cdot (H_{u,f}\mathbf{u} f) + \bigtriangledown \cdot (D_f \mathbf{u}_{vol,f} f) = \nabla \cdot (H_{d,f} D_f \nabla f) - \frac{k_f e_2 f}{\phi_f k_{fs} + f}. \tag{C.3}$$

With the following boundary condition:
For z_2,

$$z_2(0, x_2, t) = z_2^{up}, \tag{C.4}$$

$$\frac{\partial z_2(L_{x_1}, x_2, t)}{\partial x_1} = 0, \tag{C.5}$$

$$-D_z \frac{\partial z_2(x_1, L_{x_2}, t)}{\partial x_2} = -\frac{D_z v_{vol,z}}{H_{d,z}} z_2, \tag{C.6}$$

$$-D_z \frac{\partial z_2(x_1, 0, t)}{\partial x_2} = \begin{cases} -\frac{D_z v_{vol,z}}{H_{d,z}} z_2, & \text{for } x_1 < L_1, x_1 > L_2 \\ -\left(\frac{\alpha}{H_{d,z}\left(\phi_f \beta + z_2\right)} + \frac{D_z v_{vol,z}}{H_{d,z}} \right) z_2, & \text{for } L_1 \leq x_1 \leq L_2. \end{cases} \tag{C.7}$$

For e_2,

$$
\begin{aligned}
e_2(0, x_2, t) &= 0 && \text{(C.8)}\\
\frac{\partial e_2(L_{x_1}, x_2, t)}{\partial x_1} &= 0, && \text{(C.9)}\\
-D_z \frac{\partial e_2(x_1, L_{x_2}, t)}{\partial x_2} &= -\frac{D_z v_{vol,z}}{H_{d,z}} e_2, && \text{(C.10)}\\
-D_z \frac{\partial e_2(x_1, 0, t)}{\partial x_2} &= \begin{cases} -\frac{D_z v_{vol,z}}{H_{d,z}} e_2, & \text{for } x_1 < L_1, x_1 > L_2 \\ \frac{\alpha z_2}{H_{d,z}\left(\phi_f \beta + z_2\right)} - \frac{D_z v_{vol,z}}{H_{d,z}} e_2, & \text{for } L_1 \le x_1 \le L_2. \end{cases} && \text{(C.11)}
\end{aligned}
$$

For f,

$$
\begin{aligned}
f(0, x_2, t) &= f^{up}, && \text{(C.12)}\\
\frac{\partial f(L_{x_1}, x_2, t)}{\partial x_1} &= 0, && \text{(C.13)}\\
-D_f \frac{\partial f(x_1, L_{x_2}, t)}{\partial x_2} &= -\frac{D_f v_{vol,f}}{H_{d,f}} f, && \text{(C.14)}\\
-D_f \frac{\partial f(x_1, 0, t)}{\partial x_2} &= -\frac{D_f v_{vol,f}}{H_{d,f}} f.
\end{aligned}
$$

Let $\tilde{S}_{1,0} = \frac{k_f e_2 f}{\phi_f k_{fs} + f}$.

C.1.1 Gelation Variables

For R,

$$
\begin{aligned}
\frac{\partial R(\mathbf{x}, t)}{\partial t} &+ \nabla \cdot (H_{u,c} \mathbf{u} R_s) + \bigtriangledown \cdot (D_c \mathbf{u}_{vol,c} R_s) && \text{(C.15)}\\
&= \nabla \cdot (H_{d,c} D_c \nabla R_s) - \frac{k_l}{\phi_f}\left(R^2 - R_g^2\right) - \frac{k_b}{2\phi_f^2}\left(R^3 - \left(3R_s R_g^2 + R_g^3\right)\right) + 2\tilde{S}_{10}
\end{aligned}
$$

Boundary Conditions for R,

$$
\begin{aligned}
R(0, x_2, t) &= 0, && \text{(C.16)}\\
\frac{\partial R(L_{x_1}, x_2, t)}{\partial x_1} &= 0, && \text{(C.17)}\\
-D_c \frac{\partial R(x_1, L_{x_2}, t)}{\partial x_2} &= -D_c \frac{\partial R_g}{\partial x_2} - \frac{D_c v_{vol,c}}{H_{d,c}}\left(R - R_g\right), && \text{(C.18)}\\
-D_c \frac{\partial R(x_1, 0, t)}{\partial x_2} &= -D_c \frac{\partial R_g}{\partial x_2} - \frac{D_c v_{vol,c}}{H_{d,c}}\left(R - R_g\right), && \text{(C.19)}
\end{aligned}
$$

For W,

$$\begin{aligned}
\frac{\partial W}{\partial t} &+ \bigtriangledown \cdot \left(H_{u,c}\mathbf{u}\left(W - zW\big|_{z=1}\right)\right) + \bigtriangledown \cdot \left(D_c\mathbf{u}_{vol,c}\left(W - zW\big|_{z=1}\right)\right) \qquad \text{(C.20)}\\
&= \bigtriangledown \cdot \left(H_{d,c}D_c \bigtriangledown \left(W - zW\big|_{z=1}\right)\right)\\
&+ \left\{\frac{k_l}{2\phi_f}W^2 + \frac{k_b}{2\phi_f^2}\left(\frac{1}{3}W^3 + zW^2R + z^2R^2W\right) - \frac{k_b}{2\phi_f^2}z(R^2 - R_g^2)(W + zR)\right\}_z\\
&- \frac{k_l}{\phi_f}zR_g^2 - \frac{k_b}{2\phi_f^2}\left(-zR^3 + 3zR_sR_g^2 + zRg^3\right) + \frac{k_b}{2\phi_f^2}z^2R^3
\end{aligned}$$

Boundary Conditions for W,

$$\begin{aligned}
W(0, x_2, t, z) &= 0, \qquad \text{(C.21)}\\
\frac{\partial W(L_{x_1}, x_2, t, z)}{\partial x_1} &= 0, \qquad \text{(C.22)}\\
-D_c\frac{\partial W(x_1, 0, t, z)}{\partial x_2} &= D_cz\frac{\partial R_g}{\partial x_2} - \frac{D_cv_{vol,c}}{H_{d,c}}\left(W - zW\big|_{z=1}\right) \qquad \text{(C.23)}\\
-D_c\frac{\partial W(x_1, L_{x_2}, t, z)}{\partial x_2} &= D_cz\frac{\partial R_g}{\partial x_2} - \frac{D_cv_{vol,c}}{H_{d,c}}\left(W - zW\big|_{z=1}\right) \qquad \text{(C.24)}\\
W(t, x, y, 0) &= 0. \qquad \text{(C.25)}
\end{aligned}$$

For V,

$$\begin{aligned}
\frac{\partial V}{\partial t} &+ \bigtriangledown \cdot (H_{u,c}\mathbf{u}V) + \bigtriangledown \cdot D_c\mathbf{u}_{vol,c}V \qquad \text{(C.26)}\\
&= \bigtriangledown \cdot (H_{d,c}D_c \bigtriangledown V)\\
&+ \left\{\left(\frac{k_l}{\phi_f}W + \frac{k_b}{2\phi_f^2}(W + zR)^2 - \frac{k_b}{2\phi_f^2}z(R^2 - \chi R_g^2)\right)V\right\}_z\\
&- \frac{k_b}{\phi_f^2}\left\{(W + zR)^2(W_z + R)\right\} + 2zS_{10}.
\end{aligned}$$

Boundary Conditions for V,

$$\begin{aligned}
V(0, x_2, t, z) &= 0 \qquad \text{(C.27)}\\
\frac{\partial V(L_{x_1}, x_2, t, z)}{\partial x_1} &= 0 \qquad \text{(C.28)}\\
-D_c\frac{\partial V(x_1, 0, t, z)}{\partial x_2} &= -\frac{D_cv_{vol,c}}{H_{d,c}}V \qquad \text{(C.29)}\\
-D_c\frac{\partial V(x_1, L_{x_2}, t, z)}{\partial x_2} &= -\frac{D_cv_{vol,c}}{H_{d,c}}V \qquad \text{(C.30)}\\
V(x_1, x_2, t, 0) &= 0. \qquad \text{(C.31)}\\
& \qquad \text{(C.32)}
\end{aligned}$$

C.1.2 Structural Quantities

For θ,

$$\begin{aligned} \frac{\partial \theta}{\partial t} &+ \bigtriangledown \cdot (H_{u,c}\mathbf{u}\theta_s) + \bigtriangledown \cdot D_c \mathbf{u}_{vol,c}\theta_s \\ &= \bigtriangledown \cdot (H_{d,c} D_c \bigtriangledown \theta_s) + \tilde{S}_{10} \end{aligned} \tag{C.33}$$

Boundary Conditions for θ,

$$\theta(t,0,y) = 0 \tag{C.34}$$

$$\frac{\partial \theta(L_{x_1}, x_2, t)}{\partial x_1} = 0 \tag{C.35}$$

$$-D_c \frac{\partial \theta(x_1, 0, t)}{\partial x_2} = -D_c \frac{\partial \theta_g}{\partial x_2} - \frac{D_c v_{vol,c}}{H_{d,c}} (\theta - \theta_g) \tag{C.36}$$

$$-D_c \frac{\partial \theta(x_1, L_{x_2}, t)}{\partial x_2} = -D_c \frac{\partial \theta_g}{\partial x_2} - \frac{D_c v_{vol,c}}{H_{d,c}} (\theta - \theta_g) \tag{C.37}$$

$$\tag{C.38}$$

For B,

$$\begin{aligned} \frac{\partial B}{\partial t} &+ \bigtriangledown \cdot (H_{u,c}\mathbf{u}B_s) + \bigtriangledown \cdot B_s D_c \mathbf{u}_{vol,c} \\ &= \bigtriangledown \cdot (H_{d,c} D_c \bigtriangledown B_s) + \frac{k_b}{6\phi_f^2} \left(R^3 - \left(3R_s R_g^2 + R_g^3\right)\right) \end{aligned} \tag{C.39}$$

Boundary Conditions for B,

$$B(t,0,y) = 0 \tag{C.40}$$

$$\frac{\partial B(L_{x_1}, x_2, t)}{\partial x_1} = 0 \tag{C.41}$$

$$-D_c \frac{\partial B(x_1, 0, t)}{\partial x_2} = -D_c \frac{\partial B_g}{\partial x_2} - \frac{D_c v_{vol,c}}{H_{d,c}} (B - B_g) \tag{C.42}$$

$$-D_c \frac{\partial B(x_1, L_{x_2}, t)}{\partial x_2} = -D_c \frac{\partial B_g}{\partial x_2} - \frac{D_c v_{vol,c}}{H_{d,c}} (B - B_g) \tag{C.43}$$

REFERENCES

[1] S. S. Acharya and D. M. Dimichele, *Rare inherited disorders of fibrinogen*, Haemophilia, 14 (2008), pp. 1151–1158.

[2] N. Bark, Z. Földes-Papp, and R. Rigler, *The incipient stage in thrombin-induced fibrin polymerization detected by fcs at the single molecule level*, Biochemical and Biophysical Research Communications, 260 (1999), pp. 35–41.

[3] J. S. Bennett, *Structure and function of the platelet integrin αiib β3*, The Journal of Clinical Investigation, 115 (2005), pp. 3363–3369.

[4] L. F. Brass, M. Ahuja, E. Belmonte, S. Pizarro, A. Tarver, and J. A. Hoxie, *The human platelet thrombin receptor*, Annals of the New York Academy of Sciences, 714 (1994), pp. 1–12.

[5] R. A. Campbell, M. M. Aleman, L. D. Gray, M. R. Falvo, and A. S. Wolberg, *Flow profoundly influences fibrin network structure: Implications for fibrin formation and clot stability in haemostasis*, Thrombosis and Haemostasis, 104 (2010), pp. 1281–1284.

[6] I. N. Chernysh, C. Nagaswami, and J. W. Weisel, *Visualization and identification of the structures formed during early stages of fibrin polymerization*, Blood, 117 (2011), pp. 4609–4614.

[7] I. N. Chernysh and J. W. Weisel, *Dynamic imaging of fibrin network formation correlated with other measures of polymerization*, Blood, 111 (2008), pp. 4854–4861.

[8] S. J. Everse, G. Spraggon, L. Veerapandian, M. Riley, and R. F. Doolittle, *Crystal structure of fragment doubled from human fibrin with two different bound ligands*, Biochemistry, 37 (1998), pp. 8637–8642.

[9] A. L. Fogelson, *Hindered diffusion*, unpublished, (2014).

[10] A. L. Fogelson, *Notes on protein reactions in multiphase mixtures*, unpublished, (2015).

[11] A. L. Fogelson and J. P. Keener, *Toward an understanding of fibrin branching structure*, Physical Review E, 81 (2010), p. 051922.

[12] A. L. Fogelson and J. P. Keener *A framework for exploring the post-gelation behavior of Ziff and Stell's polymerization models*, SIAM J. Applied Mathematics, 75 (2015), pp. 1346–1368.

[13] K. C. Gersh, K. E. Edmondson, and J. W. Weisel, *Flow rate and fibrin fiber alignment*, Thrombosis and Haemostasis, 8 (2010), pp. 2826–2828.

[14] R. D. Guy, A. L. Fogelson, and J. P. Keener, *Fibrin gel formation in a shear flow*, Mathematical Medicine and Biology, 24 (2007), pp. 111–130.

[15] R. R. Hantgan and J. Hermans, *Assembly of fibrin*, Journal of Biological Chemistry, 254 (1979), pp. 11272–11281.

[16] D. Higgins, S. D. Lewis, and J. Shafer, *Steady state kinetic parameters for the thrombin-catalyzed conversion of human fibrinogen to fibrin*, Journal of Biological Chemistry, 258 (1983), pp. 9276–9282.

[17] J. A. Hubbell and L. V. McIntire, *Platelet active concentration profiles near growing thrombi. a mathematical consideration*, Biophysical Journal, 50 (1986), pp. 937–945.

[18] G. W. Jackson and D. F. James, *The permeability of fibrous porous media*, The Canadian Journal of Chemical Engineering, 64 (1986), pp. 364–374.

[19] A. L. Kuharsky and A. L. Fogelson, *Surface-mediated control of blood coagulation: the role of binding site densities and platelet deposition*, Biophysical Journal, 80 (2001), pp. 1050–1074.

[20] U. Larsson, B. Blombäck, and R. Rigler, *Fibrinogen and the early stages of polymerization to fibrin as studied by dynamic laser light scattering*, Biochimica et Biophysica Acta (BBA)-Protein Structure and Molecular Enzymology, 915 (1987), pp. 172–179.

[21] K. Leiderman and A. L. Fogelson, *The influence of hindered transport on the development of platelet thrombi under flow*, Bulletin of Mathematical Biology, (2012), pp. 1–29.

[22] R. J. LeVeque, *High-resolution convservative algorithms for advection in incompressible flow*, SIAM J. Numer. Anal., 33 (1996), pp. 627–665.

[23] R. J. LeVeque, *Finite Difference Methods for Ordinary and Partial Differentail Equations: Steady-state and Time-Dependent Problems*, SIAM, Philadelphia, PA 19104, 2007.

[24] S. D. Lewis, P. Shields, and J. Shafer, *Characterization of the kinetic pathway for liberation of fibrinopeptides during assembly of fibrin*, Journal of Biological Chemistry, 260 (1985), pp. 10192–10199.

[25] R. I. Litvinov, O. V. Gorkun, S. F. Owen, H. Shuman, and J. W. Weisel, *Polymerization of fibrin: Specificity, strength, and stability of knob-hole interactions studied at the single molecule level*, Blood, 106 (2005), pp. 2944–2951.

[26] K. Mann, M. Nesheim, W. Church, P. Haley, and S. Krishnaswamy, *Surface-dependent reactions of the vitamin k-dependent enzyme complexes*, Blood, 76 (1990), pp. 1–16.

[27] J. P. Miletich, C. M. Jackson, and P. W. Majerus, *Interaction of coagulation factor xa with human platelets*, Proceedings of National Acadmey of Science, 74 (1977), pp. 4033–4036.

[28] M. W. Mosesson, *Fibrinogen and fibrin structure and functions*, Journal of Thrombosis and Haemostasis, 3 (2005), pp. 1894–1904.

[29] K. B. Neeves, D. A. R. Illing, and S. L. Diamond, *Thrombin flux and wall shear rate regulate fibrin fiber deposition state during polymerization under flow*, Biophysical Journal, 98 (2010), pp. 1344–1352.

[30] A. A. Onasoga-Jarvis, T. J. Puis, S. K. O'Brien, L. Kuang, H. J.Liang, and K. B. Neeves, *Thrombin generation and fibrin formation under flow on biomimetic tissue factor-rich surfaces*, Journal of Thrombosis and Haemostasis, 12 (2014), pp. 373–382.

[31] D. W. Peaceman and H. H. Rachford, Jr, *The numerical solution of parabolic and elliptic differential equations*, SIAM, 3 (1955), pp. 28–41.

[32] E. A. Ryan, L. F. Mockros, J. W. Weisel, and L. Lorand, *Structural origins of fibrin clot rheology*, Biophysical Journal, 77 (1999), pp. 2813–2826.

[33] A. Vindigni and E. Di Cera, *Release of fibrinopeptides by the slow and fast forms of thrombin*, Biochemistry, 35 (1996), pp. 4417–4426.

[34] E. Waxman, J. A. Ross, T. M. Laue, A. Guha, S. Thiruvikraman, T. Lin, W. H. Konigsberg, and Y. Nemerson, *Tissue factor and its extracellular soluble domain: the relationship between intermolecular association with factor viia and enzymic activity of the complex*, Biochemistry, 31 (1992), pp. 3998–4003.

[35] J. W. Weisel, *Fibrinogen and fibrin*, Advances in Protein Chemistry, 70 (2005), pp. 247–299.

[36] J. W. Weisel and R. I. Litvinov, *Mechanisms of fibrin polymerization and clinical implications*, Blood, 121 (2013), pp. 1712–1718.

[37] J. W. Weisel and L. Medved, *The structure and function of the αc domains of fibrinogen*, Annals of the New York Academy of Sciences, 936 (2001), pp. 312–327.

[38] J. W. Weisel and C. Nagaswami, *Computer modeling of fibrin polymerization kinetics correlated with electron microscope and turbidity observations: Clot structure and assembly are kinetically controlled*, Biophysical Journal, 63 (1992), pp. 111–128.

[39] J. W. Weisel, Y. Veklich, and O. Gorkun, *The sequence of cleavage of fibrinopeptides from fibrinogen is important for protofibril formation and enhancement of lateral aggregation in fibrin clots*, Journal of Molecular Biology, 232 (1993), pp. 285–297.

[40] J. H. Weiss, V. T. Turitto, and H. R. Baumgartner, *Role of shear rate and platelets in promoting fibrin formation on rabbit subendothelium.*, Journal of Clinical Investigation, 78 (1986), pp. 1072–1082.

[41] A. R. Wufsus and K. B. Neeves, *Pore Scale Phenomena: Frontiers in Energy and Environment*, vol. 10 of World Scientific series in nanoscience and nanotechnology, World Scientific, 5 Toh Tuck LInk, Singapore 596224, 2015, ch. 22, pp. 457–473.

[42] R. M. Ziff and G. Stell, *Kinetics of polymer gelation*, Journal Chemical Physics, 73 (1980), pp. 3492–3499.